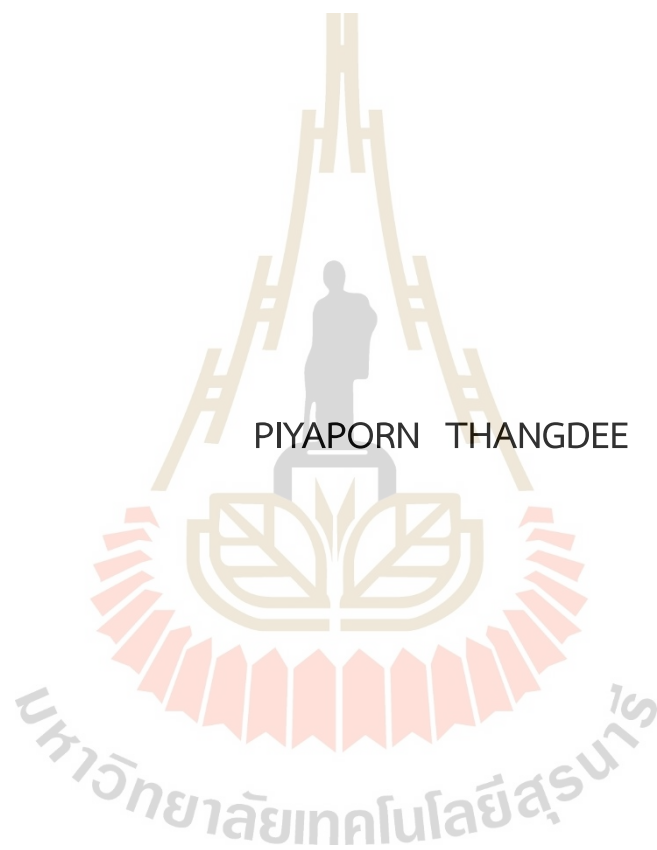# A STUDY OF V$_2$O$_5$ AND WO$_3$ ELECTROCHROMIC THIN FILMS PREPARED BY RADIO FREQUENCY MAGNETRON SPUTTERING

PIYAPORN   THANGDEE

A Thesis Submitted in Partial Fulfillment of the Requirements for the

Degree of Doctor of Philosophy in Physics

Suranaree University of Technology

Academic Year 2021

การศึกษาสมบัติอิเล็กโทรโครมิกของฟิล์มบางวาร์นาเดียมเพนต์ออกไซด์และทังสเตนไตรออกไซด์ที่เตรียมโดยวิธีอาร์เอฟแมกนีตรอนสปัตเตอร์ริง

นายปิยพร ทางดี

วิทยานิพนธ์นี้เป็นส่วนหนึ่งของการศึกษาตามหลักสูตรปริญญาวิทยาศาสตรดุษฎีบัณฑิต
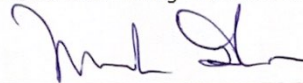สาขาวิชาฟิสิกส์
มหาวิทยาลัยเทคโนโลยีสุรนารี
ปีการศึกษา 2564

A STUDY OF V_2O_5 AND WO_3 ELECTROCHROMIC THIN FILMS PREPARED BY RADIO FREQUENCY MAGNETRON SPUTTERING

Suranaree University of Technology has approved this thesis submitted in partial fulfillment of the requirements for the Degree of Doctor of Philosophy
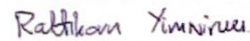
Thesis Examining Committee

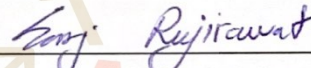_____

(Assoc. Prof. Dr. Panomsak Meemon)

Chairperson

_____

(Assoc. Prof. Dr. Prapun Manyum)

Member (Thesis Advisor)

_____

(Prof. Dr. Rattikorn Yimnirun)

Member

_____

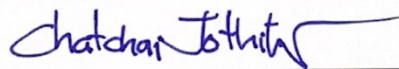(Assoc. Prof. Dr. Saroj Rujirawat)

Member

_____

(Dr. Narong Chanlek)

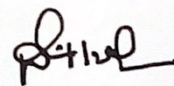Member

_____

(Dr. Pinit Kidkhunthod)

Member

_____

(Assoc. Prof. Dr. Chatchai Jothityangkoon)

Vice Rector for Academic Affairs

and Quality Assurance

_____

(Prof. Dr. Santi Maensiri)

Dean of Institute of Science

นายปิยพร ทางดี : การศึกษาสมบัติอิเล็กโทรโครมิกของฟิล์มบางวาร์นาเดียมเพนต์ออกไซด์และทังสเตนไตรออกไซด์ที่เตรียมโดยวิธีอาร์เอฟแมกนีตรอนสปัตเตอร์ริง (A STUDY OF V_2O_5 AND WO_3 ELECTROCHROMIC THIN FILMS PREPARED BY RADIO FREQUENCY MAGNETRON SPUTTERING). อาจารย์ที่ปรึกษา : รองศาสตราจารย์ ดร.ประพันธ์ แม่นยำ, 153 หน้า.

คำสำคัญ: สปัตเตอร์ริง, วาร์นาเดียมเพนต์ออกไซด์

วิทยานิพนธ์นี้มุ่งเน้นศึกษา การเตรียมฟิล์มบางวานาเดียมเพนต์ออกไซด์ด้วยวิธีอาร์เอฟแมกนีตรอนสปัตเตอร์ริงจากเป้าโลหะวาเนเดียม โดยศึกษาผลของการแปรค่าอัตราส่วนของปริมาณก๊าซ O_2/Ar ที่ให้ในระหว่างการสปัตเตอร์ต่อการเกิดฟิล์มบางวานาเดียมเพนต์ออกไซด์ซึ่งกำหนดให้ค่ากำลังและเวลาในการสปัตเตอร์เท่ากับ 200 วัตต์ และ 80 นาทีตามลำดับมีค่าคงที่ จากนั้นนำฟิล์มบางวานาเดียมเพนต์ออกไซด์ไปศึกษาลักษณะด้วย กล้องจุลทรรศน์อิเล็กตรอน (SEM) กล้องจุลทรรศน์แรงอะตอม (AFM) เครื่องเอกซ์เรย์ดิฟแฟรกชัน (XRD) และยูวีวิสซิเบิลสเปกโทรสโกปี (UV-Vis) เพื่อใช้ในการวิเคราะห์ลักษณะพื้นผิวและความหนา โครงสร้างผลึก และคุณสมบัติทางแสงของฟิล์มบางวานาเดียวเพนต์ออกไซด์ตามลำดับ และสุดท้ายคือศึกษาผลกระทบของการแปรค่าอัตราส่วนของปริมาณก๊าซ O_2/Ar ต่อโครงสร้างลักษณะเฉพาะของฟิล์มบางวาเนเดียมเพนต์ออกไซด์โดยเทคนิคการดูดกลืนรังสีเอกซ์ (XAS)

ผลปรากฏว่าสเปกตรัม XANES ที่ขอบการดูดกลืน V K-edge พบเลขออกซิเดชันของฟิล์มบางวานาเดียมเพนต์ออกไซด์ที่เงื่อนไข O_2/Ar = 1/20 (ในหน่วย sccm) มีการรวมกันของเลขออกซิเดชันของ V ที่ V^{3+}, V^{4+} และ V^{5+} ในขณะที่เงื่อนไขอื่น ๆ มี V^{5+} เป็นส่วนใหญ่ ดังนั้นการแปรค่าอัตราส่วนของปริมาณก๊าซ O_2/Ar ที่มากขึ้นทำความเข้มของระดับพลังงานที่สถานะ 1S⟶3d มีค่ามากขึ้น จากผลที่ได้นี้ทำให้ฟิล์มบางที่สังเคราะห์นั้นมีโครงสร้างของ V_2O_5 อย่างที่ต้องการ และเพื่อเป็นการยืนยันสเปกตรัมของ XANES เราจึงใช้สเปกตรัมของการวัดแบบ EXAFS เพื่อแสดงให้เห็นว่าลักษณะเฉพาะเชิงโครงสร้างโดยรอบของอะตอม V นั้นสรุปได้ว่าการแปรค่าอัตราส่วนของปริมาณก๊าซ O_2/Ar มีผลทำให้เกิดฟิล์มบาง V_2O_5 ที่มีโครงสร้างแบบออร์โทรอมบิก

การประยุกต์จึงนำไปใช้กับอุปกรณ์ที่เคลือบด้วยวัสดุที่มีสมบัติทางอิเล็กโทรโครมิก ซึ่งเป็นวัสดุที่นำไปใช้ในการประหยัดพลังงานไฟฟ้า และวัสดุโลหะออกไซด์ที่มีสมบัติอิเล็กโทรโครมิกก็เป็นอีกตัวหนึ่งที่น่าสนใจ โดยในงานวิจัยนี้ได้นำเสนอฟิล์มบางวาเนเดียมเพนต์ออกไซด์ซึ่งเป็นสารประกอบที่หาง่าย ราคาไม่แพง และมีสมบัติการเป็นสารอิเล็กโทรโครมิก ผลการทดลองที่ได้จาก

การวัดด้วยเทคนิคการเลี้ยวเบนรังสีเอ็กซ์ (XAS) พบว่าเมื่อให้ความต่างศักย์แก่ฟิล์มบาง V_2O_5 ที่ +1.8 V และ -1.8 V ทำให้ฟิล์มมีเลขออกซิเดชันที่ V^{5+} (สถานะจางสี) และ V^{3+} และ V^{4+} (สถานะเปลี่ยนสี) ตามลำดับ สรุปได้ว่ามีการแทรกตัวของไอออนของ Na (NaCl) ในฟิล์มจึงทำให้เลขออกซิเดชันเปลี่ยนไป และเมื่อวัดประสิทธิภาพของสมบัติทางอิเล็กโทรโครมิกพบว่าที่เงื่อนไข O_2/Ar = 3/20 (ในหน่วย sccm) มีค่า $\Delta\%T$ มากที่สุดที่ 22.17%

และมีการศึกษาเพิ่มเติมกับฟิล์มบาง WO_3 ที่เตรียมโดยวิธีดีซีแมกนีตรอนสปัตเตอร์ริง ซึ่งสารตัวอย่างได้ศึกษาจาก เครื่องเอ็กซ์เรย์ดิฟแฟรกชัน (XRD) และยูวีวิสซิเบิลสเปกโทรสโกปี (UV-Vis) เพื่อใช้ในการวิเคราะห์ลักษณะโครงสร้างผลึก และคุณสมบัติทางแสง ตามลำดับ อีกทั้งยังนำเทคนิคการดูดกลืนรังสีเอ็กซ์มาใช้เพื่อดูโครงสร้างโดยรอบของอะตอม W ในฟิล์มบาง WO_3 ในสถานะจางสีและเปลี่ยนสี พบว่าการแทรกตัวของไอออนของโพแทสเซียม (K) ทำให้ระยะห่างระหว่างอะตอมของ W กับอะตอมข้างเคียงมีค่าเพิ่มขึ้น และจากสเปกตรัมของ XANES และ EXAFS ยืนยันว่ามีเกิดเลขออกซิเดชันที่ W^{5+} ในสถานะจางสีและที่สถานะนี้มีการเปลี่ยนแปลงรูปแบบโครงสร้างของตัว WO_3 เนื่องจากมีการแทรกตัวของไอออนของโพแทสเซียม

สาขาวิชาฟิสิกส์

ปีการศึกษา 2564

ลายมือชื่อนักศึกษา _____

ลายมือชื่ออาจารย์ที่ปรึกษา _____

PIYAPORN THANGDEE : A STUDY OF V_2O_5 AND WO_3 ELECTROCHROMIC THIN FILMS PREPARED BY RADIO FREQUENCY MAGNETRON SPUTTERING. THESIS ADVISOR : ASSOC. PROF. PRAPUN MANYUM, Ph.D. 153 PP.

Keyword: Sputtering, V_2O_5

In this work, RF reactive magnetron sputtering with a vanadium metal target produced vanadium oxide thin films. The influence of O_2/Ar flow rate on vanadium oxide thin films was studied by varying gas flow rate and fixed RF power at 200 W and sputtering duration to 80 minutes. SEM, AFM, X-Ray Diffractometer, and UV-Visible spectroscopy were used to analyze the surface morphology, crystal structure, and optical properties of V_2O_5 thin films. The effect of the O_2/Ar ratio on the local structure of vanadium oxide thin films was investigated using XAS at Synchrotron. The x-ray absorption near-edge structure (XANES) assessed the oxidation states of vanadium oxide thin films. It was found that the films made with O_2/Ar flow rate at 1/20 sccm included vanadium in V^{3+}, V^{4+}, and V^{5+} oxidation states, whereas the others contained mostly V^{5+}. The greater O_2/Ar flow rate may generate an increase in energy flux at the substrate and the intensity of the $1s \longrightarrow 3d$ transition peak, resulting in a faster deposition rate. The gas flow rate might be modified to get the required V_2O_5 structure. The extended x-ray absorption fine structure (EXAFS) confirmed the XANES findings, demonstrating that the structural environment surrounding V atoms is in excellent accord with the V_2O_5 orthorhombic structure. Finally, XANES and EXAFS fitting findings showed that O_2 flow rate influenced the local structure of vanadium oxide thin films.

Electrochromic switching devices have a lot of attention since these thin films are promising materials for energy saving applications. The vanadium oxide technique is simple and affordable since only one layer of material is needed to color.

Electrochemical XAS measurements revealed that electrodeposition of V_2O_5 thin films at 1.8 V produced films with varied local electronic structures and gas flow rates. V_2O_5 thin films have oxidation states ranging from V^{5+} (bleached) through V^{3+} and V^{4+} (colored). This work employed XAS to assess the effects of Na insertion/extraction on vanadium oxidation states. Injection of sodium causes color shift. With $O_2/Ar = 3/20$ (in sccm unit), the electrochromic device with V_2O_5 thin film coating showed a better optical contrast (Δ %T, good electrochromic properties) of 22.17%. So, the electrochromic device works nicely at $O_2/Ar = 3/20$ (sccm) (compaired with other conditions).

WO$_3$ thin films produced by DC reactive magnetron sputtering were also used in the collaborative samples. X-Ray Diffractometer (XRD) and UV-visible spectroscopy (UV-Vis) were used to analyze the crystal structure and optical characteristics of WO_3 thin films, respectively. X-ray absorption spectroscopy was used to investigate the local structure surrounding tungsten ions in clear and colored WO_3 thin films. The potassium insertion/extraction of the development of small-radius under thin-film coloring is confirmed by the examination of the XANES and EXAFS components of the experimental spectra. With the creation of W^{5+} ions, this process is followed by a substantial lattice deformation surrounding the tungsten ions with trapped electrons, as well as a rearrangement of their electronic structure.

School of Physics

Academic Year 2021

Student's Signature _____

Advisor's Signature _____

ACKNOWLEDGEMENTS

Piyaporn Thangdee

CONTENTS

CONTENTS (Continued)

CONTENT (Continued)

LIST OF TABLES

LIST OF TABLES (Continued)

LIST OF FIGURES

LIST OF FIGURES (Continued)

LIST OF FIGURES (Continued)

LIST OF FIGURES (Continued)

LIST OF FIGURES (Continued)

LIST OF FIGURES (Continued)

LIST OF FIGURES (Continued)

LIST OF FIGURES (Continued)

LIST OF ABBREVIATIONS

°C	Degree Celsius
BL5.2	Beamline 5.2
EXAFS	Extended X-ray Absorption Fine Structure
E0	Absorption edge
EB	Binding Energy
eV	Electron-Volt
K	Kelvin
h	Plank's Constant
Ie	Electron Current
Ip	Photon Current
S	Spin
SLRI	Synchrotron Light Research Institute
XANES	X-ray Absorption Near Edge Structure
XAS	X-ray Absorption Spectroscopy
SEM	Scanning Electron Microstructure
XRD	X-ray Diffraction
λ	Wavelength
λ_i	Photoelectron mean free path
σ^2	Debye-Waller factor
S_0^2	Scale Factor

CHAPTER I

INTRODUCTION

1.1   Introduction

Electrochromism (EC) is the term used to describe the persistent and reversible changes in optical characteristics caused by an applied voltage. Electrochromic materials have garnered significant attention in recent years for a variety of promising applications, including smart windows for energy-efficient buildings, self-dimming rear-view mirrors for automobiles, information displays, and electrochromic e-skins, as well as energy storage devices such as electrochromic supercapacitors and electrochromic batteries. A typical electrochromic device (ECD) is composed of several layers, including a transparent conductor, an electrochromic film, an electrolyte layer, and an ion storage layer (Cai et al., 2016; Cong et al., 2016; Granqvist, 2014). The electrochromic layer (most often WO3 and other transition metal oxides) alters its optical characteristics (typically the transmittance in visible light) in response to an applied voltage pulse and may readily restore to its bleached original condition.

Viogens (as polymeric films), conjugated conducting polymers, transition metal oxides (e.g., WO_3, NiO, and V_2O_5), and metal coordination complexes are common EC materials (e.g., polymeric, evaporated, and sublimed films) under investigation. Among these materials, thin-film transition metal oxides have become very attractive due to their variety in composition/structure and exceptional electrochromic performance. Recent advances in transition metal oxide–based electrochromic have included the development of novel materials, the introduction of novel nanostructures, element doping, and composites, as well as novel designs and concepts for visible light and near-infrared radiation (NIR) dual-modulated smart windows and self-powered electrochromic batteries.

Vanadium pentoxide (V_2O_5), an n-type semiconductor material with a large band gap, is a promising material for a wide variety of applications, such as thermochromic, electrochromic and gas sensing materials. V_2O_5 thin films have sparked considerable attention. V^{5+} ion-generated active sites are involved in gaseous molecule adsorption and catalytic reactions. A conventional electrochromic device is composed of three layers: electrochromic, electrolyte, and ion storage (ECD). Both electrochromic and storage layers are placed on transparent substrates coated with a transparent conductive film. ECDs function by altering the optical properties of various colors. V_2O_5 is utilized as a counter electrode material in ECDs. During optical switching, it generates electrochemical redox reactions that balance charge transfer at the electrochromic working electrode. While the double injection of ions and electrons may be used to explain the standard electrochromic process of V_2O_5, the electrical double-layer phenomena is employed to store energy in electrochemical capacitors (ECs), which are sometimes referred to as "supercapacitors." The two forms of ECs are electrochemical double-layer capacitors (EDLCs) with a non-faradaic charge and pseudocapacitors based on a faradaic electrochemical redox reaction. Due to its pseudocapacitive characteristics, wide oxidation states, and high specific capacitance, V2O5 has garnered attention among transition-metal oxides used as ECs electrodes.

Another interesting electrochromic material is Tungsten Trioxide (WO3). It is one of the most desirable electrode materials for electrochromic windows, driving mirrors, displays, and other devices that need active films (Granqvist, 1995). Coloration happens as a result of the introduction of a tiny cation, such as Li+, through an electrochemical process (Faughnan, 1975):

$$WO_3(bleached) + xLi^+ + xe^- \longleftrightarrow Li_xWO_3(blue) \qquad (1.1)$$
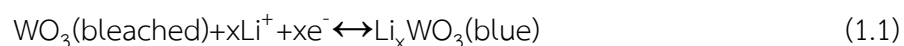
Despite intensive research on this subject, the impact of cation insertion on the local structure of amorphous WO_3 remains a point of conflict. The most researched electrochromic material, particularly in its amorphous form. Crystalline WO_3 exhibits a shift in optical constants throughout a large spectral range in the visible and infrared (IR) regions when intercalated with Li^+ or H^+ ions. Until date, the maximum coloring efficiency (CE) in the visible area of the electromagnetic spectrum has been found in

amorphous WO_3 films. These films can only be employed in lithium-based electrolytes due to their high breakdown rate in acidic electrolyte solutions, resulting in longer response times.

X-ray absorption spectroscopy (XAS) is one of the few techniques available for exploring the local structure of these disordered molecules. Measurements of linearly polarized synchrotron radiation using X-ray absorption spectroscopy (XAS) are an extremely strong method for determining the electron orbital orientation and structural changes in a material. The XAS would provide a wealth of information regarding the crystallographic properties and unoccupied electronic states of transition metal 3d and oxygen 2p states. Whereas Extended X-ray Absorption Fine Structure (EXAFS) is a structural analysis technique and a very effective tool for characterizing local structures. Y.K. Ho (Ho et al., 2013) performed an investigation on V_2O_5 films made through the sol–gel spin coating process. These films were discovered to have an orthorhombic Pmmn layered structure and to display outstanding gasochromic colouring. V_2O_5 exhibited intense anisotropic absorption spectra due to its layered structure. The three-dimensional band structures and electron correlation effects were discovered to be critical in defining this material's gasochromic characteristics. The gasochromic effect and colouring mechanism of these films were examined in depth using X-ray absorption spectroscopy based on the XAS findings. The research established that the valence state of vanadium shifted from 4.8^+ to 4.1^+ as a result of hydrogen ion insertion, and a distortion in the structural symmetry of the VO_6 octahedron was detected.

1.2   Scope and limitations

In this work, vanadium oxide thin films are prepared by using radio frequency reactive magnetron sputtering with Vanadium metal targets. The effects of preparation conditions are investigated by varying Ar/O_2 flow rate. The morphology and phase formation of V_2O_5 films are characterized by scanning electron microscope (SEM) and X-Ray Diffraction (XRD), respectively. The chemical composition of the samples is examined using. UV-Vis spectroscopy is used for investigating the optical properties. The influence of Ar/O_2 ratio on local structure of vanadium oxide thin films is studied

by Synchrotron x-ray absorption spectroscopy (XAS) technique. The local structure around V atoms is measured at V K-edge by x-ray absorption near-edge structure (XANES). In addition, changes in local structure depending on Ar/O_2 ratio around V atoms are examined using extended x-ray absorption fine structure (EXAFS). The final products with optimal structural, electrical properties are expected to be used as the electrodes of electrochromic devices and compared the efficiency of electrochromic (ΔT (%)) with collaboration sample (WO3 thin films from NECTEC).

CHAPTER II

BACKGROUND AND LITERATURE REVIEWS

2.1 Electrochromic materials

Electrochromic (EC) materials change color in response to an external electrical bias, either between colored and colorless states or between two or more colored states. The color variations are caused by the materials absorption spectra varying over the UV–visible–near-infrared (NIR) spectrum, which may be a result of the oxidation and reduction of a particular chemical in the presence of an electrical bias (Mortimer, 1997; Mortimer, 1999; Rosseinsky and Mortimer, 2001; Rowley and Mortimer, 2002). EC materials often display color shifts between two distinct colors or between a colored and bleached state. Anodically colored or cathodically colored materials exhibit colorful hues in their oxidized or reduced forms, respectively (Camurlu, 2014; Qu et al., 2017; Cao et al., 2016). Numerous EC materials with various redox states have an unmatched capacity to transition between several colored states. Polyelectrochromism is a term that refers to this phenomenon (Meacham et al., 2004; Oßigwald et al., 1993; Chang et al., 2008). In most circumstances, a steady current source is necessary to maintain the color associated with an electro-oxidized or -reduced condition. Certain materials, however, need very minimal current to preserve a certain color state, which is referred to as the "memory effect."

Deb invented the first EC device in 1969, when he showed the controlled and reversible change of hue using tungsten trioxide (WO_3) (Deb, 1969; Deb, 1973). Numerous kinds of EC materials and devices have been described since then, including metal oxides, viologens, and conjugated polymers. Due to the ease with which EC materials change color in the visible area, they were greatly sought after and used in optical display applications. The first study on EC materials in the United States, Soviet Union, Japan, and Europe was inspired by their potential uses in information displays.

Several large international companies, including IBM (Chang et al., 1975; Chang et al., 1976), Zenith Radio, the American Cyanamid Corporation, and RCA in the United States (Faughnan et al., 1975; Faughnan et al., 1975; Crandall and Faughnan, 1976), Canon in Japan (Hajimoto and Hara, 1976), Brown Boveri in Switzerland (Zeller et al., 1976), Electrochromism has maintained a high level of interest in basic research throughout the years. Interest in EC materials was rekindled in the mid-1980s due to their possible use in fenestration technology, which was seen as a means of improving building energy efficiency. The newly developed "smart" window technology may allow for variable light and solar energy transmittance, resulting in energy savings and increased interior comfort. Nowadays, EC materials and devices have been extensively employed in a variety of fields during the last several decades, most notably information displays, variable reflectance mirrors, smart windows, and variable emittance surfaces.
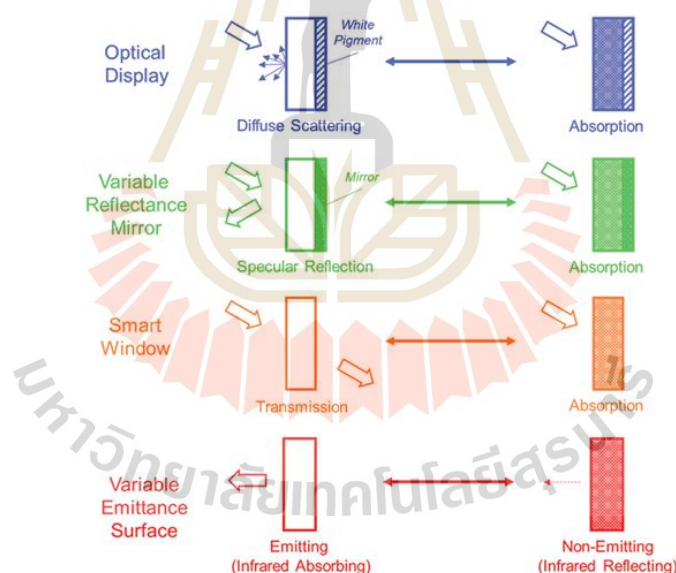
Figure 2.1 The principles behind four distinct EC device applications. The arrows represent the direction of incoming and exiting electromagnetic radiation; the thickness of the arrows indicates the strength of the radiation.

The ideas behind the four aforementioned applications are shown in figure 2.1. EC materials and devices may be applied on translucent, transparent, or mirror surfaces, and the quantity of light absorbed, reflected, or traveling through the devices can be changed by changing the electric current flowing through them. By and large,

all EC devices may be classed according to their mode of operation—transmission or reflection.

In real-world applications, EC materials must be integrated into practical EC devices. EC materials are often present as thin films inside EC devices, enabling them to be in close proximity to electrodes and electrolytes while yet allowing current to pass through the devices. Typically, an EC thin-film device has a multi-layered structure, as seen in figure 2.2, which may be utilized to customize the optical characteristics of the device when applied with a voltage and return to their original condition when the voltage's polarity is reversed. Electrical contact between layers is critical for stability and EC performance. As illustrated in figure 2.2, a typical EC device consists of at least five layers: transparent conducting oxide (TCO) layer/ion storage layer (IS)/ion conducting layer (electrolyte)/EC layer/TCO layer. These layers can be superimposed on a single substrate or sandwiched between two substrates in a laminate configuration. The EC layer is coated on one side of the ion conductor, while the ion-storage layer is placed on the opposite side. The purpose of the ion-storage layer is to conceal the galvanic cell's operating principle. The conducting layer is primarily responsible for transporting charge from a power source to its associated EC layer (Yang et al., 2016; Patel et al., 2017; Berton et al., 2003; Invernale et al., 2009; Granqvist et al., 2009). The ion conductor, which is composed of tiny mobile ionic charge carriers, completes the circuit by promoting the exchange of ions between electrodes. Finally, epoxy and other appropriate sealants are employed to prevent electrolyte leakage during operation (Byker, 2001; Eh et al., 2017; Thakur et al., 2012).
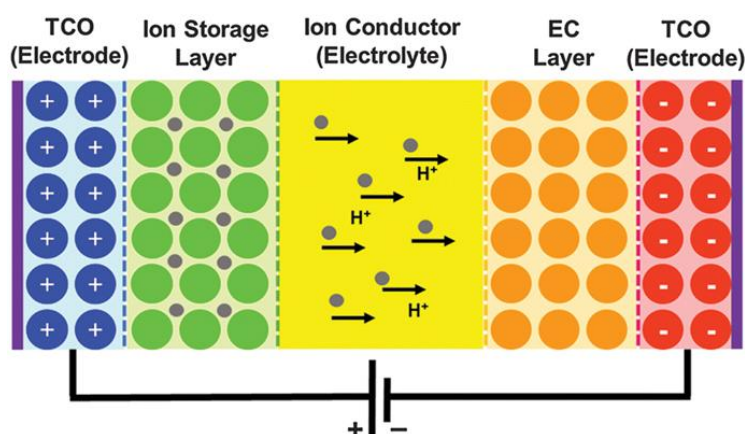
Figure 2.2 The bare bones of an EC device.

For devices supported by a single glass or polyester substrate, optical modulation of EC devices is primarily influenced by H^+ or Li^+ transport. However, laminated devices exhibit certain distinctions from their unlaminated counterparts. Electrolytes including polyethylene oxide (PEO), a copolymer of sodium vinylsulfonic acid and 1-vinyl-2-pyrrolidinone, and poly-2-acrylamido-2-methyl-propane sulfonic acid are often used in devices that utilise H+ transport. Meanwhile, the counter electrodes are composed of polyaniline, Prussian Blue, or a combination of the two, resulting in a broad modulation range of visible light. On the other hand, laminated devices that include Li^+ transport are quite unique. In other words, the polymers are composed of polymethyl methacrylate (PMMA) copolymerized with polypyrrole, propylene carbonate, silane, polypropylene, and glycidyloxypropyl trimethoxysilane copolymerized with tetraethylene glycol, polyethylene glycol methacrylate copolymerized with PEO ormolyte, or polyvinylidene fluoride. These polymers become ion conductors when an optimum Li salt is added. Additionally, V_2O_5, SnO_2 doped with Mo and Sb, and TiO_2 with or without ZrO_2 or CeO_2 additions are employed as counter electrodes in Li^+ transport systems.

Numerous classes of compounds have been reported to possess EC properties, including transition metal oxides (WO_3 and TiO_2), metal coordination complexes ($CoFe(CN)_6$ and Prussian Blue), organic molecular dyes (e.g. viologen), and organic conducting polymers (e.g. polythiophenes, polyanilines, and poly(3,4-ethylenedioxythiophene (PEDOT)). Organic EC materials, in particular, provide a number of benefits, including strong color, simplicity of structural change, excellent processability, cheap cost, and film-forming ability. On the other hand, their inorganic equivalents have been shown to have excellent chemical and electrochemical stability, as well as a broad operating temperature range (Ho and Greenberg, 1994). Additionally, organic/inorganic nanocomposites have been produced to combine the benefits of organic and inorganic electrochemical materials. These hybrid materials might be made entirely of EC-active organic or inorganic components, or a combination of both. Much attention has been made in the EC nanocomposites to changing the interfacial contacts between the organic and inorganic components, since these

interactions are critical for the structure's strength, mass transfer, electron conduction, and EC performance (Xiong et al., 2017; Mortimer et al., 2015; Thakur et al., 2012).

2.1.1 Electrochromic Metal Oxides

2.1.1.1 Cathodic Oxides

WO_3 has garnered substantial attention as a well-known and widespread inorganic electrochromic substance. Over a century has been spent studying reversible color shifts in tungsten bronzes. For the coloring state induced by cathodical charge, the intercalation of cations such as H^+, Li^+, and Na+ along with charge-compensating electrons decreases the tungsten cations from W^{6+} to W^{5+}, transforming the material from a transparent to a dark blue state (Cong et al., 2016) As previously stated, the reversible electrochromic phenomena conform to Reaction (1). A large transmittance window is critical in this respect since it permits simple modulation in response to demands. A recently reported WO_3 film was found to have a porous and nanoscale interconnecting network structure when created utilizing a pulsed electrochemical deposition process (Cai et al., 2016). It demonstrated near-ideal optical modulation, reaching around 97.7% at 633 nm, far higher than the commonly reported figure of over 80% (Cai et al., 2016). Additionally, the WO_3 film with this novel porous structure demonstrated rapid switching speeds of 6 and 2.7 seconds for the coloring and bleaching phases, respectively (Cai et al., 2016).

As shown in figure 3, further transition metal oxides that are cathodically colored include MoO_3, TiO_2, Ta_2O_5, and Nb_2O_5 (Granqvist, 2014). As with WO_3, when ions and electrons are supplied, MoO_3 changes its color from translucent to dark blue, and the substoichiometric MoO_3 film exhibits strong electrochromic activity. In general, the advantages and disadvantages of MoO_3 over WO_3 are as follows:

1) MoO_3 films have a lower coloring efficiency and cycle life than WO_3 films.

2) Molybdenum bronze in its colored condition is more compatible with the sensitivity of human eyes (Chernova et al., 2009).

3) In the visible range, MoO_3 film absorbs light more powerfully and evenly.

Figure 2.3 Documented elements used for cathodic and anodic electrochromism.

2.1.1.2 Anodic Oxides

Alternatively, anodical coloring transition metals include the well-studied Ni and Ir (Granqvist, 2014; Zhou et al., 2016), as well as the often-reported V, Fe, (Garcia et al., 2011), Co, (Lee et al., 2012; Xia et al., 2010), and Mn (Yoshino et al., 2012). (Figure 2.3). Due to the high cost and scarcity of Ir (even when diluted with less expensive Sn or Ta), the most often employed anodic oxide–based EC material has been Ni oxide (Zhou et al., 2016). NiO film undergoes a transformation from translucent to brown upon charging. Similarly, the electrochromic performance of NiO is greatly impacted by the charge transport kinetics inside the electrochromic material, as well as ion migration within the electrolyte and at their interface (Ma and Wang, 2016). Nanostructuring has been shown to significantly reduce ion diffusion length, hence accelerating the movement of ions and charges, while also improving coloring efficiency, switching kinetics, and lifespan owing to the increased specific surface area available for contact with the electrolyte (Ma and Wang, 2016).

1.2 Vanadium Oxide

2.2.1 V_2O_5 structure and bonding

Vanadium (V) oxide (vanadia) is the inorganic compound with the formula V_2O_5 (Bauer et al., 2012). Vanadium pentoxide is a brown/yellow solid that has a bright orange color when newly precipitated from an aqueous solution. It is both an

amphoteric oxide and an oxidizing agent because of its high oxidation state. It is the most significant vanadium compound in terms of industry, serving as the primary precursor to vanadium alloys and as an industrial catalyst. Shcherbinaite, the mineral form of this chemical, is exceedingly uncommon, occurring virtually exclusively in fumaroles. Navajoite is the name for a mineral trihydrate with the formula $V_2O_5.3H_2O$.

2.2.1.1 The vanadium oxide

The principal oxides of vanadium occur as single valence in oxidation states from V^{2+} to V^{5+}, in the form of VO, V_2O_3, VO_2, and V_2O_5. However, the vanadium–oxygen phase diagram also includes mixed valence oxides containing two oxidation states, such as V_6O_{13} with V^{5+} and V^{4+} and a series of oxides between VO_2 and V_2O_3 (e.g., V_8O_{15}, V_7O_{13}, V_6O_{11}, etc.) which contain V^{4+} and V^{3+} species. The mixed valence oxides are formed by introducing oxygen vacancy defects. If the number of oxygen vacancies exceeds a certain value, the vacancies tend to correlate and form crystallographic shear planes (i.e., the vacancies associate along a lattice plane) and are subsequently eliminated by reorganization of V–O coordination units. The result is a series of oxides with related stoichiometries, such as the Magnéli phases with VnO_{2n-1} and the Wadsley phases with $V_{2n}O_{5n-2}$ formulas (Surnev et al., 2003). V_2O_5 undergoes a semiconductor/metal phase transition near 257 °C (Kamper et al., 2000). A large change in electrical properties accompanies the transition, thus thermally activated electrical and/or optical switches can be fabricated. Since optical and electrical behavior are coupled, V_2O_5 is especially interesting in thin film form due to the possibility of integration into microelectronics circuitry. V_2O_5 has been suggested for use as a variable transmittance electrochromic device for controlling sunlight through windows (Weckhuysen and Keller, 2003; Wruck et al., 1989).

2.2.1.2 The crystal structure and utility of V_2O_5

In the V–O system, V_2O_5 is the saturated (highest oxidation state) oxide, and hence the most stable. It crystallizes with a Pmnm space group orthorhombic unit cell structure with lattice values of a=11.510 Å, b=3.563 Å, and c=4.369 Å. It is made up of distorted trigonal bipyramidal coordination polyhedra of O atoms surrounding V atoms and has a layer-like structure. As seen in figure 2.4, the polyhedra share edges to form $(V_2O_4)_n$ zigzag double chains in the (001) direction and are cross connected in

the (100) direction by shared corners (Goodenough, 1971). The deformed polyhedra feature a short (1.58 Å) vanadyl bond, $[VO]^{2+}$, and four O atoms at distances varying from 1.78 to 2.02 in the basal plane. The sixth O atom in the coordination polyhedron lies along the vertical axis opposite to the V–O bond at a distance of 2.79 Å.

V_2O_5 is a good catalyst from a chemical basis (Suli et al., 1986) because of its rich and diversified chemistry, which is based on two factors: the wide range of vanadium oxidation states (ranging from 2+ to 5+) and the diversity of oxygen coordination geometries. The occurrence of variably coordinated oxygen ions, which constitute a crucial element for altering physical and chemical surface characteristics, is due to this structural richness. V_2O_5 is a potential material for energy storage devices because of its layered structure and high ionic storage capacity.

Among transition metal oxides (e.g., WO_3, MoO_3), V_2O_5 has drawn significant interest in the past decades due to industrial applications such as electrochromic devices, optical switching devices, and reversible cathode materials for Li batteries. V_2O_5 thin films have been prepared by various methods, on different substrates, including electron beam evaporation, magnetron sputtering, pulsed laser deposition, chemical vapor deposition, spray pyrolysis, electrospinning, sol–gel, spin coating, and film growth in the field of a CW IR laser beam.

In general, vanadium oxide thin films are amorphous when deposited at a relatively low substrate temperature (<300 ^{o}C). The temperature of crystallization depends on the growth technique as well as the structure (crystalline or amorphous) of the substrate material. For example, in the case of pulsed laser deposition, when ejected species in the laser induced plasma plume condense on the substrate surface with high average kinetic energies, the crystallization process can take place at a lower substrate temperature due to enhanced adatom mobilities.
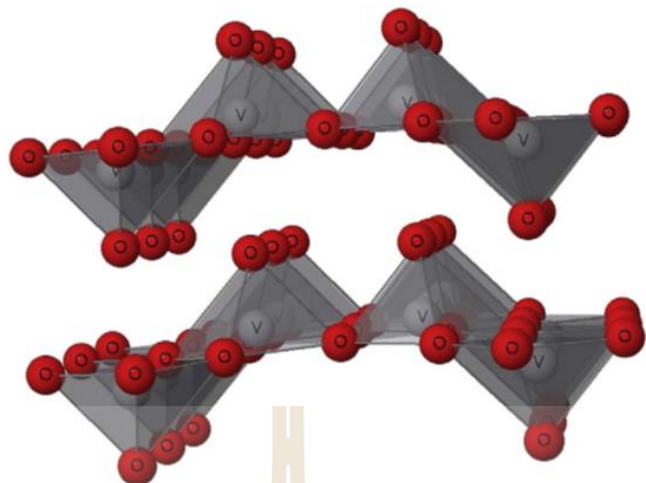
Figure 2.4 The structure of V_2O_5 is orthorhombic. (Beke, 2011)

Table 2.1 The physical properties of V_2O_5.(Bauer et al., 2012)

Crystal structure	Orthorhombic a = 11.510 Å, b = 3.563 Å, c = 4.369 Å
Molar mass	181.8800 g/mol
Density	3.357 g/cm^3
Appearance	Yellow solid
Melting point	690 $^\circ$C
Boiling point	1,750 $^\circ$C

2.2.2 V_2O_5 thin films

2.2.2.1 Thin films synthesis of V_2O_5 thin films

The deposition process and the operating conditions have a strong influence on the structure and morphology of vanadium oxide films. Because direct formation of crystalline V_2O_5 films is difficult, except for some sub-stoichiometric VO_x oxides, the films must be annealed in air at a high temperature. The different evaporation methods are described in this section, along with some common instances for each process. The thin film application determines the deposition procedure used. For electrochromic V_2O_5 films that require large surface coatings, methods such as

electrodeposition (Vernardou et al., 2013), reactive sputtering (Lin et al., 2008), sol-gel (Ma et al., 2016), hydrothermal method (Vernardou et al., 2014), and doctor-blade route (Mjejri et al., 2016) have been used. In Beke's review, the reader will get further information (Beke, 2011). When V_2O_5 is heated over its melting point during the deposition process in vacuum or in a reducing environment, oxygen atoms are removed from the film network, causing defects or reduced VO_x phases to develop. As a result, proper deposition parameters may be used to regulate structural and morphological abnormalities, as well as phase instability.

2.2.2.1.1 Thermal deposition

The thermal evaporation technique is the simplest way for forming thin films without the need of a catalyst. It is based on the formation of vapor flux in a high vacuum chamber (pressure 100 mPa). Resistive heating is used to evaporate the material in this procedure. In most cases, the unprocessed powder is put in a molybdenum boat that has been heated to T_{boat}. Variations in the substrate temperature T_s, the flow of reactive gases (in cm^3min^{-1} at standard pressure and temperature, expressed as "sccm" hereafter), and the length of the target evaporation are used to modify the structure, stoichiometry, and morphology of the deposited films. Thermally evaporated polycrystalline V_2O_5 films (10–20 nm grain size) were made, for example, at T_{boat} = 650 $^{\circ}$C for 6 hours with a gas flow of 13 sccm Ar + 50% O_2 (Rao, 2014). The substrate's nature is a key aspect in obtaining films with favored orientation (Chakraborty et al., 2007). When deposited on silicon (111) wafers by vacuum thermal evaporation, V_2O_5 films were amorphous at T_s ≤ 200 $^{\circ}$C and polycrystalline at T_s ≥ 300 $^{\circ}$C. This temperature is ideal for V_2O_5 films with (001) planes parallel to the substrate that are highly orientated (Kumar et al., 2003). Nanostructured V_2O_5 thin films (25 nm grain size) thermally deposited onto Ni substrates at T_s = 300 $^{\circ}$C show preferential (001) orientation. These films have pseudocapacitance of 730 mF cm^{-2} at current density of 1 mA cm^{-2} and charge transfer resistance of 7.5 Ω (Dhananjaya et al., 2017). The thermally evaporated V_2O_5 films at T_s = 25 $^{\circ}$C, 100 nm thick, crystallized after annealing process at 500 $^{\circ}$C with grain size 26 nm and exhibited an electrical conductivity of 5.5 S cm^{-1} (activation energy of 0.16 eV) (Santos et al. 2013) and optical bandgap of 2.8 eV.

2.2.2.1.2 Flash-evaporation

The granules are put in a reservoir and poured drop by drop into the boat heated at T_{boat} to assure vaporization in the flash-evaporation process. This method enables for the control of vaporization rates while also preserving any degradation of the starting material prior to evaporation (Julien et al., 1994). V_2O_5 flash-evaporated films have been shown to be more homogenous (Julien et al., 1995). $Li_xV_2O_5$ was also deposited using flash evaporation (Murawski et al., 1987). The effects of different substrates, substrate temperature (T_s), oxygen partial pressure (pO_2), and post-annealing treatment (T_a) on polycrystalline V_2O_5 flash-evaporated films have been studied (Julien et al., 1995). Figure 2.5 shows the development of the O/V ratio as a function of molybdenum boat temperature (Ramana et al., 1998). T_{boat} films with the best stoichiometry O/V = 2.497 were made in the 910-980 $^{\circ}$C range. However, the deposition "quenching rate" ΔT, which is the temperature differential between the melt and the substrate ($\Delta T = T_a - T_s$), has a significant impact on the characteristics of flash-evaporated films.
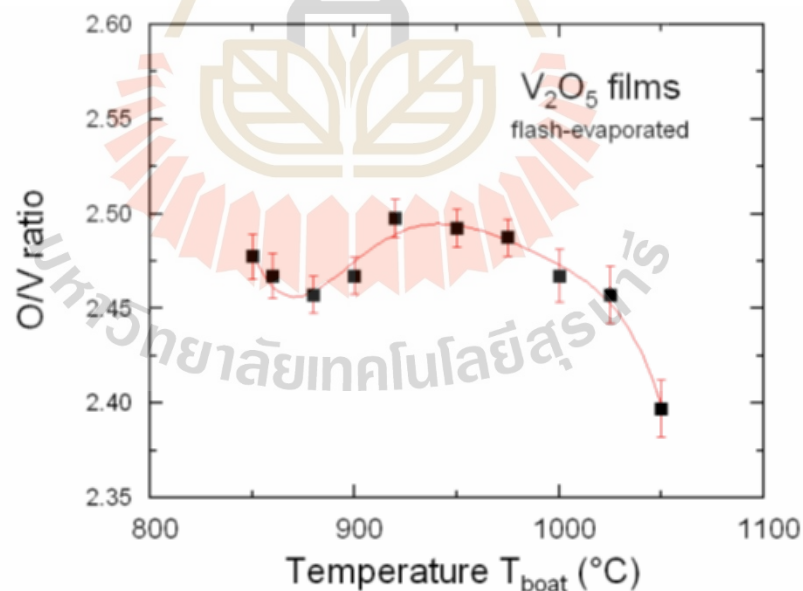
Figure 2.5 Evolution of the O/V ratio in flash-evaporated V_2O_5 films as a function of the boat temperature. (Ramana et al., 1998)

2.2.2.1.3 Chemical vapor deposition (CVD)

CVD is a flexible technology that includes an evaporator and a deposition mechanism. The precursor solution is vaporized and poured into a flash evaporation reactor. The vapor condenses in a cold-wall reactor with a substrate maintained at a constant temperature T_s in the middle zone (Vernardou, 2017). Using pure or diluted triisopropoxyvanadium oxide $VO(OC_3H_7)_3$ as a precursor, this approach has been successfully used to generate V_2O_5 films (Mantoux et al., 2004). At T_s = 300 °C, a typical V_2O_5 film 240 nm thick was produced under a total pressure of 2400 Pa with a flow of O_2 of 100 sccm. When pt drops to 1200 Pa, V_3O_7 and V_4O_7 films develop, whereas V_6O_{13} films form at T_s = 350 °C with a flow rate of 120 sccm. After post-annealing at 500 °C for 2 h in an O_2 environment with a long cooling procedure to ensure good adhesion to substrate, well crystalline films (94 nm crystallite size) were formed. PE-CVD (plasma-enhanced chemical vapor deposition) is a large-scale film deposition process. Glow discharge creates high-energy electrons that ionize gaseous molecules and produce chemically reactive ions in this process. Figure 2.6(a) shows heat-treated (500 °C for 2 h) films produced by CVD onto Pt foil that are highly structured with homogenous and smooth surfaces. L_{200} = 71 nm and L_{001} = 36 nm are the coherence domains along the a- and c-axes, respectively. Figure 2.6(b) shows the compactness of annealed V_2O_5 films in cross-section (Groult et al., 2007).

Using $VO(hfa)2H_2O$ (Hhfa = 1, 1, 1, 5, 5, 5-hexafluoro-2, 4-pentanedione) as a precursor, Barreca et al. (Barreca et al., 2000) created V_2O_5 thin films via PE-CVD. This precursor was vaporized at 70 °C at a rate of 2×10^{-4} mmol m^{-2} s^{-1} in a reactor including plasma sources of argon (constant flow rate φ = 40 sccm) and oxygen (flow rate 5 ≤ φ ≤ 20 sccm). V_2O_5 thin films grown at T_s = 200 °C with 10 sccm O_2 are highly textured (14 nm crystallite size) and preferentially develop in the (001) orientation. The organometallic vapor phase takes occur at moderate pressure (10–1000 hPa) in metal organic chemical vapor deposition (MOCVD). Watanabe et al. (Watanabe et al., 2001) employed microwave plasma MOCVD to make V_2O_5 thin films on an ITO-coated fused silica substrate. The vanadium precursor chosen was bis-acetylacetonatovanadyl, VO (acac)$_2$, $VO(C_5H_7O_2)_2$ heated at ~ 600 °C. Its vapor was introduced into the oxygen plasma that the microwave discharge produced. Other

experimental settings were as follows: the substrate was kept at Ts ≈ 300 °C, and the O_2 flow was equal to **φ** = 1.2 dm^3 h^{-1} at 650 Pa. After 15 minutes, a typical polycrystalline film with a thickness of 120 nm was formed. Vanadyl (IV) **β**-diketonate has also been employed in a low-pressure reactor with water under various settings (Barreca et al., 1999). A new vanadium (III) precursor, vanadium (III) alkoxide [V(OCMe$_2$CH$_2$OMe)$_3$], was also employed, which has a high degree of volatility at 55 °C and 200 Pa. (Crociani et al., 2011). V_2O_5–V_6O_{13} film composites with a strong (00l) orientation were produced on a fused quartz substrate at temperatures ≥ 560 °C using vanadyl acetylacetonate as a precursor. Due to the reentrant-type growth behavior, a single phase was formed for substrate maintained at Ts = 580 °C (Sahana and Shivashankar, 2004). Plasma-enhanced chemical vapor deposition was used to build V_2O_5 electrochromic coatings on flexible polymer substrates (PECVD). The breakdown of vanadium oxytrichloride (VOCl$_3$) and O_2 resulted in the formation of films at a high rate of 50 nm min^{-1} (Robbins and Seman, 2005). Nandakumar (Nandakumar and Seebauer, 2011) investigated the growth rate r_G of CVD V_2O_5 films as a function of Ts and found an Arrhenius characteristic with an activation energy of 0.14 eV; r_G = 50 nm min^{-1} at Ts ≈ 230 °C.
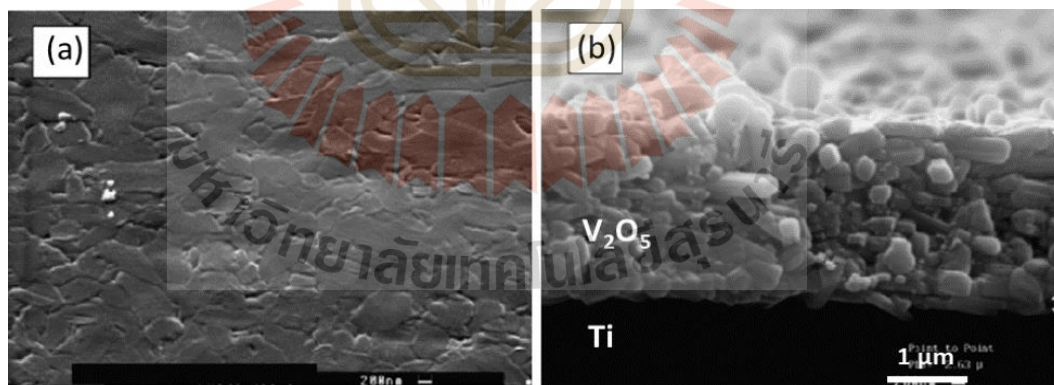
Figure 2.6 Morphology of CVD V_2O_5 films deposited onto Pt substrate. (a) SEM image of film annealed at 500 °C for 2 h and (b) cross section. (Groult et al., 2007)

     2.2.2.1.4 Sol-gel

     The sol-gel technique is a low-temperature wet-chemistry approach that involves mixing raw components at the molecular level. Wang et al. (Wang et al., 2004) looked at how post-annealing temperatures affected the structural changes of

spray-deposited $V_2O_5 \cdot nH_2O$ xerogel films. For heat-treatment at $T_a \approx 120\ °C$, films sprayed at 150 °C had large peaks in their 51V NMR spectra, indicating that the square pyramids were distorted. In comparison to contracted dry films at $T_a > 250\ °C$, the structural characteristic of $V_2O_5 \cdot nH_2O$ (with structural water) promotes lithium intercalation between the slabs. Several organizations investigated the effects of xerogel V_2O_5 film deposition conditions and post-annealing treatment. The electrochromic characteristics of $(NH_4)0.3V_2O_5 \cdot 1.25H_2O$ nanostructured films coated atop SnO_2: F (FTO) were studied by Najdoski et al. (Najdoski et al., 2014) as a function of the preparation temperature. At 50 °C, elongated aggregates with a length of 250–500 nm were formed, whereas at 85 °C, shorter aggregates (50–300 nm) were obtained. Chen et al. (Chen et al., 1998) made thin films by spin coating a sol-gel made of V_2O_5 powders, benzyl alcohol (BA), and isobutanol (IB) (molar ratio 1:40:4) heated at 110 °C for 5 hours. Wang et al. (Wang et al., 2005) used ambient conditions to make $V_2O_{5n}H_2O$ xerogel films. With a stable specific capacity of 185 mAh g^{-1} at 0.1 mA cm^{-2} current density after 50 cycles, the $V_2O_5 \cdot \frac{1}{3}H_2O$ film displayed the best Li^+ intercalation capabilities. The Raman spectra of xerogel films intercalated with lithium were examined by Cazzanelli (Cazzanelli et al., 1996). At an angular velocity of 1500 rpm, $V_2O_{5n}H_2O$ xerogel sheets ($1.8 \leq n \leq 0$) were spun-coated. The presence of water in the interlayer region has a major influence on the spectral characteristics of Li-intercalated samples, causing new Raman bands to appear at 800 and 950 cm^{-1}. V_2O_5 films deposited using a doctor blade utilizing polyol dispersion in water and acetyl acetone crystallized with the $C_{2/c}$ structure, which changed to orthorhombic Pmmn (86 nm crystallite size) after 3 hours of calcination at 170 °C (Mjejri et al., 2016). Organic (vanadium tri-isopropoxide into isopropyl alcohol) and inorganic (V_2O_5 powers in 15 wt.% H_2O_2) precursors were employed to make V_2O_5 xerogel films using the dip-coating technique (Gokdemir et al., 2014; Raj et al., 2013).

2.2.2.1.5 Magnetron sputtering

Because it allows for quicker deposition rates, the sputtering deposition process is the most used approach for growing metal-oxide layers. Its key benefit is that it produces as-deposited films with high surface uniformity. It comprises RF

magnetron sputtering (Koike et al., 1999; Batista et al., 2008; Quinzeni et al., 2011; Giannetta et al., 2015), DC magnetron sputtering (Poelman et al., 2002; Su et al., 2009; Fateh et al. 2007), and ion beam sputtering (Po (Gallasch et al., 2011). This evaporation process may be used to adjust the stoichiometry of V_2O_5 films (Silversmit et al., 2004; De Castro et al., 2013). In a plasma sputtering chamber, typical RF-magnetron sputtered V_2O_5 films are created utilizing a V_2O_5 target attacked by argon ions in a plasma of power P_w = 150–300 W. Low sputtering power P_w < 100 W may be employed for specialized applications (Raj et al., 2015). Pure argon and oxygen gases are injected at a flow rate of less than 10 sccm to achieve reactive deposition. Silversmit et al. (Silversmit et al., 2004) used reactive DC magnetron sputtering to develop V_2O_5 films on Si (100) wafers and investigated the effect of deposition settings on their stoichiometry. These tests were conducted in a vacuum of 5 x 10^{-5} Pa, with a magnetron discharge voltage of ~550 V and a plasma constant current of 150 mA. The O_2 flow rate was maintained at 3.5 sccm. Fateh et al. (Fateh et al., 2008) deposited V_2O_5 films onto (100) oriented Mg substrates and developed precise synthesis-structure correlations, demonstrating that the film deposited at 80 °C had the best crystallinity. Lourenço et al. (Lourenço et al., 1998) studied the influence of various oxygen flow rates on the structure of VO_x films and found that V_2O_5 films form at high oxygen flows (>9 sccm). For electrochromic applications, Benmoussa et al. (Benmoussa et al., 1995; Benmoussa et al., 2002) sputtered V_2O_5 thin films on Corning glass and ITO-coated glass substrates. The c-axis preferred orientation of the films produced on both substrates demonstrates that texture is substrate independent.

Yoon et al. (Yoon et al., 2004) studied the structure of V_2O_5 thin films produced on (100) Si wafers using DC and RF reactive sputtering at ambient temperature; DC-sputtered films are amorphous, but reactive RF-sputtered films crystallize with high grain size owing to the self-bias effect.
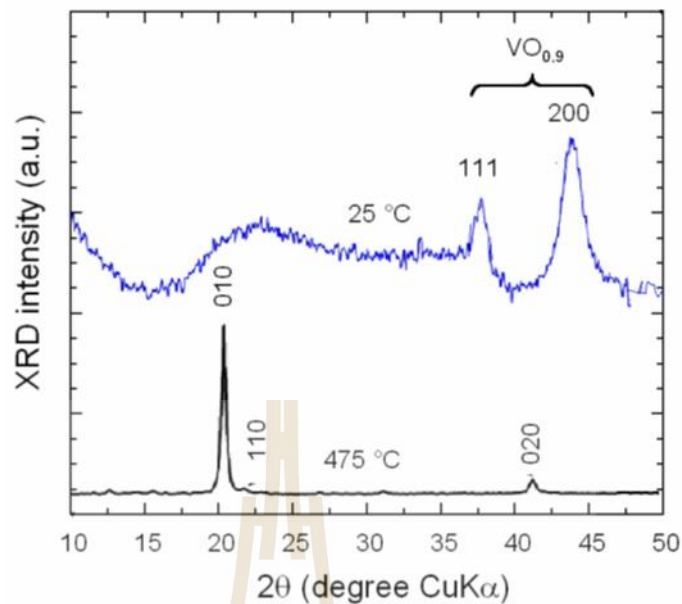
Figure 2.7 XRD diffractogram for RF sputtered V_2O_5 films (a) as-deposited at 25 °C and (b) thermally annealed at 475 °C in air for 3 h. (Giannetta et al., 2015)

Gianneta et al. (Gianneta et al., 2015) used a base pressure of 1 mPa, an RF plasma power of 200 W, and an Ar flow of 20 sccm to produce VO_x films. As-deposited films are almost amorphous, with wide XRD reflections similar to $VO_{0.9}$, but annealing at 475 °C in air for 3 h promotes the well-crystallized V_2O_5 phase with a well-developed orthorhombic form and grain size>100 nm (see figure 2.7). Ottaviano et al. (Ottaviano et al., 2004) showed better electrochromic characteristics of RF reactive sputtered films formed at low O_2 flow (2%) with the highest injected charge (49.8 mC cm^{-2}) and the largest optical density variations. Lin and Tsai (Lin et al., 2008; Lin et al., 2008) made V_2O_{5-z} films on PET/ITO (indium tin oxide) flexible substrates. After 200 cycles, oxygen-deficient V_2O_{5-z} films (z = 0.13) with a transmittance variance of 36.5% were produced under a chamber pressure of 6 Pa with Ar and O_2 flow rates of 4 sccm. Kang et al. (Kang et al., 2013) used electron-beam irradiation amorphous films generated by RF sputtering at 200 W at 1 nm min^{-1} growth rate on an alumina substrate to make nanorod-like V_2O_5 films.

2.2.2.2 Characterization of V_2O_5 thin films were prepared by magnetron sputtering

Quinzeni et al. (2011) studied the structural, morphological, and electrochemical features of nanocrystalline V_2O_5 thin films produced by radiofrequency magnetron sputtering: V_2O_5 nanocrystalline thin films are especially appealing as cathode materials for all-solid-state rechargeable lithium microbatteries due to their ease of manufacture and high energy density. Their electrochemical properties, on the other hand, are inextricably linked to the film microstructure, which is in turn linked to the nature and parameters of the deposition method. As a result, the fabrication of thin films with repeatable electrochemical characteristics remains a challenge. They describe the deposition of V_2O_5 crystalline thin films utilizing a vanadium metal target and reactive radiofrequency magnetron sputtering. Different substrate temperatures and deposition periods were used. The structural and morphological characteristics of the films were investigated using X-ray powder diffraction (XRD). The crystallographic orientation of the films is affected by the deposition conditions, according to XRD analysis. Thin samples (approximately 100 nm) generated at 300 °C have a h 0 0 orientation, while larger films have a 1 1 0 favored growth. Regardless of deposition duration, films formed at 500 °C have a 0 0 1 orientation. The h 0 0-oriented V_2O_5 thinner films, with the ab plane aligned perpendicular to the substrate, show reversible Li intercalation/deintercalation processes and high specific capacity. The cycling behavior in this scenario is quite promising, with a steady capacity more than 300 mAh g^{-1} provided for at least 70 cycles in the potential range 3.8–1.5 V at 1C rate.

Table 2.2 Deposition conditions, thickness and rugosity of the V_2O_5 thin films (Quinzeni et al., 2011).

Sample	t (h)	T (°C)	Film thickness (nm)	Film rugosity Rrms(nm)
V_2O_5-a	3	300	127	96
V_2O_5-b	3	500	200	126
V_2O_5-c	7	300	320	160
V_2O_5-d	7	500	500	250
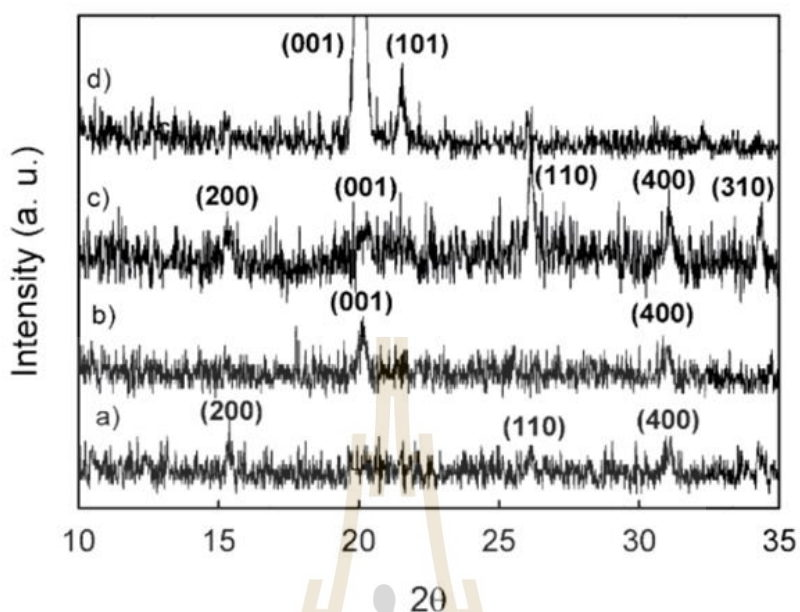
Figure 2.8 XRD patterns of V_2O_5 films deposited at different deposition times and temperatures. (Quinzeni et al., 2011)
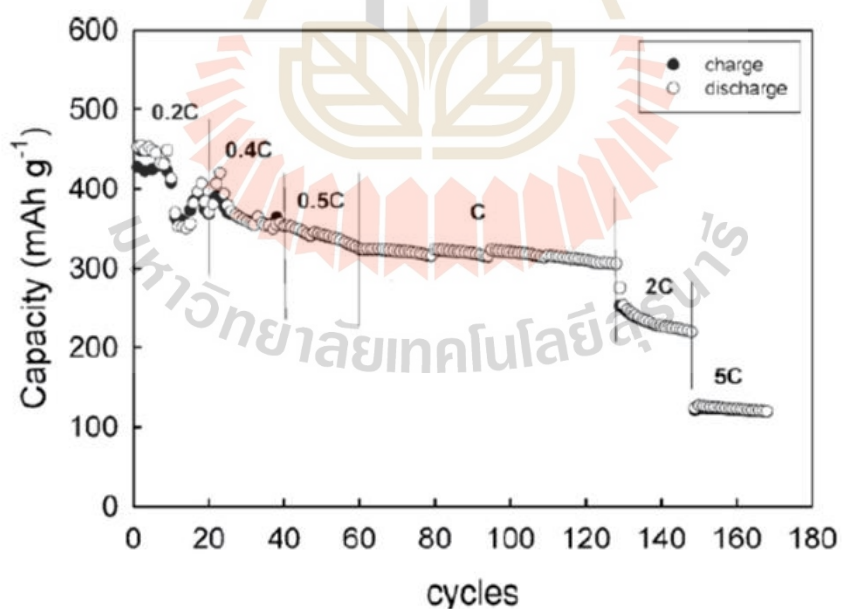
Figure 2.9 Cycling behaviour for the V_2O_5 a thin film at different current regimes in the potential range 1.5–3.8 V. Liquid electrolyte: EC/DEC (1/1 v/v)–LiPF$_6$ (1 M). (Quinzeni et al., 2011)

At room temperature, Marcelo S.B. de Castro (De Castro et al., 2013) investigated vanadium oxide thin films generated by magnetron sputtering from a V_2O_5 target: RF magnetron sputtering of vanadium oxide thin films from a V_2O_5 target at ambient temperature was used as an alternate method of producing vanadium oxide thin films for infrared detector applications. In an argon–oxygen environment, the films were deposited on glass substrates with an oxygen partial pressure ranging from 0% to 20% of total pressure. X-ray diffraction (XRD) and X-ray photon spectroscopy (XPS) analysis revealed that the films were a combination of numerous vanadium oxide compounds (V_2O_5, VO_2, V_5O_9, and V_2O_3), with varying hues ranging from yellow to black depending on composition. The thermal coefficient of resistance (TCR) ranged from -0.02 to -2.51 % K^{-1}, while the electrical resistivity ranged from 1 mX cm to more than 500 mX cm. Bolometers are thermal detectors that use the temperature dependence of electrical resistivity as a physical characteristic. The temperature coefficient resistance (TCR) is the figure of merit used to measure this parameter, which is defined as follows: TCR = (1/R) x (dR/dT)
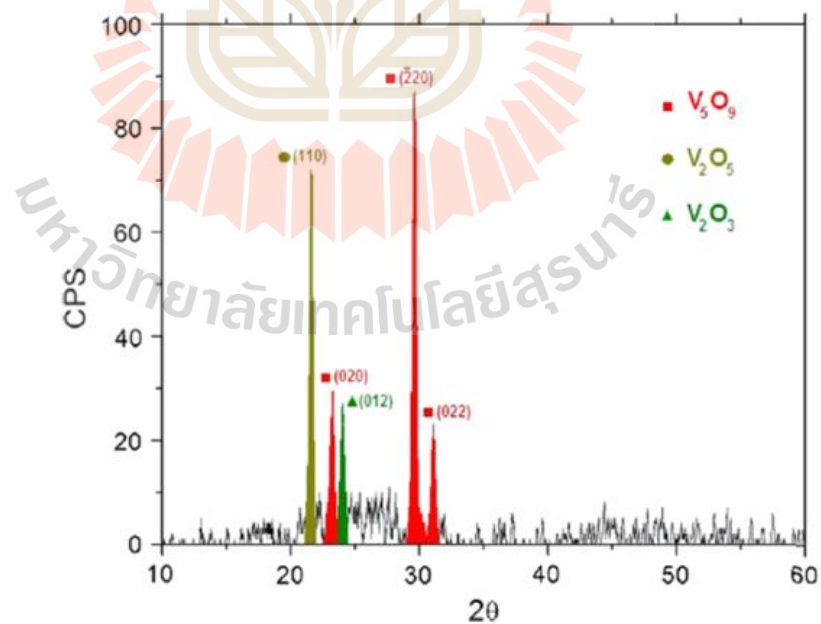
Figure 2.10 XRD characterization of samples produced on a glass substrate at room temperature in a 100% argon atmosphere. The background was subtracted to emphasize the peaks. (De Castro et al., 2013)
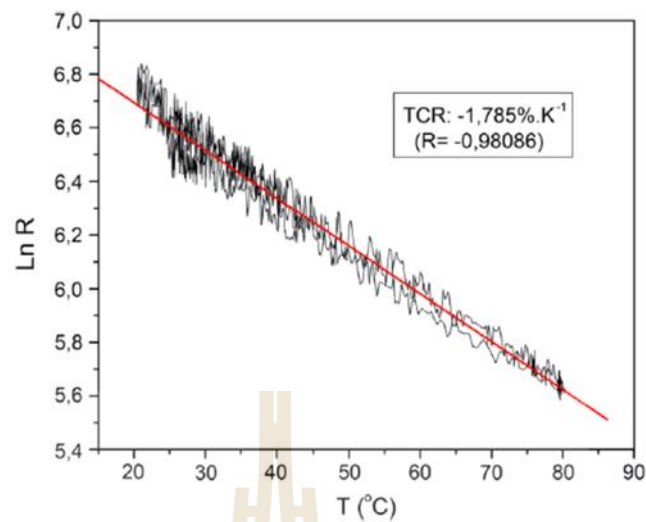
Figure 2.11 TCR measurement of samples produced on a glass substrate at room temperature in a 100% argon atmosphere. The TCR was calculates by linear regression with a correlation coefficient (R) of -0.98086. (De Castro et al., 2013)

Dwight Acosta (Acosta et al., 2016) looked at V_2O_5 thin films formed by RF Magnetron Sputtering: Oxygen Content's Effect on Physical Properties: RF Magnetron sputtering with a V_2O_5 target was used to develop Vanadium Oxide thin films on glass and FTO/Glass substrates without and with an O_2 (10% concentration) environment in the deposition chamber, respectively. EDS (Energy dispersive spectroscopy) and XRD (X-rays diffraction) were used to investigate the impact of O_2 on compositional, structural, electrical, and optical characteristics. Figure 2.12 shows the XRD pattern of a film made with a 10% O_2 concentration and deposited at room temperature, which has diffraction peaks recorded in card number 00-045-1074 (I) from the JCP2.2CA data set. The molecule is recognized as a tetragonal β-V_2O_5 phase with lattice parameters of a = 14.259 Å, b = 14.259 Å, and c = 12.576 Å. Low-intensity diffraction peaks that might correlate to a VO_2 were identified in several other XRD (X-rays diffraction) patterns of their samples, which were not shown in this study. , UV-Visible Spectroscopy in figure 2.13(b) shows that V_2O_5 samples deposited on glass have a higher transmittance than those deposited on FTO/Glass, although with reference to graphics shown in figure 2.13(a), the last samples had higher transmittance values for all wavelengths considered. Because of their thickness, the deposited V_2O_5/FTO films have a lower transmittance, but coating transmittance has the same wavelength

dependency. to investigate electric surface characteristics, as well as the Four Points approach. Rapid changes in electrical resistance when the films were heated to roughly 255 °C indicate a phase transition from semiconductor to metallic. Under an external voltage, the β-V_2O_5 films exhibit electrochromic activity, although Cyclic Voltammetry measurements show that the electrochromic characteristics are not long-lasting.
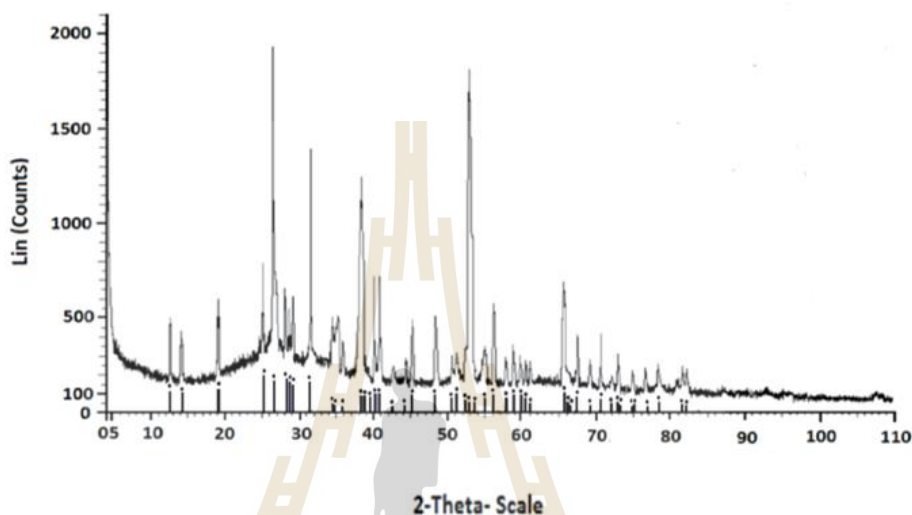
Figure 2.12 A XRD pattern from a V_2O_5/FTO film deposited at room temperature. The peaks marked with blue short lines correspond to the β-V_2O_5 reflections reported in card number 00-045-1074 (I) from the JCP2.2CA data base. (Acosta et al., 2016)
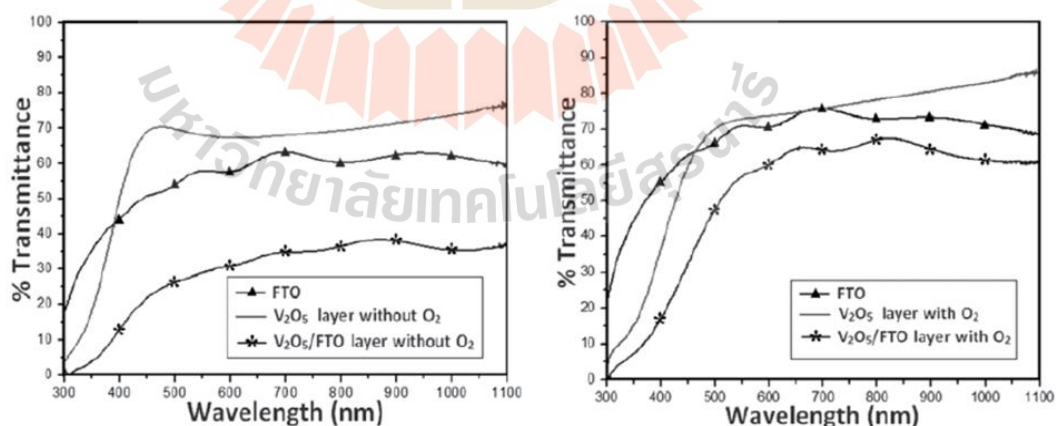
Figure 2.13 (a) Optical transmittance spectra from V_2O_5 samples deposited on glass and on FTO/Glass respectively without O_2 (b) Optical transmittance spectra from FTO/Glass and V_2O_5 samples prepared on glass and on FTO/Glass respectively with O_2. (Acosta et al., 2016).

2.2.3 Application of V$_2$O$_5$ films as an electrode material for electrochromic properties

An electrochromic layer, an electrolyte layer, and an ion storage layer make up a standard electrochromic device (ECD). On transparent substrates covered with transparent conductive film, both electrochromic and storage layers are deposited. ECDs work by varying the optical characteristics of various hues. In ECDs, V$_2$O$_5$ is used as a counter electrode material (Mjejri et al., 2016; Iida et al., 2008; Najdoski et al., 2014; Wruck et al., 1989; Talledo et al., 1990; Guan et al., 1998; Kaid, 2006; Benmoussa et al., 2008; Rosaiah and Hussain, 2013). It produces electrochemical redox reactions that balance charge transfer at the electrochromic working electrode during optical switching. The twofold injection of ions and electrons may be used to describe the usual electrochromic process of V$_2$O$_5$ (Eq 2.1). (Chen and Ho, 2001) define the transmittance variance (ΔT) as follows:

$$\Delta T\ (\%) = T_{bleached} - T_{colored} \tag{2.1}$$

where T$_{bleached}$ and T$_{colored}$ are the transmittances (in %) of bleached and colored states, respectively.

According to Sarminio et al. (Sarminio et al., 1993), the stress shift in the crystalline layer and the electrochromic characteristics are closely related. Tensile stress changes with x(Li) composition, with the δ-LiV$_2$O$_5$ phase being the highest. In the ECD cell, a V$_2$O$_5$ thin film electrochemically produced on ITO glass from a poly-vanadic acid sol was employed (Yoshino et al., 1987). The cell was tested over 8 x 10^4 times, with a reaction time of 2–20 seconds depending on the cell voltage.

Shimizu et al. (1990) created an electrochromic display device employing a V$_2$O$_5$ thin film produced by spin coating of V$_2$O$_5$ powder soaked in a mixture of benzyl alcohol and iso-butanol. The films deposited onto ITO glass and annealed at T$_a$ > 300 °C are crystalline and have high electrochromism reversibility. The creation of micrometric crystallites in mesoporous V$_2$O$_5$ films generated by hydrolysis of vanadium tri-isopropoxide in the presence of polyethylene glycol (PEG) has been proven to be beneficial for the development of advanced ECDs (Cremonesi et al., 2006). At the 400

nm absorption edge, V_2O_5 thin films formed by microwave plasma MOCVD had a transmittance of 70%. A change in the film color from yellow (V_2O_5) to blue (LiV_2O_5) happens during the reversible Li intercalation process (Watanabe et al., 2001). By modifying the surface structure of the V_2O_5 electrochromic thin film using the organic–inorganic template 3-isocyanatopropyltriethoxysilane (ICS) and poly (propylene glycol) bis-2(ammino-propyl-ether) (2-APPG), the storage capacity and diffusivity of Li^+ ions may be increased (Lin et al., 2008). At an oxygen flow rate of 2 sccm, magnetron sputtered V_2O_{5-z} thin films onto flexible polyethylene terephthalate/indium tin oxide (PET/ITO) substrates were oxygen deficient with z = 0.169 and provided 43.3 % light modulation. An optical density changes and color efficiency of 0.38 and 102.5 cm^2 C^{-1} were observed after 200 cycles at a wavelength of 400 nm, respectively (Liberatore et al., 2006). Lin and Tsai (Lin and Tsai, 2008) developed similar ECD devices at 23 ^{o}C, with an oxygen deficit z = 0.13 and a transmittance modulation of 36.5% at 400 nm. Recent research reveal that titanium-doped V_2O_5 thin film electrochromic devices (Lu et al., 2013) and spray-deposited lithium-doped V_2O_5 electrochromic devices (Lu et al., 2013) may achieve high switching speeds and colouring efficiency (Kovendhan et al., 2015). The ammonium intercalated V_2O_5 xerogel thin film produced at 50 and 85 ^{o}C shows two color shifts linked to the redox process of V^{4+}/V^{5+} states: yellow/green and green/blue (Najdoski et al., 2014).

Electrochromic switching devices, as researched by R. L. Ying (Lu et al., 2015), have attracted a lot of interest since thin films are one of the most promising materials for energy-saving applications. Because just a single-layer film of this material is required for coloring, the vanadium oxide system is simple and economical. Electrodeposition of vanadium dioxide thin films on a potentiostat/galvanostat was used to create them. With an ITO substrate, a traditional three-electrode cell was used. A 1:1 combination of deionized water and ethanol containing 1 M $VOSO_4 \cdot xH_2O$ was used to electrodeposit V_2O_5 thin films. Electrodepositions were carried out for 20, 40, and 60 seconds at -0.7 V against the reference electrode. In a 1 M $LiClO_4$ solution including propylene carbonate, the lithium-ion intercalation/deintercalation characteristics of the V_2O_5 material were examined. Using a potentiostat/galvanostat, cyclic voltammetry was conducted between -1 and +1.25 V (versus Pt) at a scanning

rate of 0.025 V s^{-1}. At room temperature, chronoamperometric measurements were taken at a constant voltage of +0.5 V and the current change was recorded for 45 s. Figure 2.14 displays a scanning electron microscope (SEM) image of the surface morphology of the electrochemical development of V_2O_5 thin films. As demonstrated in figure 2.10, the V_2O_5 thin films deposited for 20 seconds were generally smooth and adhered well to the substrate (Figure 2.14(a)). The shape of the V_2O_5 thin films altered dramatically as the deposition period rose to 40 and 60 seconds (Figure 2.14(b), (c)). The V_2O_5 thin films' shape altered from smooth to typical sea-island morphology. The electrochemical development of V_2O_5 thin films was determined using cross-sectional SEM images (Inset of figure. 2.14 (a)–(c)), yielding thicknesses of 321, 621, and 1047 nm for deposition durations of 20, 40, and 60 s, respectively.
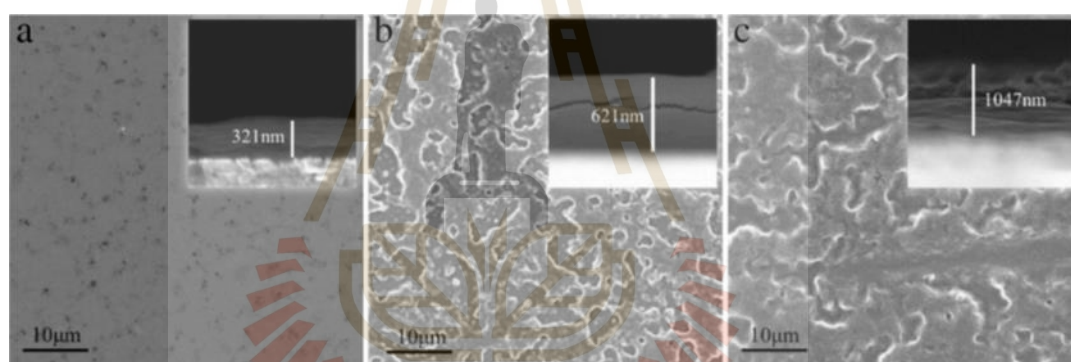
Figure 2.14 SEM image of V_2O_5 electrode deposited for a=20, b=40, and c=60 s.

With a scan rate of 0.25 V s^{-1}, cyclic voltammetry and chronoamperometry were used to explore the Li insertion/extraction behavior in a 1 M $LiClO_4$ propylene carbonate solution. In the potential range of -1 to 1.25 V, Figure 2.15(a) illustrates typical cyclic voltammograms of V_2O_5 electrodes with varied deposition times. At V_2O_5 electrodes, the electrochemical Li$^+$ insertion process may be represented as V_2O_5 + x Li$^+$ + xe$^- \longleftrightarrow$ Li$_x$V$_2$O$_5$ (Wei et al. 2012; Chen et al., 2011), this is accompanied by a shift in hue. Coloration occurs as a result of these processes [yellow$\longrightarrow$green$\longrightarrow$blue (Inset of figure 2.15(c))]. Chronoamperometric tests suggest that the thin V_2O_5 film exhibits quicker lithium-ion intercalation and deintercalation than the thick V_2O_5 film, which benefits the coloration rate. Despite extensive study into the synthesis of vanadium oxides, the monitoring of electronic and atomic structures throughout the

development and coloring of this material has received little attention. In situ XAS at the V K-edge was done during the electrochemical reaction to get insight into the impact of delithiation/lithiation on the oxidation states of vanadium as well as the local atomic structure of the V_2O_5 thin films. While the thinner film (deposited for 20 seconds) demonstrates a quicker rate of coloring than the thicker film (deposited for 60 seconds), the thicker film is more stable. Thus, Figure 2.16 shows the XAS spectrum of a 60 s of V_2O_5 film. The insets show the pre-peak intensities during the delithiation (left panel) and lithiation (right panel) processes, respectively. Notably, two significant modifications in the pre-edge region's spectral characteristics generated by Li-ion intercalation were observed: a shift of the pre-edge peak position to the lower energy and a decrease in pre-edge peaks. The transition to low energy was linked to the lower oxidation state of metal ions as a result of Li-ion intercalation, which can be philosophically explained by the metal ions' reduced effective nuclear charge as their oxidation state decreases. The intensity of the pre-edge peak definitely reduced for bias potentials ranging from 0 to -0.6 V, indicating that the local structure around the V atom became more symmetrical as a result of Li-ion intercalation. However, when lithium is extracted at a bias potential of -0.6 to +0.6 V, the coloration of the film changes from deep blue to green to yellow. When the film is oxidized at -0.3, 0, and 0.6 V, the pre-edge peak of the V K-edge transitions to a high energy state, converting partial V^{4+} ions to V^{5+}. At 0.6 V, the remaining V^{4+} ions decreased to V^{5+}. The positive shift in the V K-edge implies that vanadium average oxidation state rose as a result of the nucleus's attractive potential increasing. Additionally, the rise in the pre-edge peak size correlates with the decreasing lithium concentration, indicating that the structural symmetry was changed from Oh (V^{4+}) to a combination of Py (V^{5+}). Without the in situ electrochemical cell, it is impossible to collect the atomic/electronic structural information mentioned above. In general, our findings underscore the critical importance of in situ X-ray spectroscopic characterisation of energy materials' atomic/electronic structures in their operating state. This work advances our knowledge of the electrical and atomic characteristics of the vanadium oxide system formed by electrochemical deposition and contributes to the development of electrochromic materials for possible energy-saving applications.
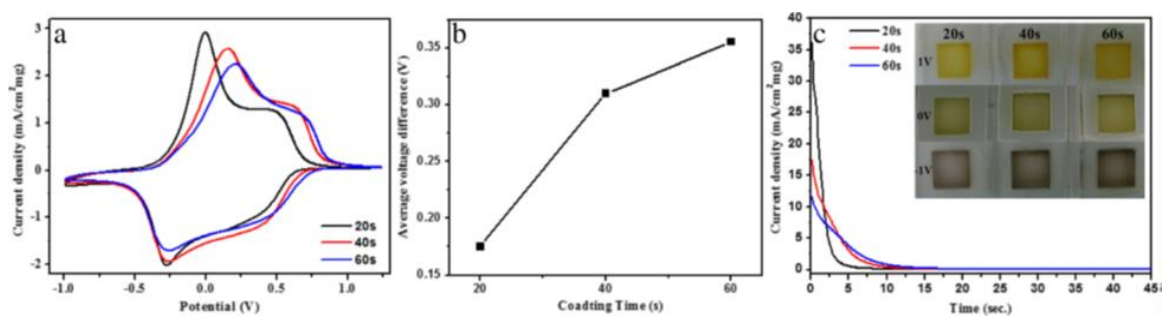
Figure 2.15 (a) Cyclic voltammograms of electrodeposited vanadium oxide films for lithium intercalation/deintercalation. (b) The average voltage difference between the cathodic and the corresponding anodic double peak of the redox reactions. (c) Chronoamperometry of vanadium oxide films.
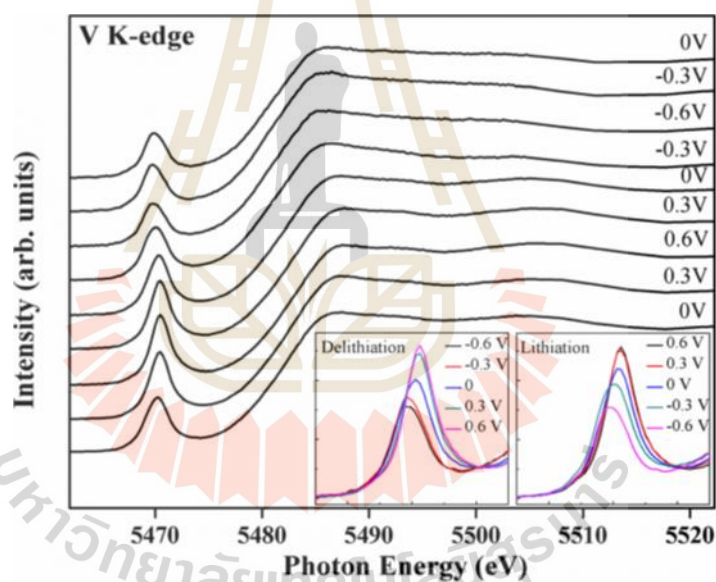
Figure 2.16 In situ XAS at V K-edge for 60 s at applied potentials in the order of 0.0, 0.3, 0.6, 0.3, 0, −0.3, −0.6, −0.3, and 0 V. Insets display the enlargements of pre-peak intensities during delithiation (left) and lithiation (right).

2.3   WO₃ Structure and Bonding

Tungsten has a long and illustrious history that dates back to its discovery in the 18th century. Peter Woulfe was the first to discover a new element in wolframite, a naturally occurring mineral. Tungsten was once known as wolfram, which explains why its elemental symbol is "W." Carl Wilhelm Scheele was a Swedish scientist who studied the mineral scheelite and also contributed to its discovery. In 1841, Robert Oxland, a chemist, published the first techniques for manufacturing tungsten trioxide and sodium tungstate. Soon after, he received patents on his work, and he is widely regarded as the father of systematic tungsten chemistry. Many transition metal oxides have been used in a variety of hard disciplines such as information science, nano and microelectronics, computer science, energy, transportation, safety engineering, military technologies, optoelectronics, and electrochromic devices throughout the last several decades. Wrought iron trioxide (WO_3) is one of the most intriguing transition metal oxides, displaying a wide range of unique characteristics, particularly in thin film form, which is beneficial for advanced technological applications. It features structural changes and sub-stoichiometric phase transitions, which have drawn the attention of researchers in the field of display systems and microelectronics in recent years to investigate their potential scientific and technical applications (Granqvist, 2000).

Wrought iron trioxide is one of the most intriguing transition metal oxides, displaying a wide range of unique characteristics, particularly in thin film form, which is beneficial for advanced technological applications. It shows structural alterations and sub-stoichiometric phase transitions, which have piqued the interest of researchers in the domains of display systems and microelectronics in recent years. It has electrochromic qualities that make it useful for changeable reflection mirrors, dazzle-free mirrors in autos, variable sun protection systems (variable transmittance), and satellite thermal control surfaces with adjustable emittance. It is a substantial chromic substance that may be colored by electrochromism, photochromism, gas chromism, laser chromism, and thermochromism techniques.

Electrochromic (EC) materials have the ability to modulate emissivity. WO_3 is the most researched electrochromic material, particularly in its amorphous form. When intercalated with Li^+ or H^+ ions, crystalline WO_3 exhibits a shift in optical constants

throughout a large spectral range in the visible and infrared (IR) regions, while being less investigated. The RT blackbody spectrum has a peak at 9.7 mm, and 94.5% of the radiated power from a blackbody falls between 2 and 40 mm. As a result, the emissivity modulator for thermal management of an RT satellite should be designed for operating in this range. Some infrared (IR) devices have been documented, however they are typically employed in a very narrow range in the near infrared (NIR) (DeVries et al., 1999). Tungsten oxides have been the most investigated inorganic materials. Until date, the maximum coloring efficiency (CE) in the visible area of the electromagnetic spectrum has been found in amorphous WO_3 films. These films can only be employed in lithium-based electrolytes due to their high breakdown rate in acidic electrolyte solutions, resulting in longer response times. Furthermore, even with Li^+ systems, extended longevity has yet to be established. Because of their quick response times and high contrast ratios, inexpensive conducting and redox polymers have gotten a lot of attention as electrochromic materials. Multiple coloring in the visible spectral band and low UV stability are drawbacks (Lee et al., 2006).

The cubic perovskite-like structure of tungsten trioxide is based on the corner sharing regular octahedra with the oxygen atoms at the corner and the tungsten atoms at the center of each octahedron. The crystal network is formed by the regular placement of O and WO_2 planes in each primary crystallographic direction. Actually, two distortions reduce the symmetry of WO_3 from the ideal ReO_3 structure: tilting of WO6 octahedra and displacement of tungsten from the center of its octahedron. The temperature affects the crystal structure of tungsten trioxide (Figure 2.16). (Weckhuysen et al., 2000). It is tetragonal above 740 $^{\circ}$C, orthorhombic between 330 and 740 $^{\circ}$C, monoclinic between 17 and 330 $^{\circ}$C, and triclinic between -50 and 17 $^{\circ}$C.
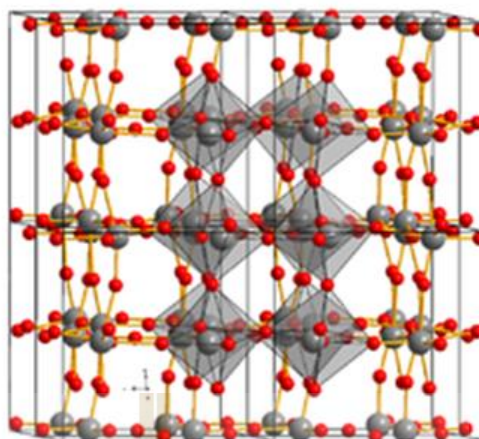
Figure 2.17 The structure of WO_3 (Granqvist, 2000).

Table 2.3 The physical properties of WO_3.

Crystal structure	monoclinic
Molar mass	231.84 g/mol
Density	7.16 g/cm^3
Appearance	Canary yellow powder
Melting point	1473 $^\circ$C
Boiling point	1,700 $^\circ$C

Tungsten oxide (WO_3), a transition metal oxide, has a variety of fascinating optical, electrical, structural, and defect properties. Interest in this substance dates all the way back to 1837, when Wohler discovered the mineral's great metallic luster in $LiWO_3$. He hypothesized that the brilliance was the result of metallic alloy production and created the name "tungsten bronzes." Mott, Sienko, and others conducted extensive experimental and theoretical work on single crystals of Na–tungsten bronzes in the 1950s and 1960s due to their remarkable electrical characteristics, including metal–insulator phase transitions and superconductivity at very low temperatures. In the mid-1960s, in an attempt to discover an inorganic material capable of reversible colouring and bleaching (photochromism), we started investigating thin films of MoO_3 and WO_3 (Deb and Chopoorian, 1966; Deb, 1968). This resulted in the finding of

photochromism in extremely disordered thin films of these materials, followed by the electrochromic (EC) phenomenon. The EC effect was first shown using surface electrode geometry, a unique device arrangement that may be quite helpful for understanding the kinetics of colouring processes. This was quickly followed by a totally reversible thin-film layer structure composed of M-SiO-WO_3-TCO, which inspired a large number of subsequent device topologies (Deb, 1969; Deb, 1973; Deb, 2008). Numerous technology advancements have resulted in the creation of a variety of intriguing gadgets, most notably the first commercially produced EC "smart window," which has the potential to have a significant impact on the energy saving. Extensive study on a variety of different transition metal oxides has resulted in the publication of various books (Granqvist, 1995; Monk et al., 1995) and review papers on the topic (Bange, 1999; Granqvist, 2000). WO_3 has been the most widely investigated material so far, not just for chromogenics, but also for a range of other device applications. Apart from technological development, significant study has been done on the physical and chemical characteristics of WO_3 as a prototype material, which is of huge scientific interest. A quick outline of some of the most significant research difficulties and prospects in the science and technology of WO_3 for chromogenic and related applications will be provided.

Amorphous tungsten trioxide is one of the most desirable electrode materials for electrochromic windows, driving mirrors, displays, and other devices that need active films (Granqvist, 1995). Coloration happens as a result of the introduction of a tiny cation, such as Li^+, through an electrochemical process (Faughnan, 1975):

$$WO_3(Bleached)+xLi^++xe^- \leftrightarrow Li_xWO_3(blue) \tag{2.2}$$

Despite intensive research on this subject, the impact of cation insertion on the local structure of amorphous WO_3 remains a point of conflict. Wang et al. (Wang et al. 1999) reported an increase in the crystallinity of amorphous WO_3 formed through sputtering with hydrogen insertion using transmission electron microscopy and electron diffraction. This should be followed by an increase in the length of the W–O bond, since the mean interatomic distance in amorphous WO_3 is known to be shorter than that in crystallized WO_3 (Pauporté et al., 2003). This behavior is consistent with the

findings of Kuzmin and Purans (Kuzmin and Purans, 1993) who examined the structural properties of the first oxygen shells acquired from ex-situ extended X-ray absorption fine structure (EXAFS) analysis of a bleach film and a film colored in acidic solution (H^+ insertion). They discovered a much higher mean interatomic distance between W-O in the latter instance. They hypothesize that the observed structural alterations are due to the creation of small-radius polarons. These findings contradict those of Yang and Yao (Yang and Yao, 2000), who examined the EXAFS spectra recorded ex-situ on two distinct films: one that had been bleached and one that had been colored with 0.1 M $LiClO_4$ + propylene carbonate (PC) solution. Under coloring, the first peak in the Fourier transform (FT) of the EXAFS oscillations, which corresponds to the first W–O distances, moves to a smaller value. The authors determined that lithiation caused the lattice to compress. These findings demonstrate the unreliability of ex-situ measurements, most likely because the redox behavior of tungsten in colored WO_3 films exposed to a synchrotron X-ray beam and in air is dubious. To overcome this obstacle and precisely regulate the film's redox state under X-ray irradiation, an electrochemical cell may be employed and in situ measurements at a controlled voltage can be performed. XAS is one of the few techniques available for exploring the local structure of these disordered molecules. When compared to previous in situ XAS investigations of structural changes generated by small ion intercalation in amorphous oxide (Hüppauff and Lengeler, 1993; Pauporté et al., 1999; Mo et al., 2000), the current system faces two significant new challenges: (i) the first Fourier transform peak requires at least two distinct distances for a satisfactory fit (Pauporté et al., 2003; Kuzmin and Purans, 1993); (ii) due to the high coloration efficiency of amorphous WO_3, the range for electrochromic application (reversible deep coloration/decoloration) is narrow, ranging between 0 and 0.5, and small structural variations are expected.

2.3.1 WO_3 thin films by magnetron sputtering and electrochromic application

A. Kuzmin and J. Purans (Kuzmin and Purans, 1993) explored local structural changes in amorphous tungsten trioxide (WO_3) thin films subjected to coloration in an acid aqueous solution using the x-ray absorption spectroscopy technique. Thermal

evaporation of WO_3 powder in a medium vacuum over a polyimide substrate at two different temperatures T_s = 340 and 390 K produced amorphous WO_3 thin films. The XANES findings from this experiment demonstrated that the difference in XAS between clear and colored WO_3 thin films is already noticeable in a comparison of x-ray absorption near-edge structures (XANES) (Figure 2.18). For colored films, (i) the edge is displaced to lower energies by roughly 1.5-1.8 eV, and (ii) the amplitude of the 'white line' is somewhat increased. The first effect was anticipated and is simply explained by the lower charge of the portion of the colored film's absorbing tungsten atoms. The shift is determined by a number of parameters, including the concentration of colored centers, charge transfer effects, the symmetry of the absorbing center, and the distance between tungsten and oxygen in the initial coordination shell. Calculations for the free tungsten ion in the 6+ and 5+ states indicate that an energy difference of around 10 eV is expected for the $2p$ to $5d$ atomic transition, which is much more than the observed value. This indicates that the bonding action with oxygen ligands has a strong impact and that the concentration of 5+ colored centers is not dominating. The findings of the single XANES experiment were unable to offer detailed information on the local structure of WO_3. The white line peak may be the result of a combination of several coordinations or a somewhat broad spread of crystal fields around tungsten. This implies a major modification of the local structure of the W atom, particularly for coordinated oxygen atoms around the W atom. This will be explored in further detail in the EXAFS section. There are three distinct peaks in the FT of the WFS (W-fourier transform) signals, which can be attributed to single-scattering (ss) processes in the first coordination shell formed by oxygen (the peak at 0.7-1.9 Å), to the multiple-scattering (MS) contribution from the first shell (the peak at 2.2-2.9 Å), and to the complex contribution from the SS plus MS signals in the second coordination shell formed by tungsten and distant oxygens (the peak at 2.9-4.2 Å). Due to the fact that the FTS have not been adjusted for photoelectron phase shift, the locations of the peaks in Figure 2.19 (b) do not correspond to the genuine crystallographic values. To determine which signal is responsible for the difference between the EXAFS spectra of clear and colored films, we computed the back FTS in the three ranges stated before, and the result is given in figure 2.20. As can be seen, the first shell has the greatest variance in the

frequency of the EXAFS curves. Take note that a higher frequency equals a greater distance. Thus, comparative study of the experimental spectra demonstrates that the coloring process results in local structural changes, namely an increase in the average tungsten-oxygen bond length. To determine the magnitude of the effect, the multi-shell best-fit approach was used to analyze the experimental data from the first shell qualitatively. Additionally, we will use the words 'one-component', 'two-component', and 'multi-component' models to denote the number of crystallographic coordination shells and separate WAFS signals employed in the fitting approach to characterize the experimental data. To begin, we fitted both signals using the one-component model to get the parameters' average values. This strategy is conceivable since the form of the experimental signal is not as beat as it is for WO_3 (Balerna et al., 1991). As a consequence, both the average distance ((R)) and the Debye-Waller factor ((σ^2)) values increase with coloring and are equal to $(R) = 1.767$ Å and $(\sigma^2) = 0.0038$ Å^2 for the clear film and $(R) = 1.7928$ Å and $(\sigma^2) = 0.0051$ Å^2 for the colored film, respectively. Given that only a portion of the tungsten ions convert to the W^+ state, we determined the approximate ratio W/W^+ using the ratio of the coordination numbers retrieved from the two-component fitting approach for the colored film's first-shell EXAFS signal.
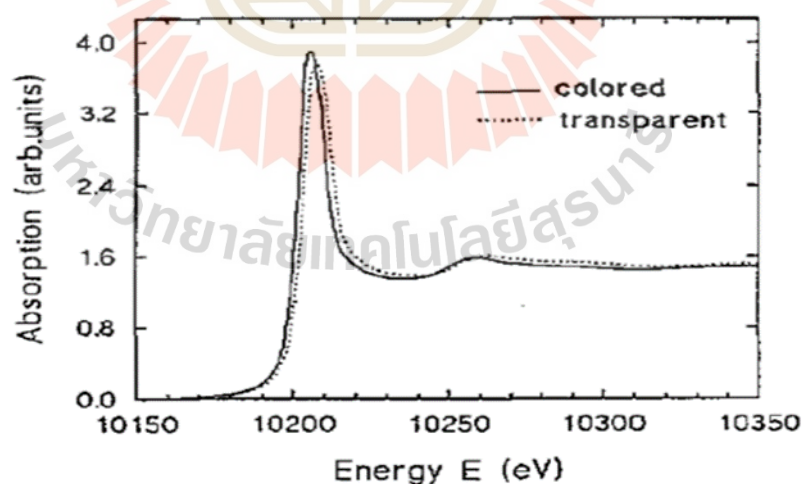
Figure 2.18 Experimental x-ray absorption spectra of the W L_3-edgc in transparent (dotted curve) and colored (full curve) WO_3 thin films. (Only the XANES region is shown. (Kuzmin and Purans, 1993))
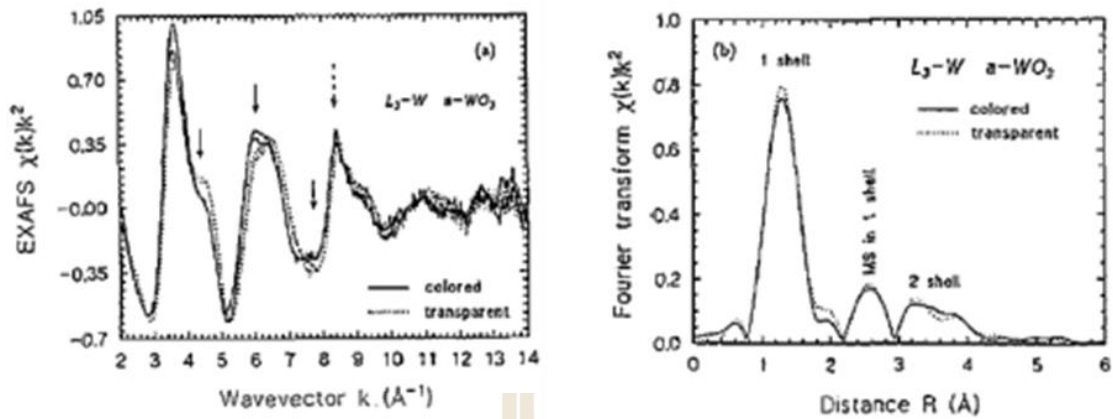
Figure 2.19 (a) Experimental EXAFS $\chi(k)k^2$ spectra of the W L_3-edge in WO_3 thin films for two samples before (dotted curve) and immediately after coloration (full curve). Two spectra for each case correspond to different samples. The full arrows indicate the main observed difference. The broken arrow marks the position of the double excitation 2p4d to 5d5d. (b) Fourier transforms of the W L_3-edge EXAFS $\chi(k)k^2$. Dotted curve: transparent film; full curve: colored film. (Kuzmin and Purans, 1993)
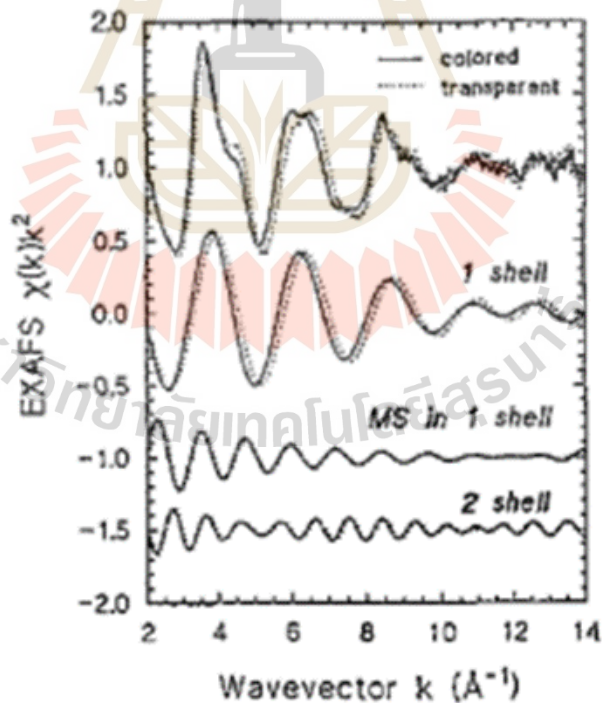
Figure 2.20 The separate contributions to the experimental signals (upper curves) From the scattering processes inside the first two shell. Dotted curve: transparent film; full curve: colored film. (Kuzmin and Purans, 1993)

T. Pauporte et al. (Pauporté et al., 2004) investigated the effect of Li^+ electroinsertion into amorphous sputtered WO_3 thin films deposited using dc magnetron reactive sputtering on two different substrates: F-doped SnO_2 conducting glass for the electrochemical study and high purity carbon substrates for the in-situ XAS study. The electrochemical cell utilized in this experiment is described in further detail elsewhere (Pauporté et al., 1999). It was filled with a 0.3 M solution of $LiClO_4$ and propylene carbonate. A sheet of Toray paper served as the counter-electrode. In the electrochemical cell, a pseudo Ag–AgCl reference was inserted directly. Three distinct potentials, +0.66, -0.84, and -1.04 V versus SHE, have been studied. They correlate in Li_xWO_3 to x = 0, 0.32 and 0.45, respectively, as determined by electrochemical and chemical titration. With lithiation, shifts in the locations of the tungsten L_I and L_{III}-edges toward lower energies are detected, which are attributable to the reduction in the W oxidation state. On the extended X-ray fine structure (EXAFS) spectrum, significant changes are also seen. The examination of initial oxygen shells clearly demonstrates that lithiation results in an increase in the mean W–O interatomic distances that is not attributable to a crystallization process triggered by the cathodic reaction.
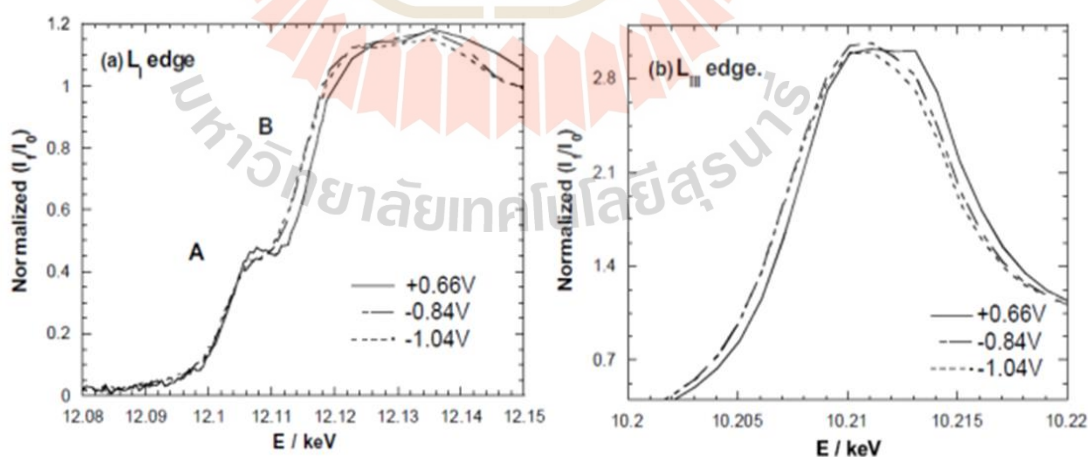
Figure 2.21 Variation of W L-edges with the applied potential. (a) L_I edge and (b) L_{III} edge. (Pauporté et al., 2004)
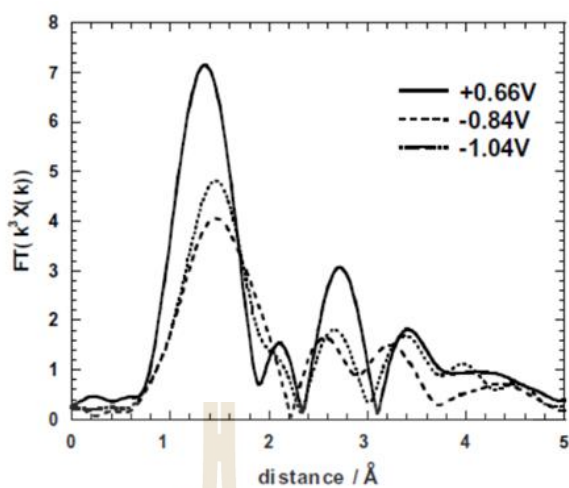
Figure 2.22 FT of the k^3 weighted EXAFS spectra recorded as a function of potential. (Pauporté et al., 2004)

CHAPTER III

EXPERIMENTAL METHODS

3.1   Thin film preparation

3.1.1 Radio frequency (RF) magnetron sputtering technique

RF or Radio Frequency Sputtering is a technique that involves alternating the electrical potential of the current in a vacuum environment at radio frequencies in order to avoid a charge building up on certain types of sputtering target materials, which over time can result in arcing into the plasma, spewing droplets, causing quality control issues on the thin films, and even completely stopping the sputtering of atoms.

DC or direct current sputtering is a cost-efficient method of coating metal targets that are electrical conductors, such as gold. On the other hand, DC sputtering is confined to dielectric target materials-coatings that are non-conducting insulating materials capable of absorbing a polarized charge. Aluminum oxide, Silicon oxide, and Tantalum oxide are all examples of typical dielectric coating materials used in the semiconductor industry.

As with DC Sputtering, RF Sputtering involves passing an energy pulse through an inert gas that gets ionized in a vacuum chamber. These high energy ions strike the target material or cathode that will form the thin film coating, sputtering off atoms as a tiny spray covering the substrate to be coated. RF Magnetron sputtering employs magnets behind the negative cathode to trap electrons above the negatively charged target material, preventing them from bombarding the substrate and so enabling quicker deposition rates.

Positive ions are generated over time and aggregate on the surface of the target face, imparting it with a positive charge. At some point, this charge may accumulate to the point that all sputtering atoms are expelled for coating.

By alternating the electrical potential during RF Sputtering, the target material's surface may be "cleaned" of charge accumulation on a cycle-by-cycle basis. On a

positive cycle, electrons are drawn to the target material or cathode, imparting a negative bias on it. On the negative half of the cycle - which occurs at the radio frequency of 13.56 MHz, which is often used for RF power supply equipment - the ion bombardment of the sputtered target continues. (Hughes, 2016)
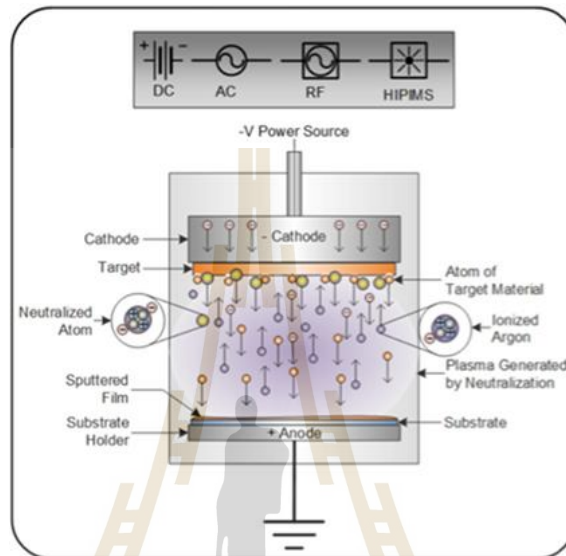
Figure 3.1 Diagram of the RF Sputtering Process. (Hughes, 2016)

However, owing to the AC modulation of the power at radio frequencies, the material to be coated using RF Sputtering does not accumulate as much charge, since it is discharged each half cycle and becomes insulated, finally resulting in the end of thin film deposition. With RF Magnetron Sputtering, the magnetic field creates a boundary "tunnel" that traps electron at the target's surface, increasing gas ion production efficiency and restricting the plasma's discharge. Thus, RF Magnetron Sputtering enables greater current with lower gas pressure, resulting in an increased deposition rate. (Hughes, 2016)

Magnetron sputtering is the process by which the quantity of ions produced increases as the distance between charged particles increases. Due to the Lorentz's force, charge particles are accelerated in a spiral motion as they pass through an angle of magnetic field. Additionally, the magnetic field may confine charged particles that are unable to escape the vicinity (นันทนัส วัฒนสุภิญโญ, 2553).
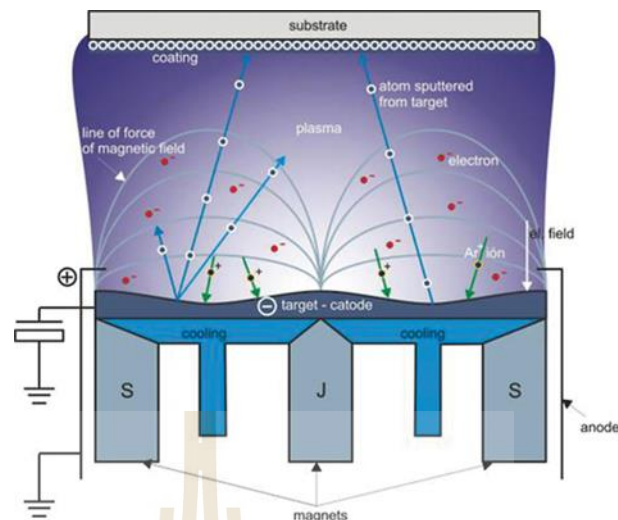
Figure 3.2 Magnetron sputtering system. (นันทนัส วัฒนสุภิญโญ, 2553)

3.1.2 RF Magnetron sputtering setup

In order to prepare the metal oxide thin films, RF magnetron sputtering system locating at SLRI are designed and constructed. First of all, the basic need is trying to make the system as clean, or free of contaminants, as possible for maintaining a good vacuum. The work included the procurement of standard and custom-order components which the team then used in the construction of this system. In the actual construction of the custom-built system, it is necessary to get professional help and supports from multiple people from SLRI.

The works already done in the sputtering system construction are listed below:
- Installed additional turbomolecular and roughing pumps and compact full range gauge (Pfeiffer Vacuum PKR 251).
- Placed sputtering magnetron gun with ceramic target.
- Changed the deposition stage (3 axes of motion and options for sample heating).
- Installed the cooling system for magnetron gun.
- Set and tested RF power supply connected with matching box.
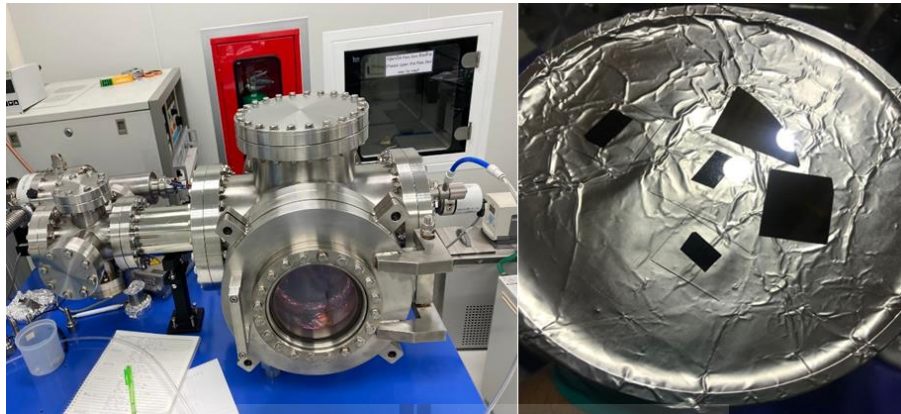
Figure 3.3 (Left) View of entire system (rack and sputter system) and (Right) Substrates holder with carbon tape which hold the substrate.
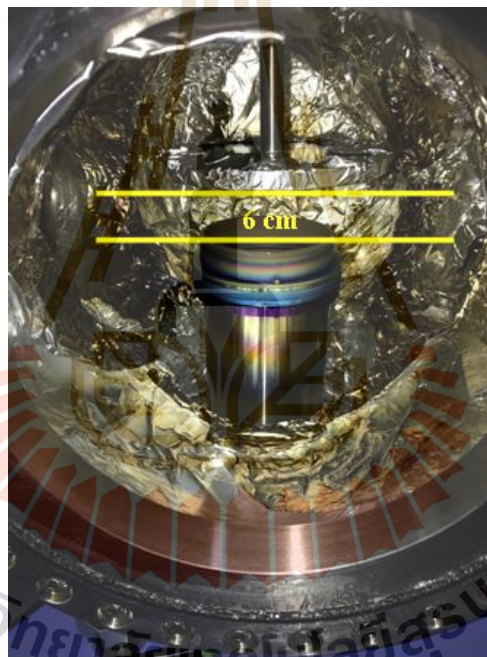
Figure 3.4 A view of the deposition chamber from top, showing plate with substrate holder.

3.1.3 Sample processing

The following steps were followed during the deposition of the vanadium oxide thin films: Cleaning the substrates that will be used for deposition is necessary. This phase is critical because it aids in the formation of a stronger link between the deposited material and the substrate. Ultrasonic cleaning does this. The substrate should be cleaned with alcohol for 30 minutes prior to ultrasonic cleaning. Then reintroduce them to acetone and repeat the procedure for an additional 10 minutes.

Finally, the substrates are reintroduced to the alcohol and cleaned for a further 10 minutes.

The chamber is sealed and the first pump to pump it is a mechanical pump. The fore vacuum should reach a few 9×10^{-3} mbar before the Turbo pump may be activated. Pumping for a few hours should result in a vacuum of 1×10^{-5} mbar, which is satisfactory.

The vanadium oxide thin films were prepared by vanadium metal target (3 inches) 99.9% of purity, from Kurt J. Lesker. The target was placed at a distance of 6 cm from the substrates. It is necessary to enable rare argon gas to flow through the chamber at a rate of 20 sccm, which is regulated by a mass flowmeter, in order to begin the deposition process. It is important to ensure that the ionization gauge is turned off throughout this operation. The RF generator has been switched on, and an argon pressure of 2.6×10^{-2} mbar is required in order to ignite plasma. Then, the O_2 flow rates were varied by 1, 2, 3, 4, 5, and 6 sccm and the RF power and sputtering time was kept constant at 200 W and 80 minutes, respectively while the operating pressure (O_2+Ar gas flow rate) reach in range of 3×10^{-2} mbar. After deposition is complete, the chamber is allowed to cool, the chamber is purged with air, and the substrates are ultimately removed from the substrate holders.

3.2   Thin film characterizations

3.2.1 Scanning electron microscope (SEM)

The scanning electron microscope (SEM) is a sophisticated electron microscope that uses a focused stream of high-energy electrons to create a variety of signals on the surface of solid objects. The signals produced when a focused beam of high-energy electrons interacts with the atoms in a target sample reveal information about the sample's external morphology (texture), chemical composition, crystalline structure and orientation of the materials that comprise the sample, among other things (Brandon and Kaplan, 1999).

A scanning electron microscope is seen schematically in figure 3.5. The SEM generates a stream of incoming electrons in an electron column above the sample

chamber. The electrons are generated by a thermal emission source, such as a heated tungsten filament, or a field emission cathode. The incident electrons' energy may vary between 100 eV and 30 keV, depending on the assessment goals. The SEM column's electromagnetic lenses focus the electrons into a tight beam. By scanning coils at the column's end, the focused beam is guided and positioned onto the sample surface. For imaging, the electron beam is traversed over the surface in a raster pattern. The beam may be focussed on a single point or scanned down a line for x-ray investigation. The beam may be focussed to a diameter of around 10 microns for the probe.

When an electron beam collides with a specimen, a large number of signals are generated. These signals include secondary electrons, backscattered electrons, distinctive x-rays, cathodoluminescence, and transmitted electrons, as depicted in figure 3.6.
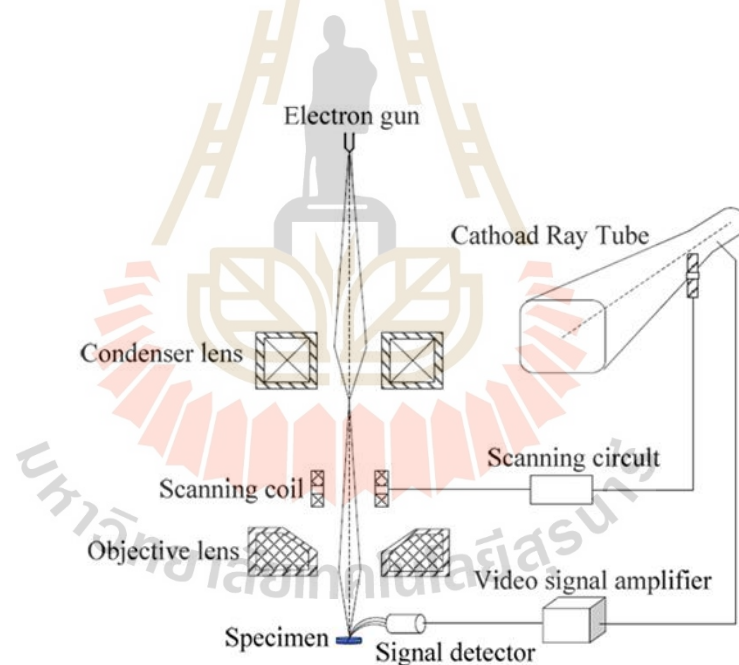
Figure 3.5 Principles schematic illustration of SEM. (JEOL, Ltd., 1989)
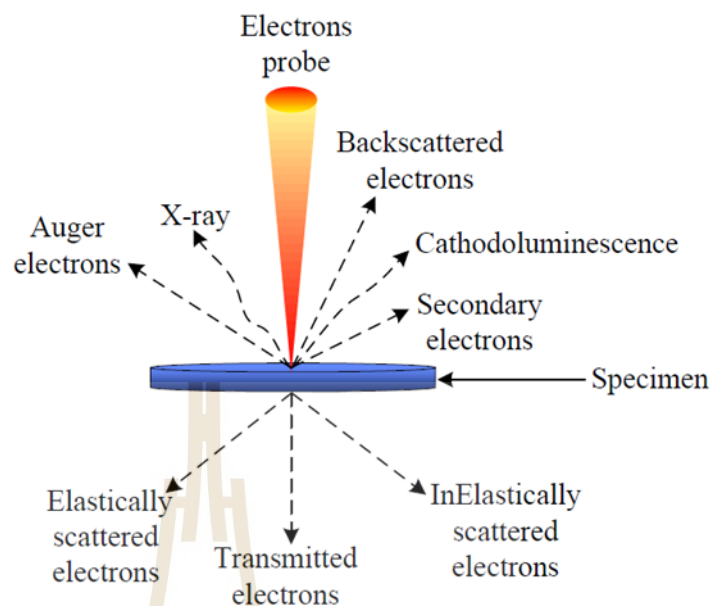
Figure 3.6 Schematic diagram of signals in SEM. (Brandon and Kaplan, 1999)

In SEM, there are four major signals to employ:

1) Secondary electrons (SE) are low-energy electrons that are ejected from sample atoms as a consequence of inelastic collisions with the nucleus that result in considerable energy loss or as a result of the ejection of loosely bound electrons. Secondary electrons have a maximum energy of 50 eV. The topography of the surface features has an effect on the number of electrons that reach the secondary electron detector from any position on the scanned surface. This local shift in electron intensity creates the optical contrast that reveals the surface shape. The secondary electron image resolution of a tungsten-filament electron source SEM is around 3.5 nm for an ideal sample, or 1.5 nm for field emission SE.

2) Backscattered electrons are high-energy electrons that are expelled when an incoming electron collides with the nucleus of a sample atom in an elastic collision. Surface topography is not as precisely resolved as secondary electron imaging because high-energy electrons can escape from far deeper than secondary electrons. Backscattered electron generation efficiency is related to the mean atomic number of the sample material, resulting in picture contrast as a function of composition, with greater atomic number material appearing brighter than lower atomic number material

in a backscattered electron image. Backscattered electron imaging has a resolution of around 5.5 nm.

3) Backscattered electrons are high-energy electrons that are ejected from the nucleus of a sample atom when an incoming electron collides with it in an elastic collision. Because high-energy electrons may escape from far deeper than secondary electrons, surface topography cannot be determined as accurately as secondary electron imaging. The efficiency of backscattered electron generation is proportional to the sample material's mean atomic number, resulting in picture contrast as a function of composition, with material with a higher atomic number appearing brighter than material with a lower atomic number in a backscattered electron image. The resolution of backscattered electron imaging is about 5.5 nm.

4) Cathodoluminescence (CL), the emission of light by excited atoms upon their return to their ground state. CL detectors in the SEM may gather all light released by the specimen or analyze the wavelengths emitted by the specimen and provide a real-color emission spectrum or picture of the cathodoluminescence distribution emitted by the specimen.

To generate a SEM picture, the incident electron beam is scanned over the sample's surface in a raster pattern. An electron detector detects the released electrons at each place in the scanned region. On a cathode ray tube, the strength of the produced electron signal is shown as brightness (CRT). The CRT display shows the morphology of the sample surface area scanned by the incident electron beam by synchronizing the CRT scan to the incident electron beam scan. Magnification of the CRT picture is defined as the ratio of the size of the image display to the area scanned by the electron beam. SEM imaging is primarily performed using two kinds of electron detectors. Secondary electron imaging is performed using detectors of the scintillator type (Everhart-Thornley). A positive voltage is applied to this detector to attract electrons and so increase the signal to noise ratio. Scintillator or solid-state detectors may be used to detect backscattered electrons. The SEM column and sample chamber are vacuumed to enable electrons to easily pass from the electron beam source to the sample and subsequently to the detectors. The chamber is evacuated to a greater vacuum, generally between 10^{-5} and 10^{-7} Torr, for high-resolution imaging. At greater

pressures, imaging of nonconductive, volatile, and vacuum-sensitive materials is possible.

Energy dispersive x-ray spectroscopy (EDS) is a method for detecting and quantifying elemental compositions in a very small sample of material. EDS is a typical feature of scanning electron microscopes. When a SEM image is obtained, the surface being examined is blasted with an electron beam. The EDS system is schematically shown in figure 3.7. Electron bombardment excites atoms, leading in the release of excess energy in the form of X-ray. When the sample surface is blasted with an electron beam, some electrons are extracted from the atoms. As a consequence, electrons from a higher shell must be used to fill holes in the electron shell. As a consequence, an X-ray is created to balance the energy difference between the two electrons. The amount of energy released is proportional to the number of atoms excited, resulting in distinct peaks in the energy spectrum depending on the composition of the material. EDS is a qualitative and quantitative composition diagnostic tool due to the fact that the intensities or areas of the various peaks in a particular spectrum are related to the element's concentration.
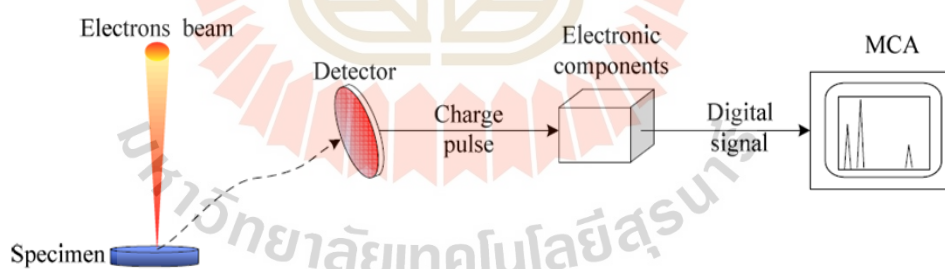
Figure 3.7 Schematic diagram of an EDS. (Brandon and Kaplan, 1999)

3.2.2 Atomic Force Microscopy (AFM)

Atomic force microscopy (AFM) is a method for mapping the topography of materials and studying their characteristics on a nanoscale. AFM interacts with a material through a probe attached to one end of a spring-like cantilever (sample). Attractive or repulsive forces are generated when the sample and the tip contact. These forces provide insight into the sample's topography. When the tip and sample

are in close proximity, the attractive force deflects the cantilever toward the sample; when the tip comes into contact with the sample, the repulsive force deflects the cantilever away from it. Pauli's exclusion principle can account for this phenomenon. Force sensor is provided via the cantilever mechanism. Cantilevers are available in a variety of forms; the one used is determined by the kind of measurement to be performed. To achieve a low force sensitivity, a spring constant k between 0.01-100 N/m is used (Meyer, 1992). The cantilever is vibrated at its resonance frequency in circumstances of vibrations. As shown in Equation (3.1), the resonance frequency is dependent on the force constant and the mass of the cantilever,

$$\omega_0 = \sqrt{\frac{k}{m}} \tag{3.1}$$

This implies that the cantilever's bulk must likewise be kept to a minimum. This is accomplished by shrinking its dimensions. These deflections are detected using a laser beam. This occurs when the incoming laser beam is reflected off the cantilever's surface; any deflection causes the reflected beam's direction to shift. These changes are registered using a high-resolution deflection detector (position sensitive detector). Changes might be significant or insignificant. The detector is sufficiently sensitive to amplify even extremely slight deflections. The feedback loop maintains an instrument-defined setpoint. In this example, feedback regulates the cantilever's deflection. The piezoelectric XYZ-scanner is responsible for the x,y,z-direction motions between the tip and sample. The piezoelectric scanner enables three-dimensional imaging. The schematic diagram of the AFM's operation is given in figure 3.8.
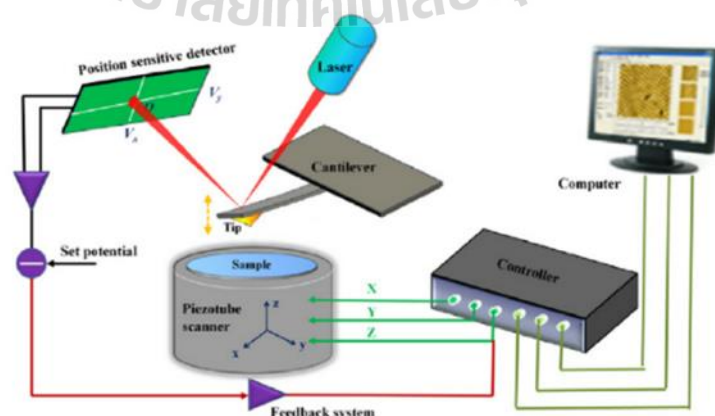
Figure 3.8 A schematic diagram for the working principle of AFM.

A schematic picture illustrating the AFM operating principle, in which the cantilever deflection is caused by the probing tip-sample contact. The illustration is from The AFM functions in two distinct modes: static mode, commonly referred to as contact mode, and dynamic mode (the non-contact mode and the tapping mode). Each mode has a dominating interaction force. In the contact mode, repulsive forces are visible; in the non-contact mode, attracting forces are visible. At high frequencies, we may see both the repulsive and attracting modes in the tapping mode.

3.2.3 X-ray diffraction (XRD)

X-ray diffraction is a non-destructive method that is used to evaluate the phases of the crystal structure, the arrangement of atoms in the molecules of diverse compounds, and the composition of the elements that may be used to determine the crystal structure and crystalline size of a material. Amorphous materials, on the other hand, cannot be quantified using x-ray diffraction since the basic notion of x-ray diffraction concerns x-ray reflection on each crystal plan. As seen in Figure 3.9, Due to the wave form of the x-ray beam, reflection and a route difference equal to the wavelength of the x-ray beam occur. Bragg's law establishes the link between d-spacing, angle of the x-ray beam, and wavelength of the x-ray.

$$d_{hkl} = \frac{n\lambda}{2\sin\theta} \qquad (3.2)$$

where d stands for the distance between consecutive atomic plans, also known as "d-spacing", θ is the x-ray beam's angle, n stands for the diffracted beam's order and the wavelength of the incident x-ray beam is represented by λ.
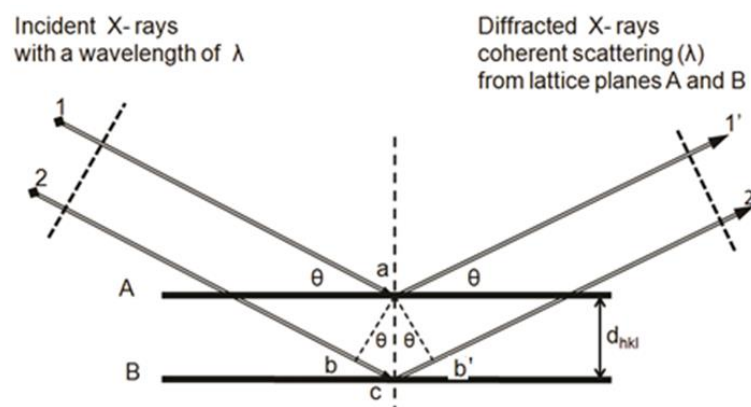
Figure 3.9 The course of the X-ray diffraction beam is controlled by a mechanism.
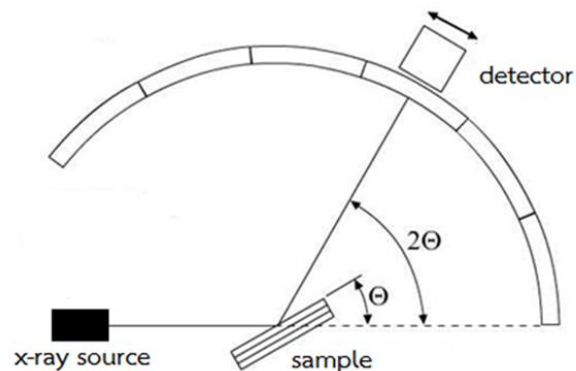
Figure 3.10 Represent XRD measurement of samples.

As illustrated in figure 3.10, this approach rotates the sample material by an angle while moving the X-ray detector by an angle of 2θ to create diffraction in accordance with Bragg's law.

The Bragg requirement is met for any collection of planes with a separation greater than half the wavelength of the x-ray employed (if $d < \lambda/2$, $\sin(\theta) > 1$, which is impossible). This constraint limits the number of diffracted orders that may be achieved from a particular crystal when an x-ray beam of a specific wavelength is used. Due to the fact that the crystal pattern repeats in three dimensions, a three-dimensional diffraction grating is necessary to describe the order of the diffracted waves. Three integers, indicated (h k l), are required to represent the order of the diffracted waves. These three numbers form the Miller indices, which are employed in crystallography to describe the orientation of the reflecting sheets with respect to the unit cell and the path difference in wavelength units between identical reflecting sheets.

The x-ray diffraction technique is carried out using an x-ray diffractometer. An x-ray diffractometer consists of the following critical components (Fultz and Howe, 2008):

    1) A source of x-ray, usually a sealed x-ray tube

    2) A goniometer, which provides precise mechanical motions of the tube specimen and detector

    3) An x-ray detector

4) Electronics for counting detector pulses in synchronization with the positions of the goniometer

The Debye-Scherrer Method, the Laue Method, the Rotating Crystal Method, and the θ-2θ diffractometer Method are four useful approaches for seeing and measuring diffractions. All of this is done to assure compliance with Bragg's legislation. Figures 3.11 and 3.12 illustrate the schematic design of the θ-2θ x-ray diffractometer utilized in this study (Rigaku SmartLab outfitted with a Cu K_ sealed tube with a wave length of 1.5418 Å). The θ-2θ diffractometer is used to measure the diffraction of an unfixed horizontal sample. To do this, the sample will be rotated to θ and the x-ray detector will be relocated to position 2θ. The diffraction angle was calculated using Bragg's equation (3.2). A counterweight is employed to correct for the tube stand's asymmetrical weight distribution. Both the tube stand and the counter weight are secured in the outer ring. XRD data were taken at room temperature in a 2θ range of 10–60° with a step size of 0.02° and a scanning rate of 2.5° per minute.
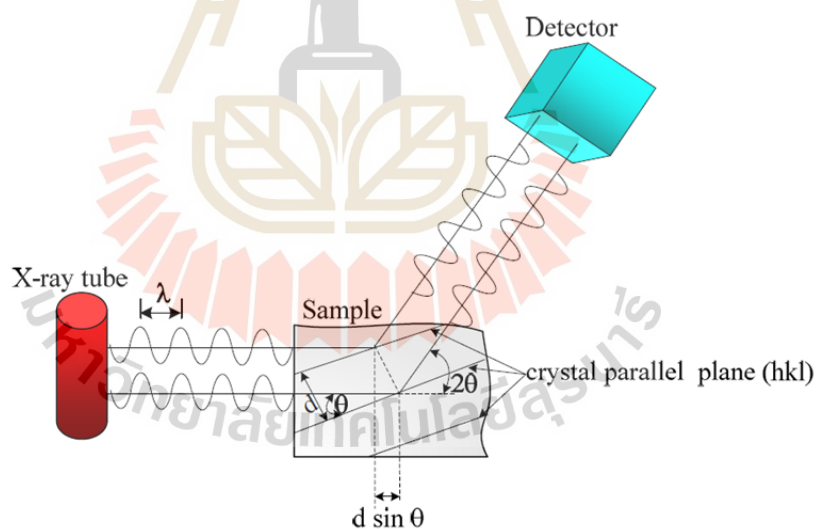
Figure 3.11 X-ray diffraction experiment schematic drawing.
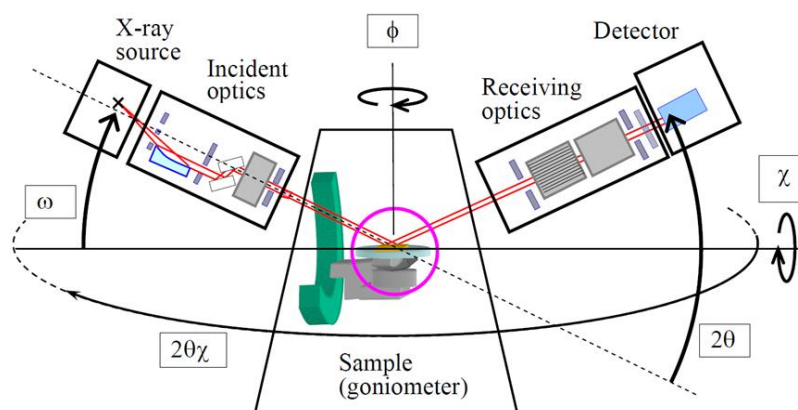
Figure 3.12 Schematic representation of X-ray diffractometer Rigaku SmartLab. (K. Inaba et al., 1994)

3.2.4 UV-Visible spectroscopy (UV-Vis)

UV-Vis spectroscopy is an analytical method that determines the quantity of discrete wavelengths of ultraviolet or visible light absorbed or transmitted by a sample in comparison to a reference or blank sample. This feature is affected by the sample composition and may provide information about the contents and concentration of the sample. Given that this method of spectroscopy is based on the utilization of light, let us first explore the qualities of light.

Light carries a fixed quantity of energy proportionate to its wavelength. Thus, shorter wavelengths of light have a higher energy content, whereas longer wavelengths have a lower energy content. A certain amount of energy is required to promote electrons in a material to a higher energy state, which is visible as absorption. Electrons in a substance's various bonding settings need a varying amount of energy to advance them to a higher energy state. This is why various wavelengths of light are absorbed by different things. Humans can see a visible light spectrum ranging from around 380 nm, which we perceive as violet, to 780 nm, which we perceive as red. UV light has wavelengths that are roughly 100 nanometers shorter than visible light. Thus, light may be defined by its wavelength, which is advantageous in UV-Vis spectroscopy for analyzing or identifying various compounds by discovering the exact wavelengths associated with highest absorption (see the Applications of UV-Vis spectroscopy section).

Whilst there are several versions of the UV-Vis spectrophotometer, in order to acquire a better grasp of how it works, let's analyze the primary components represented in figure 3.13.
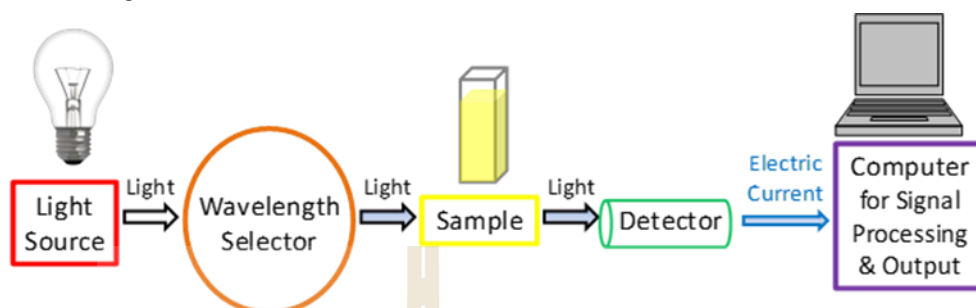
Figure 3.13 A simplified schematic of the main components in a UV-Vis spectrophotometer. (Justin, 2021)

3.2.4.1 Light source

As a light-based approach, it is critical to have a stable source capable of emitting light throughout a broad range of wavelengths. A single xenon lamp is often employed as a high-intensity light source in both the ultraviolet and visible wavelength regions. However, xenon lights are more expensive and less stable than tungsten and halogen lamps.

In devices with two lamps, a tungsten or halogen lamp is often used to provide visible light, while a deuterium lamp is frequently used to generate UV light. Due to the fact that two distinct light sources are required to scan both UV and visible wavelengths, the instrument's light source must swap during measurement. In reality, this switchover often happens between 300 and 350 nm, when the light output from both light sources is comparable, allowing for a more seamless transition.

3.2.4.2 Wavelength selection

Following that, among the large range of wavelengths produced by the light source, certain wavelengths relevant to the sample type and analyte for detection must be chosen for sample evaluation. Several techniques are available to do this, including the following:

3.2.4.2.1 Monochromators

A monochromator divides light into a small number of wavelengths. It is often based on diffraction gratings that may be manipulated to determine the

appropriate incoming and reflected angles (Diffey, 2002). The groove frequency of a diffraction grating is often expressed as the number of grooves per millimeter. A greater groove frequency results in increased optical resolution at the expense of a smaller useable wavelength range. A lower groove frequency results in a wider range of useful wavelengths but a lesser optical resolution. Between 300 and 2000 grooves per millimeter are suitable for UV-Vis spectroscopy, however a minimum of 1200 grooves per millimeter is usual. The quality of the spectroscopic measurements is highly dependent on the diffraction grating and optical setup's physical defects. As a result, ruled holographic diffraction gratings have a higher defect rate than blazed holographic diffraction gratings (Namioka, 2000). Generally, holographic diffraction gratings with a blazed surface provide substantially higher-quality observations (Namioka, 2000).

3.2.4.2.2 Absorption filters

Absorption filters are often constructed of tinted glass or plastic with the purpose of absorbing certain wavelengths of light (Diffey, 2002).

3.2.4.2.3 Interference filters

Also known as dichroic filters, these widely used filters are constructed of several layers of dielectric material that exhibit interference between the thin layers of material. By using destructive interference, these filters may be utilized to exclude undesired wavelengths, thereby serving as a wavelength selector (Diffey, 2002).

3.2.4.2.4 Cutoff filters

Cutoff filters enable light to pass through at a wavelength either below (shortpass) or above (longpass). These are often achieved via the use of interference filters.

3.2.4.2.5 Bandpass filters

Bandpass filters permit the passage of a variety of wavelengths and may be created by combining shortpass and longpass filters.

Due to its flexibility, monochromators are the most often utilized for this operation. Filters, on the other hand, are often used in conjunction with monochromators to further reduce the wavelengths of light picked for more exact measurements and to increase the signal-to-noise ratio.

3.2.4.3 Detection

After the light has gone through the sample, it is converted to a readable electrical signal using a detector. Detectors are often made of photoelectric coatings or semiconductors.

3.2.4.3.1 Photoelectric Coating

When exposed to light, a photoelectric coating emits negatively charged electrons. A current proportionate to the light intensity is created when electrons are expelled. A photomultiplier tube (PMT) is one of the most often utilized detectors in UV-Vis spectroscopy (Abramowitz and Davidson, 2021). (Namioka, 2000; Picollo et al., 2018). A photomultiplier tube is based on the photoelectric effect, which causes electrons to be released upon exposure to light. The ejected electrons are then sequentially multiplied to create a greater electric current (Abramowitz and Davidson, 2021). PMT detectors are very helpful for detecting extremely low light levels.

3.2.4.3.2 semiconductors

When semiconductors are exposed to light, they permit the passage of an electric current proportional to the light intensity. More precisely, photodiodes6 and charge-coupled devices (CCDs) are two of the most prevalent semiconductor detectors (Amelio, 1974; Namioka, 2000; Picollo et al., 2018).

After the detector generates an electric current, the signal is identified and sent to a computer or screen. The figures 3.14 and 3.15 provide simplified schematic schematics of UV-Vis spectrophotometer configurations.
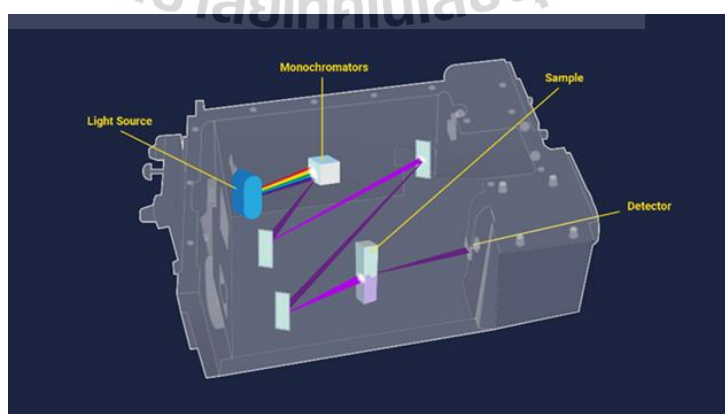
Figure 3.14 Schematic diagram of a cuvette-based UV-Vis spectroscopy system. (Justin, 2021)
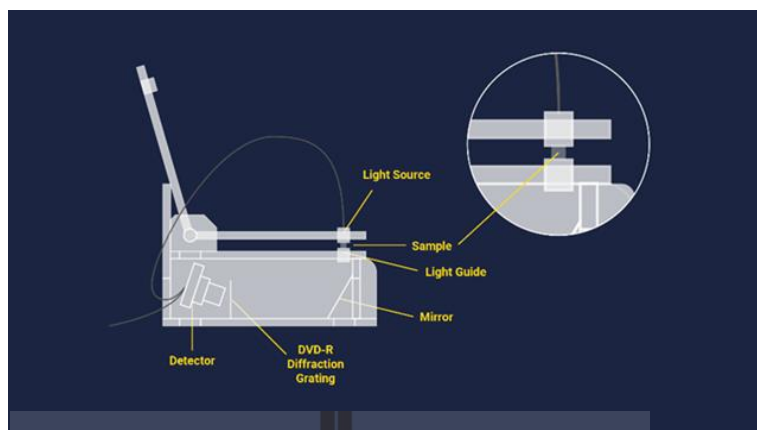
Figure 3.15 Schematic diagram of a cuvette-free UV-Vis spectroscopy system. (Justin, 2021)

UV-Vis spectroscopy data may be shown as a function of wavelength as an absorbance, optical density, or transmittance graph. However, the data is often displayed in the form of a graph with absorbance on the vertical y axis and wavelength on the horizontal x axis. Typically, this graph is referred to as an absorption spectrum; an example of one is given in figure 3.16.
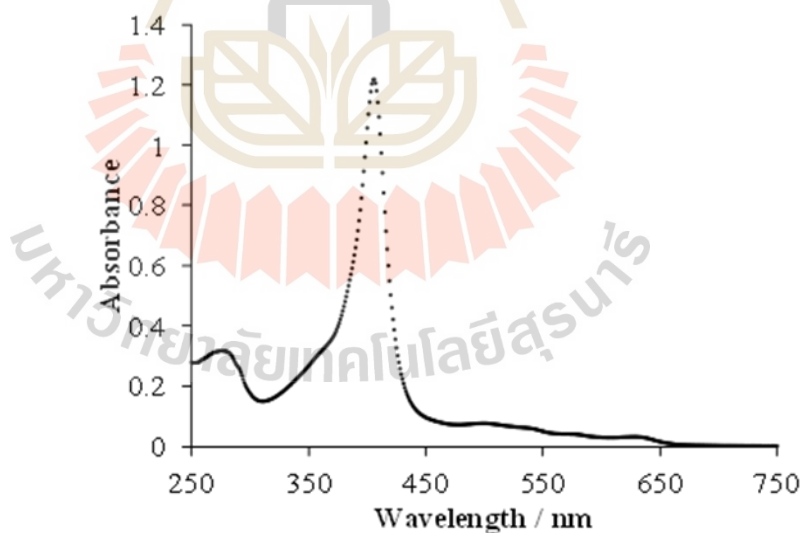
Figure 3.16 An example absorption spectrum taken from a UV-Vis spectrophotometer. (Justin, 2021)

The intensity of light may be fairly predicted to be quantitatively connected to the quantity of light absorbed by the sample, based on the UV-Vis spectrophotometer apparatus discussed in the preceding portion of this article.

The absorbance (A) is equal to the logarithm of a proportion of the intensity of light before it passes through a sample (I_0) divided by the intensity of light after it passes through the sample (I). The ratio of I to I_0 is sometimes referred to as transmittance (T), because it indicates how much light has travelled through a sample. However, given the molar absorptivity (ε) and path length (L) of the sample are known, Beer–Lambert's law is often used to determine the concentration of the sample (c). Typically, ε is stated in terms of L mol^{-1} cm^{-1}, L in terms of cm, and c in terms of mol L^{-1}. As a result, A lacks units.

Sometimes AU is used to indicate arbitrary units or absorbance units but this has been strongly discouraged.

Beer–Lambert's law is particularly effective for determining the concentration of a drug when a linear connection exists between the concentration of the substance and the concentration of a measured set of standard solutions containing the same substance. Equation 3.3 illustrates the mathematical links between absorbance, Beer–Lambert's law, the observed light intensities, and transmittance.

$$A = \varepsilon Lc = \log_{10}\left(\frac{I_0}{I}\right) = \log_{10}\left(\frac{1}{T}\right) = -\log_{10}(T) \qquad (3.3)$$

Equation 3.3: A set of equations showing the relationships between absorbance A, Beer–Lambert's law, the light intensities measured in the instrument, and transmittance.
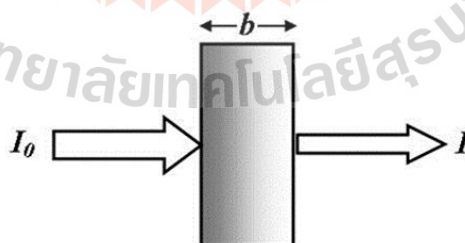
Figure 3.17 Light before passing through the sample (I_0) divided by the intensity of light after passing through the sample (I).

3.2.5 X-ray absorption spectroscopy (XAS)

X-ray absorption Spectroscopy is an extremely powerful instrument for identifying the local structure, formal oxidation state, and surrounding atoms of an

element, as well as the electronic structure of materials. XAS experiments are often conducted in a synchrotron radiation facility, where the energy of x-ray photons may be altered and controlled (Shanthakumar, 2008). Additionally, the synchrotron radiation facility incorporates high-intensity light sources.

The Lambert-Beer law describes the absorption equation, which indicates that the intensity of the beam diminishes exponentially with the strength of the incoming x-ray beam.

$$I = I_0 e^{-\mu x} \tag{3.4}$$

where I_0 is the entering x-ray beam's intensity, I is the beam's intensity after passing through the sample, x is the sample's thickness, μ is the absorption coefficient and the absorption was determined by μx.

$$\ln\left(\frac{I_0}{I}\right) = \mu x \tag{3.5}$$

The absorption cross-section σ_a and the linear absorption coefficient are related by

$$\mu = \sigma_a \rho_a = \frac{\sigma_a \rho_m N_A}{A} \tag{3.6}$$

where A, ρ_a, ρ_m and N_A are the atomic mass number, the atomic density, the mass density and Avogadro's number, respectively.

The energy of the photon has a significant effect on the absorption cross section. Platinum is seen in figure 3.18. The double-logarithmic illustration demonstrates that the absorption cross section is approximately proportional to $1/E^3$ below and above discontinuities.
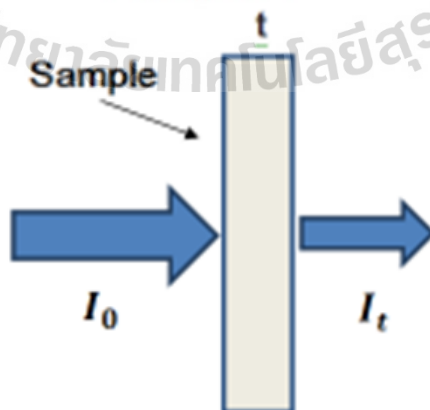
Figure 3.18 In transmission mode, a schematic of x-ray absorption measurement is shown.
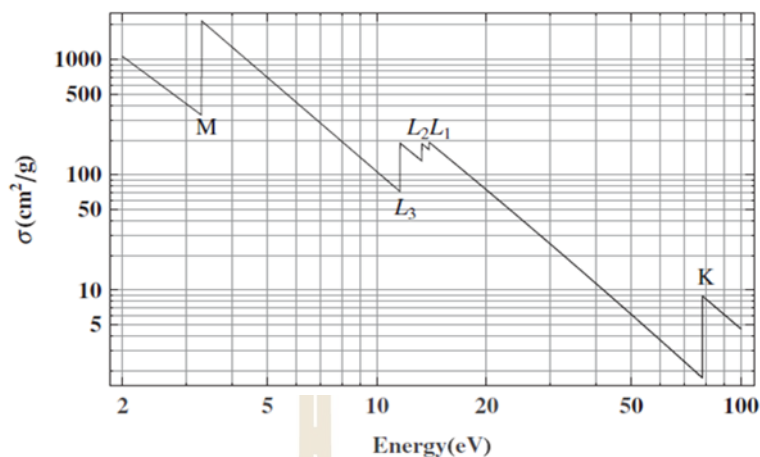
Figure 3.19 Log-log plot of the (semiempirical) X-ray absorption cross section of platinum (Z=78) vs. X-ray energy. The K, L_1, L_2, L_3, and M edges are shown; fine structure is not shown. (Bunker, 2010)

The latter, dubbed absorption edges, occur at certain energies when the X-ray is strong enough to evict an electron from an atomic core level, resulting in an abrupt increase in the absorption cross section.

In this case, the selection criteria are applied to the electrons' transition. Transitions between the electronic energy levels of transition metal complexes are governed by Selection Rules.

1. $\Delta S = 0$; The Spin Rule, the electron's spin must be unchanged from core shell state to excited state.

2. $\Delta l = \pm 1$; The Orbital Rule, the difference of electron's orbital angular momentum must be equal -1 or 1 only.

The total angular momentum was defined as $J = l+S$ or have value $|l-s| \geq J \geq l+s$, where $l=0,1, 2, ..., n-1$ and $S = -1/2, 1/2$. Therefore, the spin rule can be considered by $\Delta J = \pm 1$. In addition, the new symbol for electron each shell were defined for the electron transition. Figure 3.20 shows the electron transition in inner shell.

When X-ray radiation is incident via the binding energy of a core shell, the absorption cross-section rapidly increases. This spectral region is referred to as the absorption edge, with each edge denoting a distinct core-electron binding energy. The names of the edges are denoted by the fundamental quantum number: K for n = 1, L for n = 2, M for n = 3, and so on.
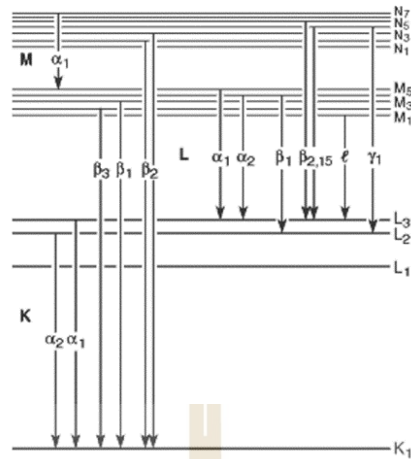
Figure 3.20 Diagram of the electron transition in inner shells. (Thompson et al., 2001)

The x-ray apsorption process involves the absorption of photon energy by an atom, which has an effect on the electrons in the inner shells: K, L, or M, which transition to an unoccupied valance band above the Fermi level. When an electron is stimulated, its energy state becomes unstable. As a result, an electron in the next state will transition to replace the exicited electron, resulting in fluorescence emission, as seen in figure 3.21. Although the core energy state is stable, the subsequent state is not. As a result, another electron in the next state will transit to the conduction band; this electron is referred to as the Auger electron.
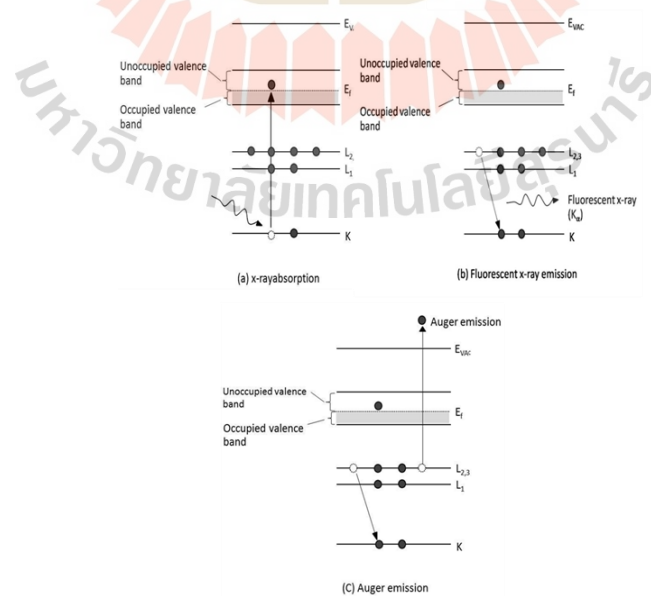
Figure 3.21 Mechanism of the x-ray absorption (a) X-ray absorption (b) Fluorescent X-ray emission and (c) Auger emission. (Klysubun, 2006)

X-ray absorption spectroscopy (XAS), alternatively referred to as X-ray absorption fine structure (XAFS), is an absorption spectroscopy technique that involves a modulation of the absorption coefficient as a function of the incident photon, typically by a few present, around and above the absorption edge. This fine structure is a material's distinctive hallmark since it is dependent on the material's detailed local and electronic structures. For example, Fe K-edge refers to the transition of an excited electron from the 1s to the 3d orbital, which is disallowed by the selection rule. However, in the case of FeO, the action of Fe-O bonding affects d-orbital spitting as t_{2g} and e_g, which results in the mixing of d-p orbitals according to ligand field theory. As a result, a prohibited transition is partly permitted as a result of ligand p-character mixing. While the first line on the main edge is owing to the permitted 1s to 4p bound-state transition. The post edge is associated with the unoccupied state in the conduction band and the complete multiple scattering of a spherical wave electron by its adjacent atom. As seen in figure 3.22, XAS is further classified into two types: X-ray Absorption Near Edge Structure (XANES), which finishes roughly 80–100 eV above the edge, and Extended X-ray Absorption Fine Structure (EXAFS), which starts approximately 50 eV above the edge.
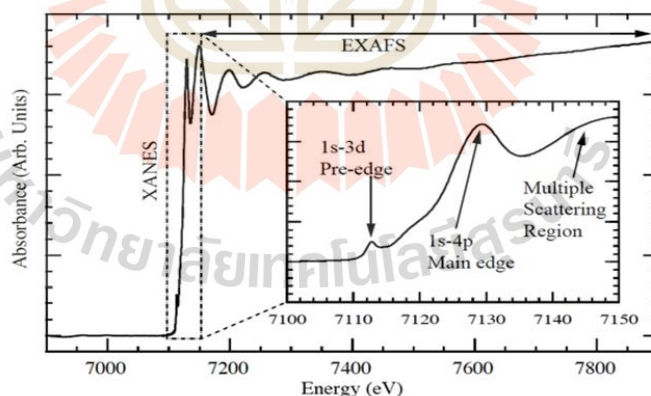
Figure 3.22 The absorbance Fe K-edge spectra in compound iron oxide. (Larsen et al., 2014).

3.2.5.1 X-ray Absorption Near Edge Structure (XANES)

The XANES region (including the pre-edge region) contains information on the local geometry of the absorbing atom. Additionally, the edge location indicates the charge (oxidation state) of the absorber. The XANES is usually only qualitatively

interpretable because to the overlapping contributions of several electrical and structural processes and the approximations required for its theoretical explanation.

The overall absorption cross-section can be estimated using Fermi's Golden Rule (Gaussian unit) of one electron approximation (Koningsberger and Prins, 1988; Kodre, 2002; Stern et al., 1983; Als-Nielsen and McMorrow, 2001; Newville, 2004; Ravel, 1997; Shanthakumar, 2008),

$$\mu(\omega) = \frac{4c\pi^2 e^2}{\omega} \sum_{i,f} \left| \left\langle f \left| \vec{r} \cdot \hat{\varepsilon} e^{i\vec{k}\cdot\vec{r}} \right| i \right\rangle \right|^2 \delta(E_i - E_f + \hbar\omega) \qquad (3.7)$$

where $|i\rangle$, $|f\rangle$, E_i and E_f denote the initial and final states and their energies; k is wave vector, $\hat{\varepsilon}$ is unit polarization, ω is frequency of photon energy, c is light velocity, e is electron charge and $\delta(E_i)$ is the Dirac delta function. Generally, this equation can be written in form the Dipole operator (D) as

$$\mu(\omega) = \frac{4c\pi^2 e^2}{\omega} \sum_{i,f} \left| \left\langle f \left| \vec{D} \right| i \right\rangle \right|^2 \delta(E_i - E_f + \hbar\omega) \qquad (3.8)$$

which can easily understand for electron transition from $|i\rangle$, to next $|f\rangle$ state corresponding to the photon energy incident in the Dirac delta function and amplitude relate dipole transition in inner atom. However, when an electron is stimulated by a photon with a higher energy than the binding energy, the electron will transit to the unoccupied valance band. At this point, the photon energy is higher, and the photon will leave the inner atom, propagating a spherical electron wave.

In this case, we use the muffin-tin approximation to determine the spherical electron wave scattering. We examine scattering from the muffin-tin potential, which consists of many atoms or ions, each of which contributes non-zero energy only within a finite-radius spherically non-overlapping scattering zone.

$$V = \sum_i v^i \qquad (3.9)$$
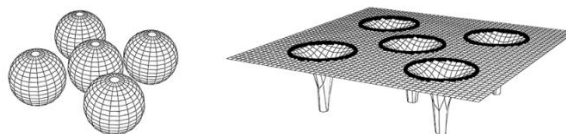
Figure 3.23 The muffin-tin potential consists of non-overlapping spherical regions. (Kodre, 2002)

Figure 3.23 shows the muffin-tin potential, which is set to zero outside the spherical or interstitial portions. The scattering parameters, which include the amplitude and phase changes of the scattering, are computed independently for each scatterer and are therefore pure atomic quantities. The Hamiltonian describes the propagation of a spherical electron wave in such a muffin-tin potential V.

$$H = H_0 + V \tag{3.10}$$

where H_0 is the kinetic-energy operator. According to Schrodinger's equation is

$$H|\varphi\rangle = E|\varphi\rangle \tag{3.11}$$

$$(E - H_0)|\varphi\rangle = V|\varphi\rangle \tag{3.12}$$

However, we cannot solve to exact solution. Therefore, we can consider to separated terms. The term of $(E - H_0)|\varphi\rangle$ is free-electron wave function and if $\langle\vec{r}|\emptyset\rangle$ is the solution of the "homogeneous" part of free-electron wave function.

$$(E - H_0)\langle\vec{r}|\emptyset\rangle = 0 \tag{3.13}$$

And the free-electron Green's function G_0 is defined with relation

$$(E - H_0)G_0(\vec{r},\vec{r}';E) \equiv (\nabla^2 + k^2)G_0(\vec{r},\vec{r}';E) = \delta(\vec{r} - \vec{r}') \tag{3.14}$$

Therefore, the general solution of Eq. 3.13 can be written as a sum of the solution of the "homogeneous" part and the Green's function for the muffin-tin potential part

$$\langle\vec{r}|\varphi\rangle = \langle\vec{r}|\emptyset\rangle + \int d^3 r' \, G_0(\vec{r},\vec{r}';E)\langle\vec{r}|V\varphi\rangle \tag{3.15}$$

It is easily understood, if the spherical electron wave is only weakly scattered by the potential V, the solution $\langle\vec{r}|\varphi\rangle$ is close to the free-electron solution $\langle\vec{r}|\emptyset\rangle$. Generally, the Green's function can be written in form

$$G_0^{\pm}(\vec{r},\vec{r}';E) = \langle\vec{r}|G_0^{\pm}|\vec{r}'\rangle = -\frac{1}{4\pi}\frac{e^{\pm ik|\vec{r}-\vec{r}'|}}{|\vec{r}-\vec{r}'|} = \left\langle\vec{r}\left|\frac{1}{E-H_0\pm i\eta}\right|\vec{r}'\right\rangle \tag{3.16}$$

Because of its singularity, an imaginary term is modified in the operator $\frac{1}{E-H_0}$ by $\pm i\eta$, where η is infinitesimally small for identify direction of spherical wave electron, G_0^+ and

G_0^- describe how outing and coming spherical waves propagate in free space, respectively. Therefore, the formal solution of the operator Eq. 3.15 is given by the Lippman-Schwinger equation

$$\langle \vec{r}|\varphi \rangle = \langle \vec{r}|\emptyset \rangle + \frac{1}{E - H_0 \pm i\eta} V|\varphi \rangle \tag{3.17}$$

To solve Eq. 3.15, one needs to define transition operator (T) are

$$V|\varphi \rangle = T|\varphi \rangle \tag{3.18}$$

If we define the propagation G of this system as

$$G(E) = \frac{1}{E - H_0 - V + i\eta} = ([G_0]^{-1} - V)^{-1} = G_0(1 - VG_0)^{-1} \tag{3.19}$$

According to the Taylor series expression

$$G(E) = G_0 + G_0 V G_0 + G_0 V G_0 V G_0 + \ldots = G_0 + G_0 V G \tag{3.20}$$

The following important relationships from Eq. 3.18,

$$G_0 T = GV \tag{3.21}$$

And then,

$$G = G_0 + G_0 T G_0 \;;\; T = V + VGV \tag{3.22}$$

according to the muffin-tin potentials from Eq. 3.9, we can write the transition operators of individual atoms as

$$t^i = v^i + t^i v^i G_0 \tag{3.23}$$

However, the operator T and t^i is not obvious in the physical meaning, but we are able to explain in the weak-scattering expansions by substituting Eq. 3.22 into 3.23 respectively, we obtain

$$G = G_0 + \sum_i G_0 v^i G_0 + \sum_{i, i1} G_0 v^i G_0 v^i G_0 + \ldots$$
$$= G_0 + \sum_i G_0 t^i G_0 + \sum_i \sum_{i1 \neq i} G_0 t^i G_0 t^i G_0 + \ldots \tag{3.24}$$

$$T = \sum_i t^i + \sum_i \sum_{i1 \neq i} t^{i1} G_0 t^i + \sum_i \sum_{i1 \neq i} \sum_{i2 \neq i} t^{i2} G_0 t^{i1} G_0 t^i + \ldots \tag{3.25}$$

$$t^i = v^i + v^i G_0 v^i + v^i G_0 v^i + v^i G_0 v^i G_0 v^i + \ldots \tag{3.26}$$

equations are referred to as Dyson's expansions, and Eq. (3.24) may be used to describe the order of the spherical electron wave's scattering process. The first term denotes the propagation of an unscattered wave. The second term is single scattering through free propagation G_0 to the ith atom, where the wave is scattered once by potential v^i and then continues ahead, as seen in figure 3.24(a)-left. Due to the similarity, the third word "scatter" is used to refer to the incident wave twice, as seen in figure 3.24(a)-middle and right.
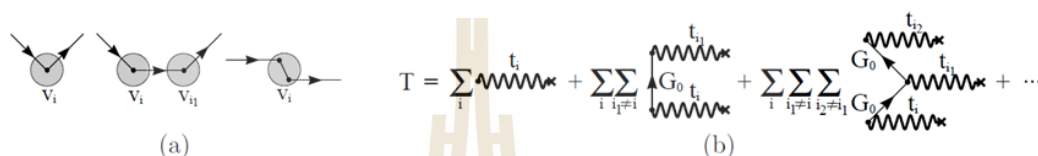
Figure 3.24 (a) Single scattering (left), double scattering from different atoms (middle), and double scattering from the same atom (right). (b) Graphical representation of the T-operator. (Kodre, 2002).

3.2.5.2 Extended X-ray Absorption Fine Structure (EXAFS)

The EXAFS is a term that refers to the oscillatory region of the x-ray absorption spectrum that begins roughly 80 eV above the absorption edge and extends to nearly 1,000 eV. Above the absorption edge, the energy of the X-ray photon is used to excite an electron into the continuum, and any residual energy is converted to kinetic energy by the photoelectron. Photoelectron waves can be thought of as spherical waves propagating from absorber atoms. If additional atoms are nearby the absorber atoms, the photoelectron is dispersed by them and subsequently returns to the absorber atoms, contributing to the EXAFS signal (Groot et al., 1994; Hench and West, 1990). As seen in figure 3.25, the arriving and dispersed waves may interact. Each atom located at the same radial distance from the absorber contributes to the same EXAFS signal component. This collection of atoms is referred to as a shell. The distance between the absorber and the backscattered atom has an effect on the phase of the EXAFS signal, which varies according to the photoelectron's wavelength. The kind of atom that backscatters dictates the relationship between backscattering strength and photoelectron energy. As a consequence, EXAFS gives information about the center atom's atomic surroundings. Above a specific absorption edge, the oscillatory

component of the x-ray absorption spectrum is investigated using the EXAFS technique. As a result, an experimental EXAFS function may be defined as follows:

$$\chi(E) = [\mu(E) - \mu_0(E)]/\Delta\mu_0 (E) \tag{3.27}$$
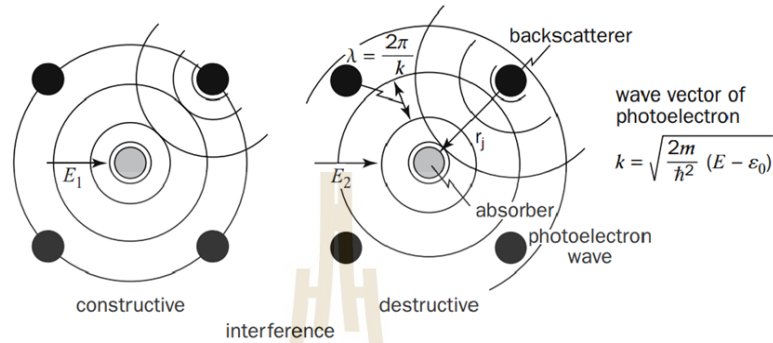
Figure 3.25 Interference of outgoing and backscattered photoelectron wave responsible for XAFS oscillation. $E = \hbar\omega$ is the incoming photon energy. (Hippert et al., 2006)

where μ_0 is the background absorption coefficient, $\Delta\mu_0 (E)$ is the absorptionedge jump, and k is the photoelectron wave number, given by $k = \sqrt{2m_e(E - E_0)/\hbar^2}$ with m_e is the electron mass and E_0 is the edge energy. After that, χ(k) is obtained from the measured absorption coefficient $\mu(E)$. Also, the E_0 is the energy at the first maximum of the derivative of $\mu(E)$ at the Ti K-edge (Bunker, 2010). According to Fermi-Golden rule Eq.3.7, the final state will be affected by the neighboring atom because the photo-electron will be able to see it. If we separate $|f\rangle$ into two state, one that is the "bare atom" portion ($/f_0\rangle$), and one that is the effect of the neighboring atom ($|\Delta f\rangle$) as

$$|f\rangle = |f_0\rangle + |\Delta f\rangle \tag{3.28}$$

Therefore

$$\mu(E) \, \alpha \, |i\langle\hat{\varepsilon}\rangle f_0|^2 [1 + \langle i\langle\hat{\varepsilon}\rangle\Delta f\rangle \frac{\langle f\langle\hat{\varepsilon}i\rangle\rangle^*}{|i\langle\hat{\varepsilon}\rangle\Delta f|^2} + C. C] \tag{3.29}$$

where C.C. means complex conjugate. Comparison Eq. 3.28 and 3.29, we can now assign $\mu(E_0) = |i\langle\hat{\varepsilon}\rangle f_0|^2$ as the "bare atom absorption", which depends on the absorbing atom only. Therefore, the signal of EXAFS will be proportion as

$$\chi(E) \, \alpha \, \langle i\langle\hat{\varepsilon}\rangle\Delta f\rangle \tag{3.30}$$

We can consider (at least roughly) an integral equation easily (at least roughly). The interaction term H is probably the most complicate part, which represents the process of changing between two energy, momentum states. In quantum radiation theory, the interaction term needed is the p·A term, where A is the quantized vector potential (the A·A term, but this does not contribute to absorption). Therefore, it can be reduced to a term that is proportional to $e^{-i\vec{k}\cdot\vec{r}}$. The initial state is a tightly bound core-level, which we can be approximated by delta function. Finally, the change in final state is the wave-function of the scattered photo-electron, $\varphi_{scatt}(r)$.

$$\chi(E) \, \alpha \, \int dr \delta(r) e^{ikr} \varphi_{scatt}(r) \tag{3.31}$$

However, r=0

$$\chi(E) \, \alpha \, \varphi_{scatt}(0) \tag{3.32}$$

The wave-function of the scattered photo-electron can consider from the spherical wave electron move out from absorber atoms and expression as

$$\varphi_{backscatt}(k,r) = (f_i^{eff}(k)e^{ik|R_i-r|}e^{i(\delta_i(k)-\frac{\pi}{2})})(|R_i - r|)^{-1} \tag{3.33}$$

where $f_i^{eff}(k)$ is the scattering amplitude and the term $\delta_i(k) - \frac{\pi}{2}$ is phase shift of photoelectron after scattering from neighbor atoms. Therefore, the total photoelectron wave scattering obtains by

$$\varphi_{scatt}(k,r) = \varphi_0(k,r) \cdot \varphi_{backscatt}(k,r)$$
$$= f_i^{eff}(k)e^{2ik|R_i-r|+(\delta_i(k)-\frac{\pi}{2}} \cdot (|R_i - r|)^{-2} \tag{3.34}$$

The scattering at absorber atom r = 0, the real part of Eq. 3.34 is

$$\varphi_{scatt}(k,r) = f_i^{eff}(k)\sin[skR + \delta_i(k)]R^{-2} \tag{3.35}$$

However, we neglect the effect of the thermal and static disorder in the bond distances will give a range of distances that will affect the XAFS is $e^{-2k^2\sigma^2}$, where is the Debye-Waller (DW) factor which is caused by thermal vibration in subject of the heat capacity, is written as

$$\sigma_i^2(T) = \frac{\hbar^2}{2k_B M_R \theta_E} \coth\left(\frac{\theta_E}{2T}\right) \tag{3.36}$$

Where k_B is the Boltzmann constant, is reduce mass of scattering atoms and is the Einstein's temperature.

Moreover, we still neglect the effect of the lifetime of excited photoelectron and core hole. Because in order for backscattering wave to interfere with outgoing wave the two must be coherent as

$$e^{\frac{-R_i}{\lambda(k)}} \tag{3.37}$$

However, real systems usually have more than one type of neighboring atom around a particular absorbing atom. This is easily accommodated in the XAFS formalism, as the measured XAFS will simply be a sum of the contributions from each scattering atom type (or coordination shell, as it is often called the terms coordination sphere and scattering path are also used), In general $\chi(k)$, can be expressed by summation of all path, EXAFS equation is

$$\chi(k) = \sum_f \frac{S_0^2 N_j}{k R_j^2} \left| f_j^{eff}(k, R_j) \right| \sin\left[2kR_j + \varphi_j(k)\right] e^{-2\sigma_j^2 k^2} e^{-R_j/\lambda(k)} \tag{3.38}$$

where Nj is the degeneracy of path j. Note that Eq. (3.17) includes both single scattering (SS) and multiple scattering (MS) processes. For a SS path, Nj is simply the number of chemically identical atoms situated at a given distance Rj from the central atom. However, $\chi(k)$ can be a Fourier transform (FT) in R-space and expressed by

$$\chi(R) = \frac{\int_0^\infty k^2 \chi(k) w(k) e^{2ikR} dk}{2\pi} \tag{3.39}$$

To process and enhance the EXAFS with the high k region, the plot $k^2 \chi(k)$ is considered and windowed using a Hanning window w(k).

3.2.5.3 X-ray absorption spectroscopy setup

Due to the high intensity and energy-varying capability of generated x-ray photons, as well as the ability to capture a continuous absorption spectrum over a broad energy range, x-ray absorption spectroscopy is often done at a synchrotron radiation source. There are three methods of x-ray absorption measurements, as

schematically depicted in figure 3.26: transmission-mode XAS, fluorescence-mode XAS, and electron-yield XAS.

(a) I_0 I_1

Incident x-ray photon beam
transmitted x-ray photon beam

$I = I_0 e^{-\mu(E)x}$

(b) I_0

Incident x-ray photon beam
Fluorescence X-ray
X-ray detector

(c)

A

e^-

I

$I_{f,e} = \mu I_0$

I_0

Incident x-ray photon beam
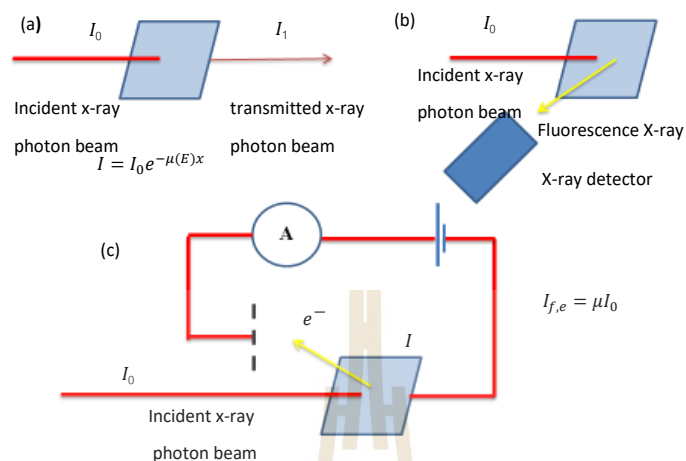
Figure 3.26 Transmission mode, fluorescence mode, and electron yield are the three modalities of XAS measurement [adapted from. (Kawai, 2000)

In transmission mode XAS, the intensities of the incident x-ray photon beam (I_0) and transmitted x-ray photon beam (I) are measured using ionization chambers after the energy of the incoming x-ray photons is modulated using an x-ray double crystals monochromator, as indicated in figure 3.27. In this mode, we ensure that the x-ray photon beam is precisely positioned on the sample. The experimental configuration of the XAS experimental station at the XAS beam line, Siam Photon Laboratory, SLRI is shown in figure 3.28.

Double crystal monochromator

X - ray

Ionization chamber

Ionization chamber

Sample chamber
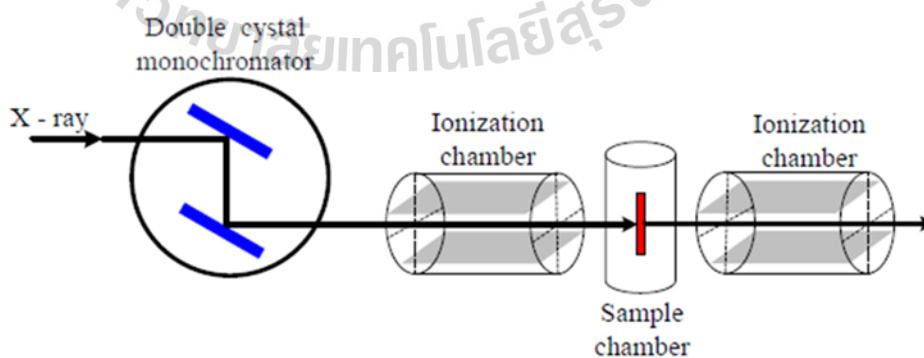
Figure 3.27 Schematic illustration of the experimental setup of transmission-mode X-ray absorption spectroscopy. (Jutimoosik, 2010)
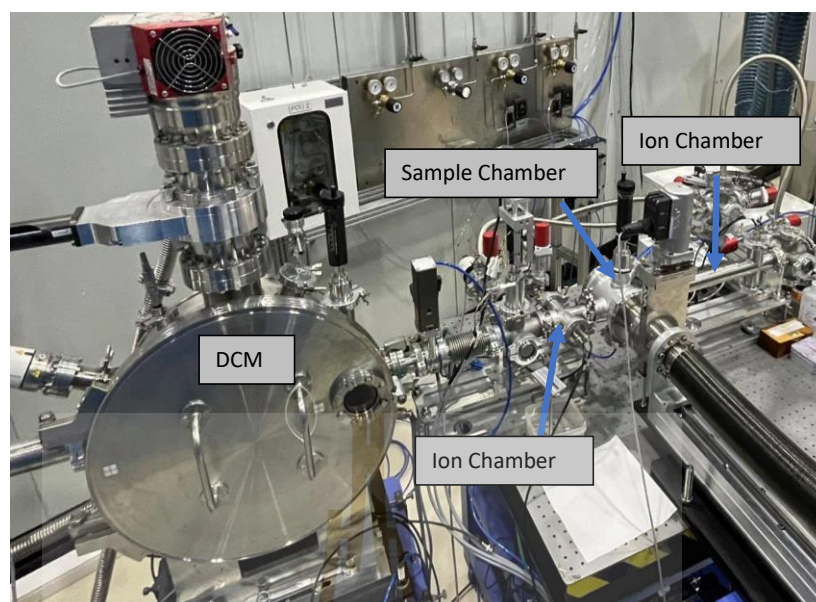
Figure 3.28 Transmission-mode X-ray absorption spectroscopy experimental setup diagram.

In addition to the transmission mode, the absorption coefficient may be determined using the fluorescence mode and the electron yield. When an x-ray photon knocks out an electron from the inner shell, another electron from a higher energy level cascades down to fill the hole, emitting radiation. As illustrated in figure 3.26(a), the discharged energy x-ray photon is released, and the fluorescence x-ray may be noticed. De-excitation may also produce the Auger effect, in which one electron is lowered to a lower energy level while another is stimulated to the continuum state and perhaps exits the sample, as indicated in figure 3.26(b), where it can be detected with electron-yield XAS detectors.

In fluorescence mode, we measure the intensities of the incoming x-ray photon beam and the fluorescence x-ray generated after the x-ray absorption. The fluorescence detector is typically positioned horizontally at 90° to the incoming x-ray photon beam, with the sample at an angle to the beam (typically 45°). Due to the fact that changes in the amount of elastically scattered x-rays contribute significantly to noise in fluorescence XAS, the detector's position is selected to minimize elastically scattered radiation by employing the x-ray beam's polarization. In the case of electron yield, we count the electrons that are emitted from the surface of the sample. Due to

the method's short route length (1000 Å), it is surface-sensitive, which may be useful if one is interested in near-surface occurrences. Additionally, it may aid in preventing the "self-absorption" phenomena that occurs during fluorescence mode. Both modes, on the other hand, are immediately equivalent to the absorption capacities of the sample. As a consequence, the three methodologies may be combined to determine the structure of a material by employing the absorption capacity of the sample.
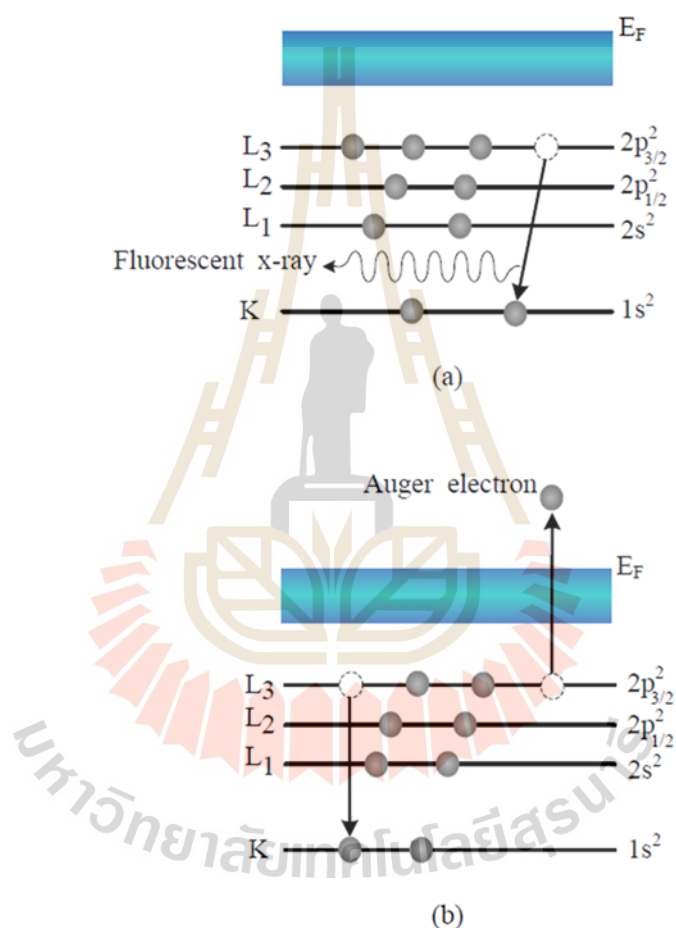
Figure 3.29 The excited state (a) x-ray fluorescence and (b) the Auger effect. (Koningsberger and Prins, 1988)

3.2.5.4 X-ray Absorption spectrum calculation

The FEFF 8.2 code is used to execute the majority of the theoretical calculations in this thesis. The FEFF (feff) project, created at the University of Washington's Department of Physics in Seattle, USA, makes use of this code to calculate x-ray absorption. Apart from calculating XAS spectra, the FEFF code is

capable of calculating x-ray natural circular dichroism (XNCD), spin-dependent x-ray magnetic dichroism (XMCD), nonresonant x-ray emission (XES), and electronic structure, including local densities of states (LDOS). The FEFF code is written in ANSI FORTRAN 77 by John J. Rehr and Alexei L. Ankudinov. (Rehr and Albers, 2000)

FEFF is a self-consistent real-space multiple-scattering (RSMS) technique for concurrently estimating the x-ray absorption spectrum and the electronic structure. As seen in figure 3.28, the input file "feff.inp" may be created straight from ATOMS code by using the "atoms.inp." command.

```
## This Atoms file was generated by Demeter 0.9.26
## Demeter written by and copyright (c) Bruce Ravel, 2006-2018

title = V2o5
space = P 1
a     =    3.63468     b    =     6.32490     c     =     11.41933
alpha = 90.00000    beta =  90.00000     gamma =  90.00000
rmax  =    5.45203    core = V0
polarization = 0.0  0.0  0.0
shift =      0.00000      0.00000      0.00000
atoms
# el.       x           y           z          tag
   V      0.00000     0.91602     0.14898     V0
   V      0.50000     0.08398     0.35112     V1
   V      0.50000     0.08398     0.64898     V2
   V      0.00000     0.91602     0.85112     V3
   O      0.00000     0.01512     0.00000     o4
   O      0.00000     0.66306     0.13984     o5
   O      0.50000     0.99135     0.18160     o6
   O      0.00000     0.00864     0.31840     o7
   O      0.50000     0.33694     0.36016     o8
   O      0.50000     0.98486     0.50000     o9
   O      0.50000     0.33694     0.63984     o10
   O      0.00000     0.00864     0.68160     o11
   O      0.50000     0.99135     0.81840     o12
   O      0.00000     0.66306     0.86016     o13
```

Figure 3.30 Detail of an atoms.inp input file to generate "feff.inp" for FEFF calculation.

The input file "feff.inp," which is shown in figure 3.30, may be updated to indicate the relevant FEFF-XAS spectrum calculation instructions, parameters, and atomic positions. This file contains information on the generator used to generate the input file and the number of atoms in the cluster. The next sections demonstrate how to distribute the stages of a calculation among several cards. The next section discusses the various sorts of atomic potentials and specified atomic symbols, followed by the created atoms' locations in the system, with the center atom at (0,0,0) in (x,y,z) coordination.

```
TITLE V2O5

HOLE      1   1.0   * FYI: (V K edge @ 5465 eV, 2nd number is S0
^2)
*            mphase,mpath,mfeff,mchi
CONTROL   1    1    1    1
PRINT     1    0    0    0

RMAX      5.0
 * POLARIZATION  0.0   0.0   0.0

POTENTIALS
 * ipot    Z       tag
    0      23      V
    1      23      V
    2      8       O

ATOMS                 * this list contains 32 atoms
 *   x          y          z      ipot tag            distance
   0.00000    0.00000    0.00000    0  V0              0.00000
   0.00000   -1.59995   -0.10323    2  O5.1            1.60327
   0.00000    0.62680   -1.70011    2  O4.1            1.81197
   1.81734    0.47645    0.37364    2  O6.1            1.91555
  -1.81734    0.47645    0.37364    2  O6.1            1.91555
   0.00000    0.58581    1.93580    2  O7.1            2.02250
   1.81734    1.06233    2.30945    1  V1.1            3.12487
  -1.81734    1.06233    2.30945    1  V1.1            3.12487
   0.00000    0.00000   -3.40022    1  V3.1            3.40022
   3.63468    0.00000    0.00000    1  V0.1            3.63468
  -3.63468    0.00000    0.00000    1  V0.1            3.63468
   0.00000   -1.59995   -3.29699    2  O13.1           3.66469
   3.63468   -1.59995   -0.10323    2  O5.2            3.97258
  -3.63468   -1.59995   -0.10323    2  O5.2            3.97258
   1.81734    2.66228    2.41268    2  O8.1            4.02634
  -1.81734    2.66228    2.41268    2  O8.1            4.02634
   3.63468    0.62680   -1.70011    2  O4.2            4.06130
  -3.63468    0.62680   -1.70011    2  O4.2            4.06130
   3.63468    0.58581    1.93580    2  O7.2            4.15950
  -3.63468    0.58581    1.93580    2  O7.2            4.15950
   1.81734    0.47645   -3.77386    2  O12.1           4.21566
  -1.81734    0.47645   -3.77386    2  O12.1           4.21566
   1.81734    0.43553    4.00956    2  O9.1            4.42368
```

Figure 3.31 Detail of a "feff.inp" input file of V_2O_5 with V as center atom for FEFF calculation.

3.3   Cyclic Voltammetry (CV)

In the discipline of electrochemistry, cyclic voltammetry (CV) is a very effective technique. It has been widely utilized to characterize the performance of a variety of electrical energy storage devices, including supercapacitors. CV approaches impose a periodic and linearly varying electric potential at the electrodes. As seen in figure 3.32, the ensuing electric current is recorded. Calculate the total charge accumulated at the electrode's surface by integrating the current with respect to time. Finally, capacitance may be calculated by dividing the total charge by the potential window. Generally, capacitance is measured at various scan rates to characterize the performance of energy storage devices such as supercapacitors. When we use a supercapacitor coin cell, cyclic voltammetry (CV) provides the specific capacitance of the cell (F g^{-1}). The following equation is used to compute.

$$I = \frac{dQ}{dt} = \frac{CdV}{dt} \qquad (3.40)$$

$$C = \frac{Idt}{dV} ; C = \frac{Q}{V} \qquad (3.41)$$

where I is current (ampere) and dV/dt is potential scan rate (v) in unit V/s

Therefore,

$$C = \frac{I}{V} \qquad (3.42)$$
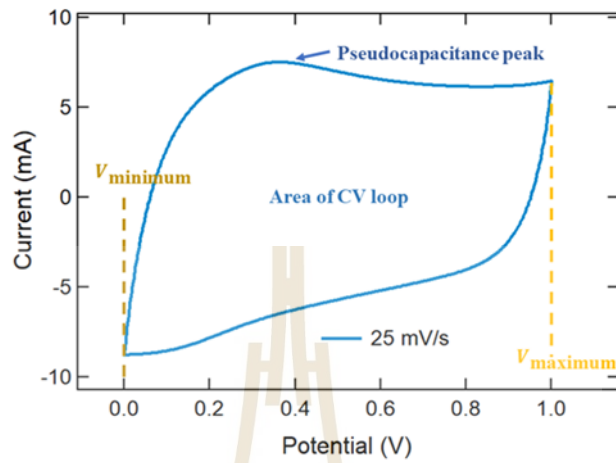
Figure 3.32 CV measurement example.

CHAPTER IV

LOCAL AND STRUCTURE OF VANADIUM

PENTAOXIIDE (V_2O_5) FILMS

In this chapter, vanadium oxide thin films were prepared by using the radio frequency reactive magnetron sputtering (RF magnetron sputtering) with Vanadium metal. The effect of deposition parameters such as gas flow rate on the structural and optical properties of the samples will be studied. The phase formation of the prepared samples was carried out using an X-ray diffractometer (XRD). The morphology of samples will be examined by Scanning Electron Microscope (SEM), Focused Ion Beam-Scanning Electron Microscope (FIB) and Atomic Force Microscope (AFM). The optical transmittance and reflectance will be obtained by UV-Visible spectrophotometry (UV-Vis) measurement. The local structure will be investigated by XAS. In particular, XANES will be used to gives information on oxidation state and site symmetry of V and EXAFS gives detailed information on bond lengths and coordination numbers of neighboring atom shells surrounding the V atom. The final products with optimal structural, electrical properties are expected to be used as the electrodes of electrochromic devices.

4.1 Thin films preparation

The vanadium oxide thin films were prepared by vanadium metal target (3 inches) 99.9% of purity, from Kurt J. Lesker. The target was placed at a distance of 6 cm from the substrates. The deposition conditions were fixed with the RF power of 200 W, based pressure less than 2.0×10^{-5} mbar, and Ar flow rate of 20 sccm, while the O_2 flow rates were varied by 1, 2, 3, 4, 5, and 6 sccm and the sputtering time was kept constant at 80 minutes. The vanadium oxide thin films were deposited on glass and Si (100) substrates to obtain the morphology, phase formation, and local structure.

Phase formation was investigated by the x-ray diffraction spectroscopy (XRD; BRUKER, D8 ADVANCE) with Cu Kα radiation). The film morphology was carried out by scanning electron microscopy (SEM) equipped with the energy-dispersive X-ray spectroscopy (EDS) (JEOL JSM-6010LV) and atomic force microscope (AFM) (Park Systems AFM XE-120). The local structure was characterized by synchrotron-based XANES and EXAFS spectra at the SUT-NANOTEC-SLRI XAS Beamline (BL5.2) at the Synchrotron Light Research Institute (Public Organization), Thailand.

Table 4.1 The sputtering condition of V_2O_5 thin films at different of O_2 and Ar flow rate.

Target	V-metal target (3 inches 99.9% of purity, from Kurt J. Lesker)
RF power	200 W
Base pressure	1×10^{-5} mbar
Operating pressure (O_2+Ar flow rate)	3×10^{-2} mbar
Distance of sample holder from target	6 cm
Sputtering time	80 minutes
O_2 flow rate	1, 2, 3, 4, 5, and 6 sccm
Ar flow rate	20 sccm
Substrate	Si (100), Glass slide, ITO and FTO glass
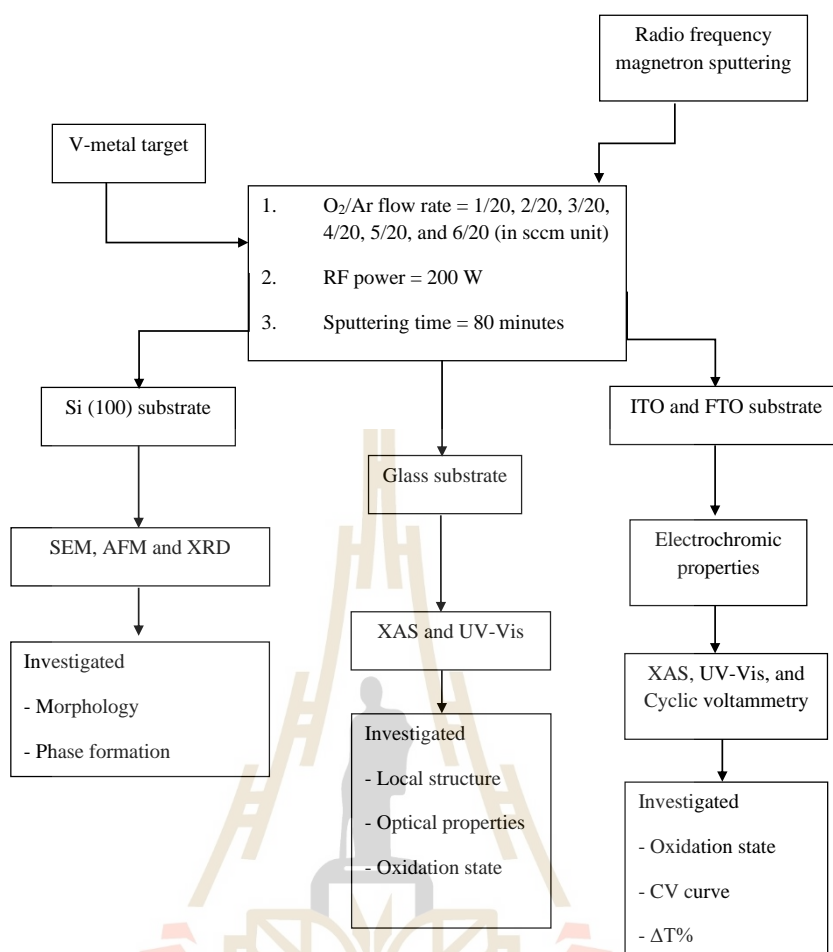
Figure 4.1 Flow chart of the synthesis of V_2O_5 thin films at different of O_2 and Ar flow rate.

4.2   Results and discussion

4.2.1 The Films morphology

Figure 4.2 showed the AFM images of vanadium oxide thin films at the O_2/Ar flow rate of (a) 1/20, (b) 2/20, (c) 3/20, (d) 4/20, (e) 5/20, and (f) 6/20 (in sccm unit). The surface roughness of prepared films with the O_2/Ar flow rate of 3/20, 4/20, 5/20, and 6/20 (in sccm unit) is higher than that of 1/20 and 2/20 (in sccm unit) because an increase of the working gas flow rate is thought to boost the energy flux at the substrate, which could contribute to a faster deposition rate and larger grain growth (Al-Mansoori et al., 2017).
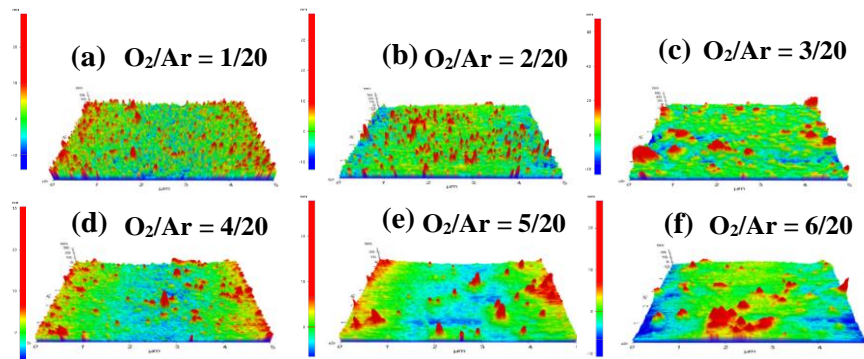
Figure 4.2 AFM images of vanadium oxide thin films at O_2/Ar flow rate of (a) 1/20, (b) 2/20, (c) 3/20, (d) 4/20, (e) 5/20, and (f) 6/20 (in sccm unit).

The SEM surface and cross-section images of vanadium oxide thin films with the O_2/Ar flow rate of 1/20, 2/20, 3/20, 4/20, 5/20, and 6/20 (in sccm unit) were shown in figure 4.3. From the SEM cross-section images, the average thickness of the films was approximately 152.59 nm because the sputtering duration was kept constant at 80 minutes, so the average thickness of films was considerably equal.
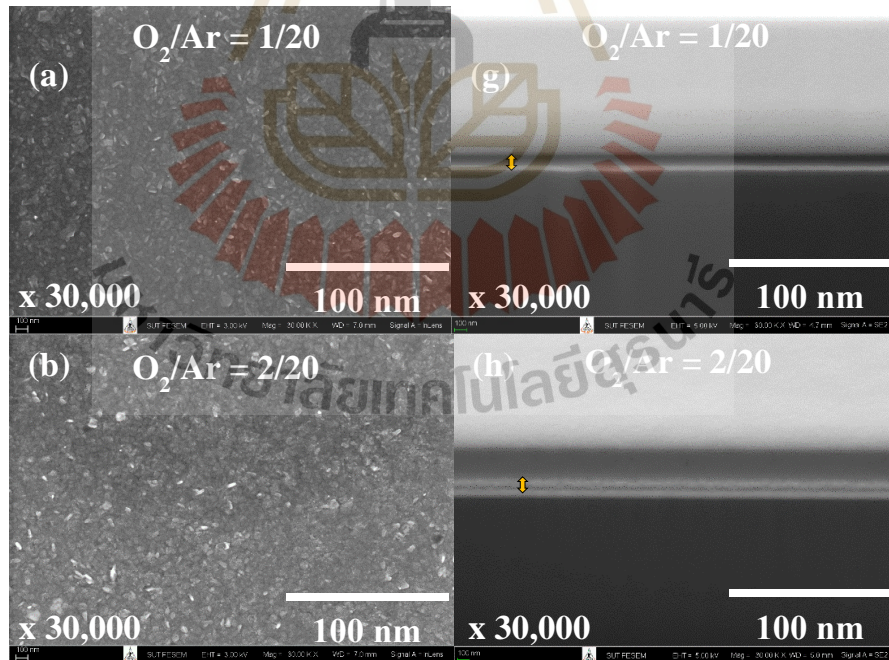
Figure 4.3 (Continuous) SEM surface images of vanadium oxide thin films at O_2/Ar flow rate of (a) 1/20, (b) 2/20, (c) 3/20, (d) 4/20, (e), 5/20 and (f) 6/20 (in sccm unit) and SEM cross-section images of vanadium oxide thin films at O_2/Ar flow rate of (g) 1/20, (h) 2/20, (i) 3/20, (j) 4/20, (k) 5/20, and (l) 6/20 (in sccm unit).
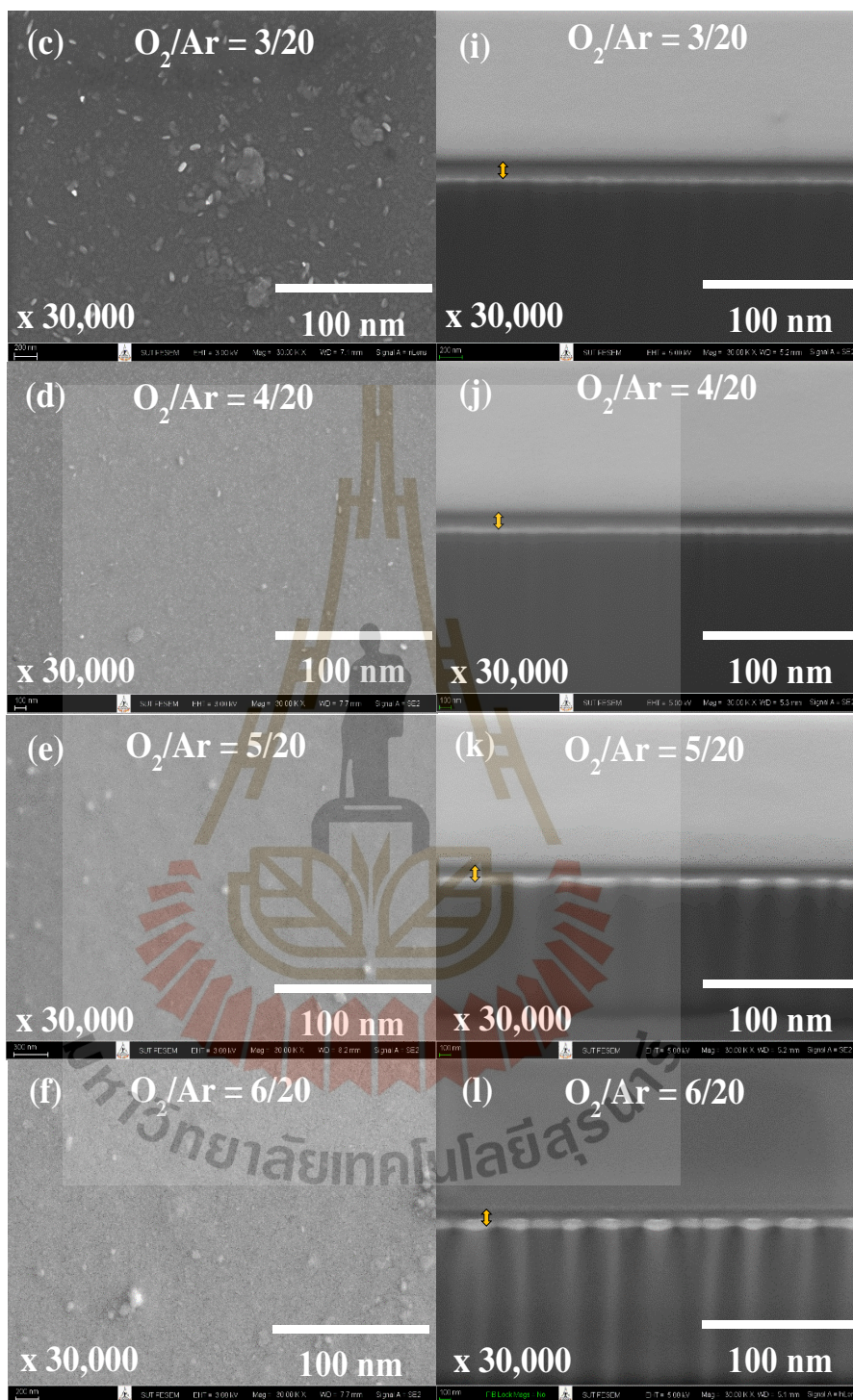
Figure 4.3 (Continuous) SEM surface images of vanadium oxide thin films at O_2/Ar flow rate of (a) 1/20, (b) 2/20, (c) 3/20, (d) 4/20, (e) 5/20, and (f) 6/20 (in sccm unit) and SEM cross-section images of vanadium oxide thin films at O_2/Ar flow rate of (g) 1/20, (h) 2/20, (i) 3/20, (j) 4/20, (k) 5/20, and (l) 6/20 (in sccm unit).

Table 4.2 Thickness of vanadium oxide thin films at different O_2/Ar flow rates.

O_2/Ar flow rate (in sccm unit)	Thickness (nm)
1/20	149.59
2/20	154.08
3/20	154.06
4/20	149.66
5/20	158.55
6/20	149.61
average	152.59

Figure 4.4 was shown the EDS results, V and O signal was clearly observed indicating an existence of V and O atoms in the films. It should be noted that the samples are composed of only two elements (vanadium and oxygen). The atomic and weight ratios of O/V of the films with all conditions were shown in table 4.5 and table 4.6, respectively. The film with the O_2/Ar flow rate of 3/20 (in sccm unit) possessed an atomic and weight ratio of 2.29 and 0.72, respectively, which are very close to those O/V ratios of V_2O_5 (Kumagai et al., 1998).

As seen from table 4.3 and table 4.4, higher concentrations of O_2 gas resulted in a drop in deposition rate due to a decrease in the sticking coefficient. Furthermore, as the O_2 concentration rose, the argon gas pressure fell, obstructing the passage of argon ions towards the target. The thin film with an O_2/Ar ratio of 3/20 (in sccm units) performed the closest O/V atomic and weight ratio to those of V_2O_5. This probably suggests the most appropriate condition for fabricating the V_2O_5 thin film.
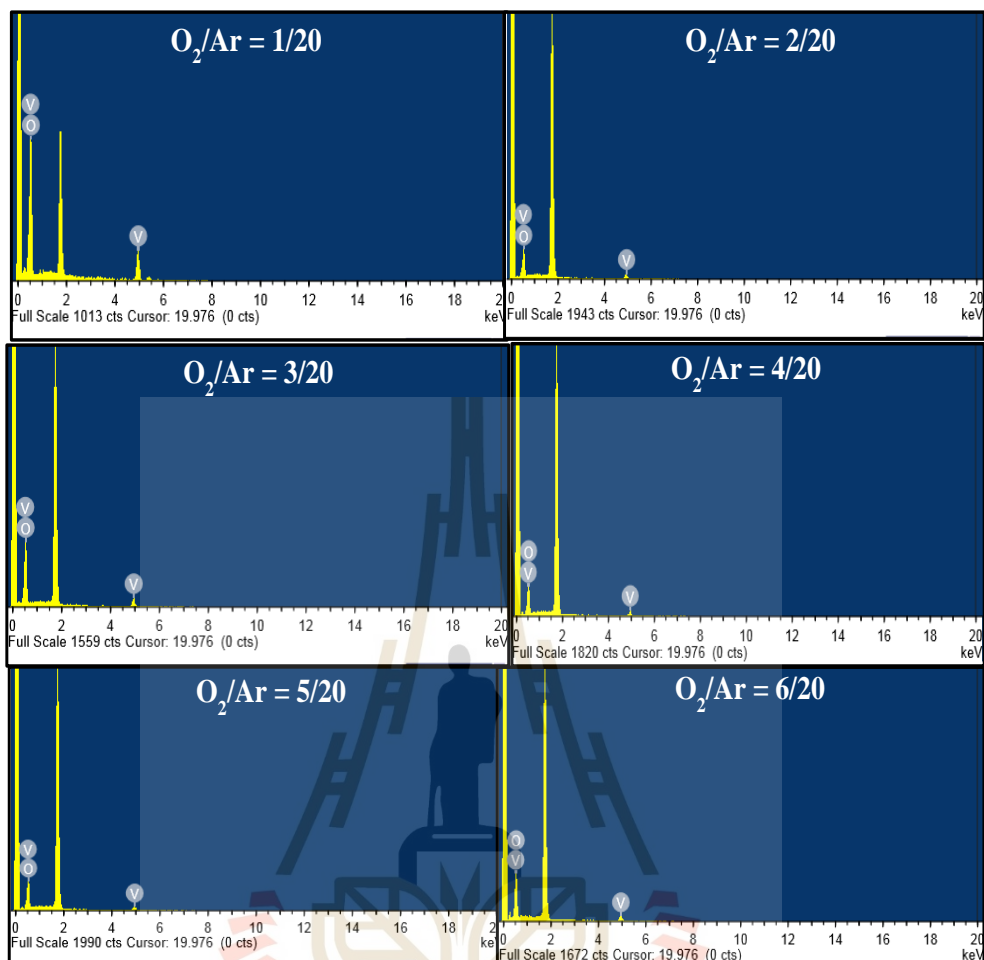
Figure 4.4 EDS spectra of vanadium oxide thin films at the O_2/Ar flow rate of (a) 1/20, (b) 2/20, (c) 3/20, (d) 4/20, (e) 5/20, and (f) 6/20 (in sccm unit).

Table 4.3 Weight (%) of vanadium oxide thin films at various O_2/Ar flow rates.

O_2/Ar flow rate (in sccm unit)	weight (%)		O/V
	O	V	
1/20	22.73	77.27	0.30
2/20	33.22	66.78	0.50
3/20	41.86	58.14	0.72
4/20	35.06	64.94	0.54
5/20	36.81	61.69	0.60
6/20	32.96	67.04	0.49

Table 4.4 Atomic (%) of vanadium oxide thin films at various O_2/Ar flow rates.

O_2/Ar flow rate (in sccm unit)	Atomic (%)		O/V
	O	V	
1/20	48.02	51.98	0.95
2/20	61.30	38.70	1.58
3/20	69.62	30.38	2.29
4/20	63.22	36.78	1.72
5/20	66.40	33.6	1.98
6/20	61.02	38.98	1.57

Figure 4.5 %Weight (a) and %Atomic (b) of vanadium oxide thin films at the O_2/Ar flow rate of 1/20, 2/20, 3/20, 4/20, 5/20, and 6/20 (in sccm unit).

4.2.2 Phase formation of V_2O_5 thin films
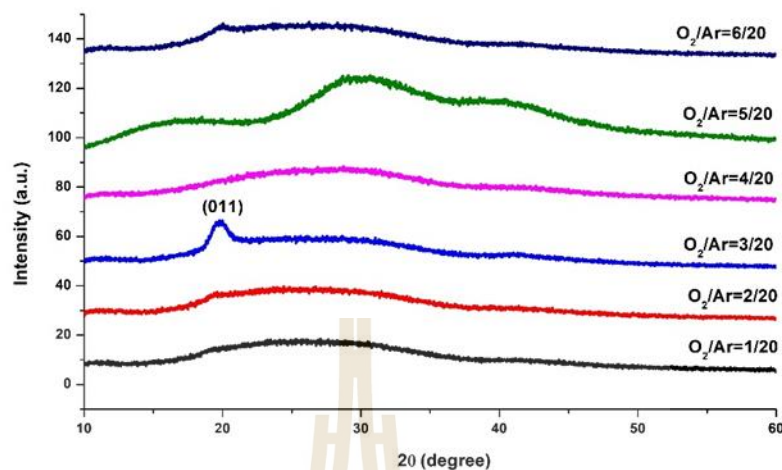
Figure 4.6 X-ray diffraction patterns of vanadium oxide thin films at the O_2/Ar flow rate of 1/20, 2/20, 3/20, 4/20, 5/20, and 6/20 (in sccm unit).

For investigating the crystal structures of vanadium oxide thin films, all thin-film samples fabricated at the O_2/Ar flow rate of 1/20, 2/20, 3/20, 4/20, 5/20, and 6/20 (in sccm unit) were characterized by the X-ray diffraction technique (XRD) and their diffraction patterns were shown in figure 4.6. The XRD patterns could be indexed to V_2O_5. At the O_2/Ar flow rate of 3/20 (in sccm unit) in a 2θ range of $10°$ - $60°$, the diffraction peak at $20.36°$ corresponding to the (011) plane of orthorhombic V_2O_5 (space group Pmmn according to the standard mp-754670_V_2O_5 (from material project) and fit with JANA program) was detected (Chan et al., 2014). No other diffraction peak was detected in the O_2/Ar flow rate of 1/20, 2/20, 4/20, 5/20, and 6/20 (in sccm unit) sample. From XRD results, it was found that the thin-film sample with the O_2/Ar flow rate of 3/20 (in sccm unit) was composed of only V_2O_5 phase as identified by (011) plane. The crystal phase within the samples of an O_2/Ar flow rate of 1/20, 2/20,4/20, 5/20, and 6/20 (in sccm unit) was not detected because these samples were an amorphous phase. The XRD results of all thin-film samples would be further confirmed by the XAS technique.

4.2.3 Optical properties

The absorbance and transmittance spectra of vanadium oxide thin films on glass slide substrate with different O_2/Ar flow rate were shown in figure 4.7. The

absorption edges were clearly observed at around 400-600 nm which was corresponded to the energy band gap of the V_2O_5 thin films.
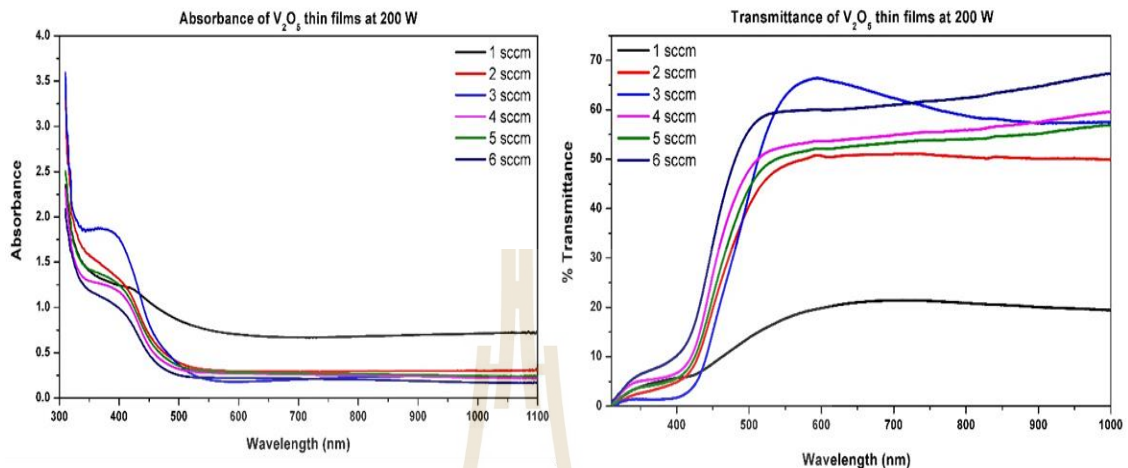
Figure 4.7 The absorbance (left) and transmittance (Right) spectra of vanadium oxide thin films at the O_2/Ar flow rate of 1/20, 2/20, 3/20, 4/20, 5/20, and 6/20 (in sccm unit).

From figure 4.7, the absorbance and transmittance spectra of V_2O_5 thin films at O_2/Ar flow rate of 1/20 (in sccm unit) are difficult to transmit because of this condition is close to metal on glass. From these result, transmittance spectra of V_2O_5 thin film sputtered onto glass slide at O_2/Ar flow rate of 1/20, 2/20, 3/20, 4/20, 5/20 and 6/20 (in sccm unit) were used to calculate the energy band gap of the film with the following equation

- Photon energy is directly proportional to frequency and photon's wavelength.

$$E = hf = \frac{hc}{\lambda}; c = 3 \times 10^8 \frac{m}{s} \tag{4.1}$$

where

E is photon energy (J)

f is frequency (Hz)

c is the speed of light in vacuum (m/s)

λ is photon's wavelength (m)

The value of energy band gap was extracted from transmittance spectra by plotting $(\alpha h\nu)^2$ vs $h\nu$ and extrapolating the linear portion of the curve to zero. From table 4.5, The energy band gap of the V_2O_5 thin films at O_2/Ar flow rate of 1/20, 2/20, 3/20, 4/20, 5/20 and 6/20 (in sccm unit) were estimated to be 2.40, 2.62, 2.74, 2.72,

2.73, and 2.74 eV, respectively. Therefore, the energy band diagram can be drawn as an inset of figure 4.8
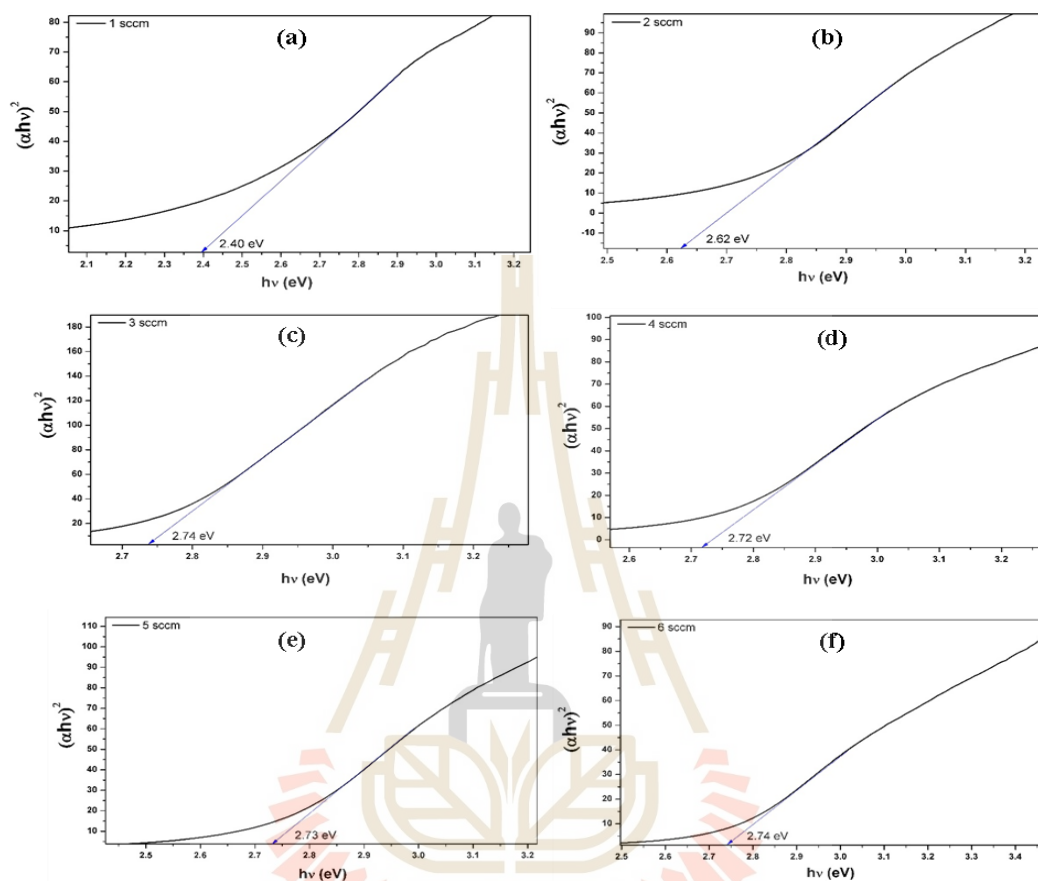
Figure 4.8 Relation between $(\alpha h\nu)^2$ and $h\nu$ of vanadium oxide thin films at the O_2/Ar flow rate of (a) 1/20, (b) 2/20, (c) 3/20, (d) 4/20, (e) 5/20, and (f) 6/20 (in sccm unit).

Table 4.5 The energy band gap of vanadium oxide thin films at different O_2/Ar flow rate.

O_2/Ar flow rate (in sccm unit)	Energy gap (eV)
1/20	2.40
2/20	2.62
3/20	2.74
4/20	2.72
5/20	2.73
6/20	2.74

4.2.4 XAS data analysis

Synchrotron-based XANES and EXAFS spectra were conducted at the SUT-NANOTEC-SLRI XAS Beamline (BL5.2) at the Synchrotron Light Research Institute (Public Organization), Thailand (Kidkhunthod., 2017; Klysubun et al.,2017). The experiment XAS, which included XANES and EXAFS spectra at V K-edge spectra, was collected in fluorescence modes to describe the valence states and local structural information of vanadium atoms. Using reference V metal spectra, the vanadium K-edge absorption measurements were calibrated and aligned, with the maximum value of the first derivative set at 5465 eV.

4.2.4.1 Local structure of V_2O_5 thin films
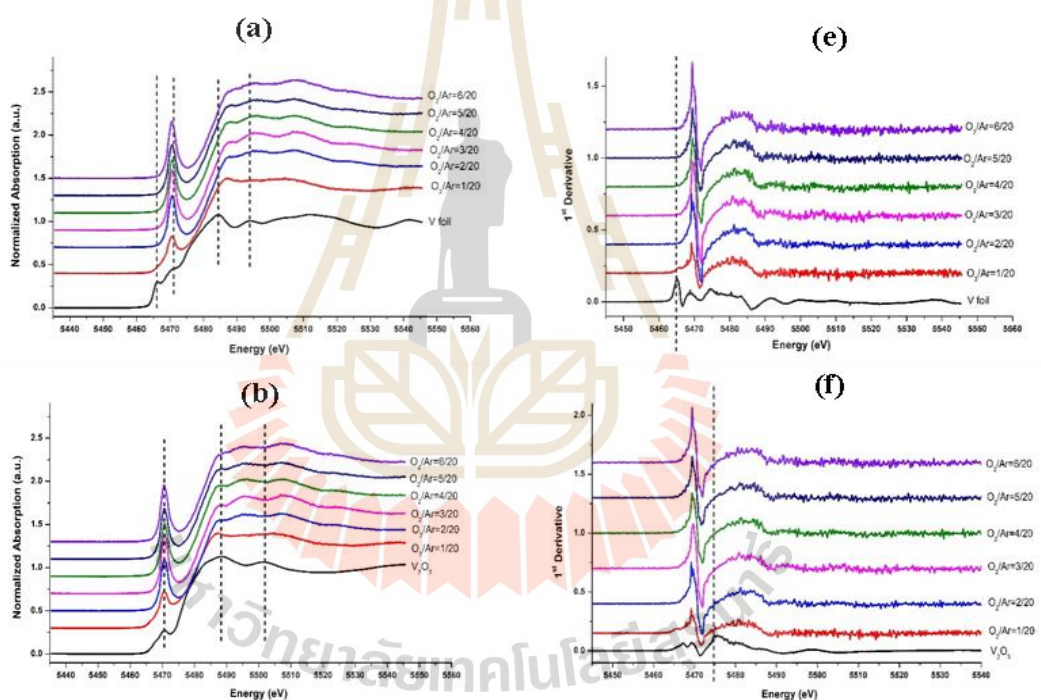
Figure 4.9 (Continuous) Normalized V K-edge XANES spectra ((a)-(d)) and the corresponding first derivatives ((e)-(h)) of vanadium oxide thin films at the O_2/Ar flow rate of 1/20, 2/20, 3/20, 4/20, 5/20, and 6/20 (in sccm unit) with V-foil, V_2O_3, VO_2 and V_2O_5 standard samples (Kidkhunthod et al., 2016).
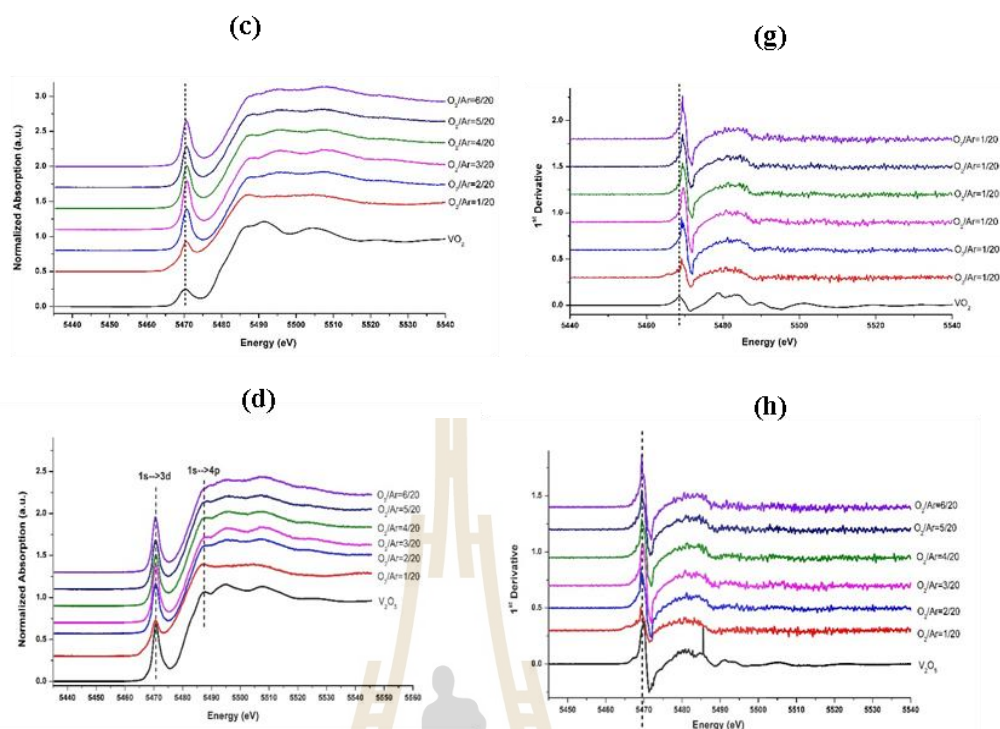
Figure 4.9 (Continuous) Normalized V K-edge XANES spectra ((a)-(d)) and the corresponding first derivatives ((e)-(h)) of vanadium oxide thin films at the O_2/Ar flow rate of 1/20, 2/20, 3/20, 4/20, 5/20, and 6/20 (in sccm unit) with V-foil, V_2O_3, VO_2 and V_2O_5 standard samples (Kidkhunthod et al., 2016).
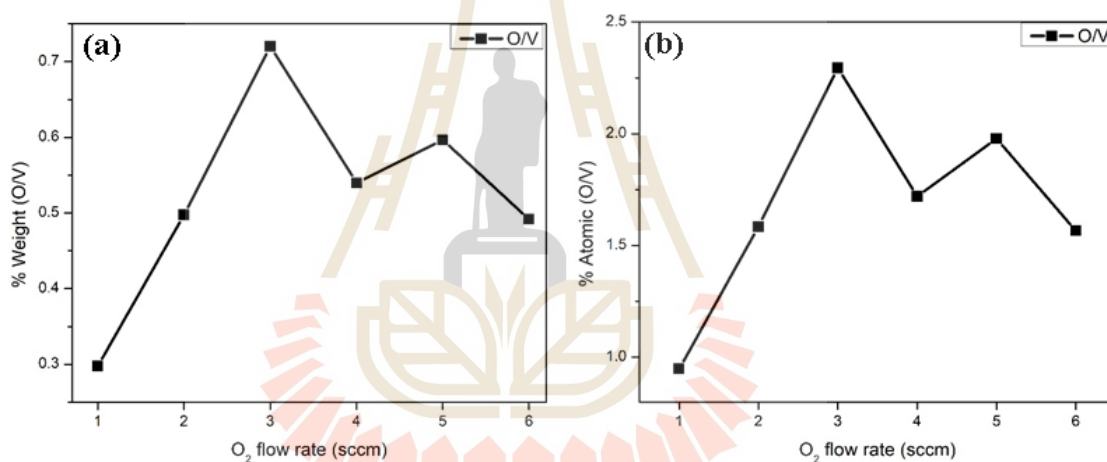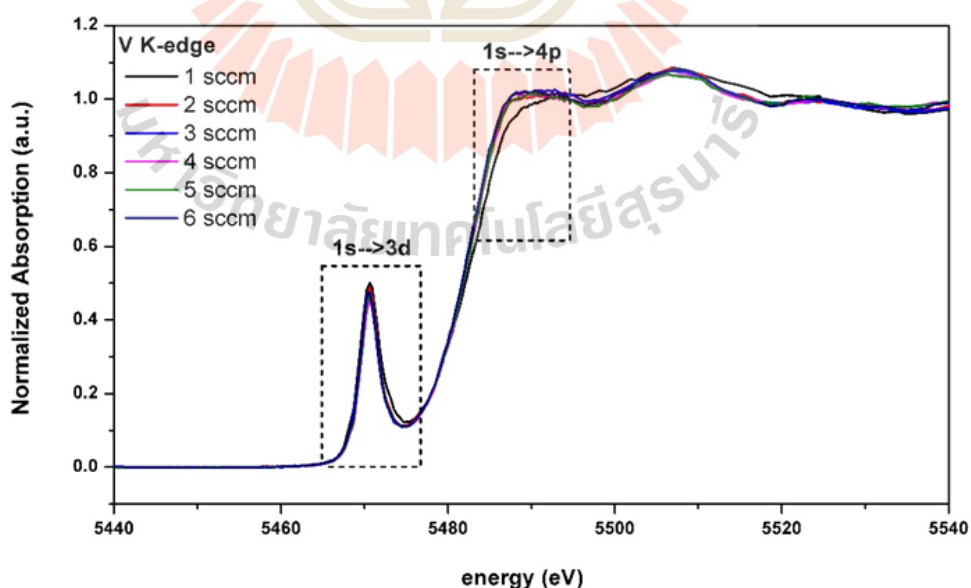

Figure 4.10 Normalized V K-edge XANES spectra of vanadium oxide thin films at the O_2/Ar flow rate of 1/20, 2/20, 3/20, 4/20, 5/20, and 6/20 (in sccm unit).

A majority vanadium oxide phase can be used to study the electronic structure and local structure around V atoms using the XAS technique. Figure 4.9 showed the normalized V K-edge XANES spectra and their first derivatives of the O_2/Ar flow rate of 1/20, 2/20, 3/20, 4/20, 5/20, and 6/20 (in sccm unit) thin-film, V-foil, V_2O_3, and V_2O_5 standard samples. The characteristic absorption edge of V existed at 5465 eV, which corresponds to the energy required to eject a core electron from a vanadium atom. The most intense peak near 5464-5469 eV (Stizza et al., 1989; Šipr et al., 1999; Wong et al., 1984; Poumellec et al., 1998) deconvoluted from XANES showed that the films contained the V^{3+}, V^{4+} and V^{5+} with the oxidation states of 3+, 4+ and 5+ (from Linear combination fit in table 4.6.) (Patridge et al., 2013; Ekwongsa et al., 2020). Since the deposited VOx was a mix of vanadium oxide phases. The white line peaks observed in XANES spectra refered to the electronic 1s→3d transitions, whereas the broad peaks around 5490 eV came from the 1s→4p transition (Nabavi et al., 1991). So, the O_2/Ar flow rate obviously affected the oxidation state of vanadium oxide thin films. As mentioned previously, the XANES results were used for the study of oxidation state of vanadium thin films at the O_2/Ar ratio of 1/20, 2/20, 3/20, 4/20, 5/20, and 6/20 (in sccm unit). The plots showed that, vanadium thin films contained the 1s→3d transition peak (around 5464-5469 eV) and the 1s→4p transition peak (around 5490 eV) at all O_2/Ar ratios (as seen in figure 4.9(d)) depicting that the crystal structure of V_2O_5 (V^{5+}) was orthorhombic wurtzite. From figure 4.10, the O_2/Ar ratio of 1/20 (in sccm unit) revealed the lowest intensity at the 1s→3d transition peak compared to the others. By increasing the O_2/Ar ratio to 2/20 (in sccm unit), the 1s→3d transition peak intensity increased. The increase in an intensity of 1s→3d transition peak is attributed to the development of the V_2O_5 (V^{5+}) formation. Similarly, when O_2/Ar ratio increased to 3/20 -6/20 (in sccm unit), the 1s→3d transition peak's intensities further increased comparative to that of 1/20 ratio. Especially, focusing on the O_2/Ar ratio of 3/20 (in sccm unit), this condition performed the highest intensity peak of the 1s→3d transition. This implies to the strongest enhancement in the vanadium metal form to V_2O_5 (V^{5+}). The sample with an O_2/Ar flow rate of 1/20 (in sccm unit) was made up of a mix of amorphous V_2O_5 and V_2O_3, whereas the rest was made up entirely of

amorphous V_2O_5, except the 3/20 ratio condition which had the highest crystallinity. An increase of O_2 flow rate is highly believed of causing an increase in energy flux and enlargement of the 1s⟶3d transition peak's intensity at the substrate, which can lead to a higher deposition rate. Therefore, to achieve a desired V_2O_5 structure, the gas flow rate would be adjusted to accomplish. The sole XANES results were not able to provide deeply information on the local structure of vanadium oxide. The peak near 5464-5469 eV (Wu et al., 2004) could be due to a mixture of several coordinations or a rather large distribution of crystal fields around vanadium (Ravel and Newville, 2005). This suggests a significant change in V local structure especially for coordinated oxygen atoms surrounding V atom. This would be further discussed in the EXAFS section.

Table 4.6 Linear combination fit of %V_2O_3, %V_2O_5 and %VO_2 of vanadium oxide thin films at different O_2/Ar flow rates.

O_2/Ar flow rate (in sccm unit)	% V_2O_3	% V_2O_5	%VO_2
1/20	1	58	41
2/20	6	77	19
3/20	7	81	12
4/20	8	73	19
5/20	7	75	18
6/20	7	76	17

In order to understand the local environment of V atoms in the structure, the EXAFS spectra were intensively analyzed and fitted using Athena and Artemis programs as implement in the IFEFFIT packages (Al-Mansoori et al., 2015; Wong et al., 1984). The EXAFS spectra of the corresponding Fourier transform (FT) in R space at V K-edge of all samples were shown in figure 4.11. It can be seen that the amplitudes of V–O and V–V peaks were not significantly different. These patterns can be identified as the V_2O_5 orthorhombic structure as they were best fitted with the V_2O_5 model with a good R-factor (good R-factor for fitting is between 1-5%). In addition, the investigation of structural parameters of the local environment around the V atom was analyzed based

on FT fitting. Plots of V K-edge K[3] weighted Fourier transform fitting from the experiment (red line) and fitted line (black circle) of all vanadium oxide thin films were shown in figure 4.11. The FT provided information on the partial atomic distribution around the V atoms in the V_2O_5 system. For the sample with the O_2/Ar flow rate of 2/20, 3/20, 4/20, 5/20, and 6/20 (in sccm unit), the resulting filtered data and wavenumber in a range of 2-9 Å were shown in figure 4.11 (Prins and Koningsberger, 1988). The FT spectra of R space showed that the single scattering contributions from the location of four V–O shells and the next location of two V–V shells were determined (Li et al., 1995). The V–O and V–V models of the V_2O_5 orthorhombic structure were used for the fit. The parameters of the EXAFS fitting such as interatomic distances (R), Debye-Waller factors (σ^2), amplitude reduction (S_0^2), and R-factor were shown in table 4.7 (Mansour et al., 2002). In the special case at 1/20 of O_2/Ar flow rate (in sccm unit) sample, EXAFS data was not fitted by Artemis programs because the unit cell of 1/20 of O_2/Ar condition (in sccm unit) was combined by the 55.8% V_2O_3 and 44.2% V_2O_5 (from Linear combination fit). Additionally, the EXAFS fitting data of the 2/20 – 6/20 of O_2/Ar flow rate (in sccm unit) samples implied and supported the XANES results for the structural environment around V atoms in the V_2O_5 orthorhombic structure. A local structure was discovered to be affected directly by the flow rate of O_2/Ar gas. Increasing the O_2/Ar gas flow rate is thought to enhance energy flux at the substrate, which might contribute to a faster deposition rate.
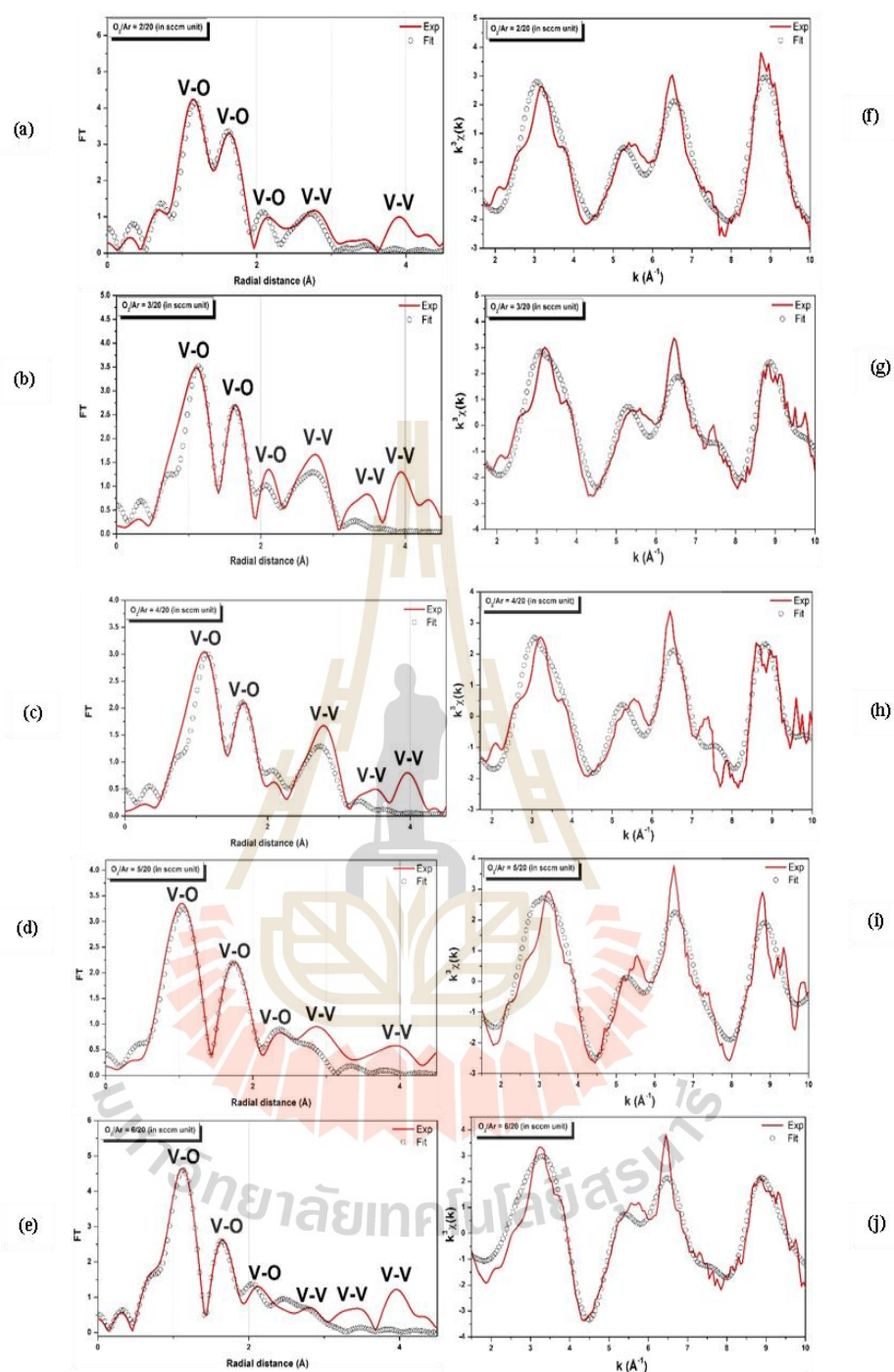
Figure 4.11 Fourier transform of EXAFS spectra at V K-edge (left) obtained from the experiment (red line) and fitting (black circle) of vanadium oxide thin films at the O_2/Ar flow rate of (a) 2/20, (b) 3/20, (c) 4/20, (d) 5/20, and (e) 6/20 (in sccm unit) and k^3-weighted EXAFS data (right) of vanadium oxide thin films at the O_2/Ar flow rate of (f) 2/20, (g) 3/20, (h) 4/20, (i) 5/20, and (j) 6/20 (in sccm unit).

**Table 4.7** EXAFS fitting parameters of interatomic distance (R), coordination number (N), Debye-Waller factor (σ^2), and amplitude reduction (S_0^2) of O_2/Ar flow rate at 2/20, 3/20, 4/20, 5/20, and 6/20 (in sccm unit).

Sample	Shell	N	σ^2	R(Å)	R-factor	S_0^2
2/20 (in sccm unit)	V–O	1	0.00090	1.62346	2.42%	0.70
	V–O	1	0.00102	1.83479		
	V–O	2	0.00569	1.95214		
	V–O	1	0.00718	1.61986		
	V–V	2	0.01316	3.12490		
	V–V	1	0.01432	3.40020		
3/20 (in sccm unit)	V–O	1	0.00300	1.59091	4.18%	0.70
	V–O	1	0.00339	1.79799		
	V–O	2	0.00607	1.92997		
	V–O	1	0.00766	1.63959		
	V–V	2	0.01034	3.10404		
	V–V	1	0.01125	3.37750		
4/20 (in sccm unit)	V–O	1	0.00427	1.61004	3.86%	0.7
	V–O	1	0.00483	1.81962		
	V–O	2	0.00745	1.95514		
	V–O	1	0.00940	1.62942		
	V–V	2	0.01052	3.10334		
	V–V	1	0.01145	3.37675		

Table 4.7(Continuous) EXAFS fitting parameters of interatomic distance (R), coordination number (N), Debye-Waller factor (σ^2), and amplitude reduction (S_0^2) of O_2/Ar flow rate at 2/20, 3/20, 4/20, 5/20, and 6/20 (in sccm unit).

Sample	Shell	N	σ^2	R(Å)	R-factor	S_0^2
5/20 (in sccm unit)	V–O	1	0.00112	1.51349	3.32%	0.850
	V–O	1	0.00127	1.71048		
	V–O	2	0.00296	1.91254		
	V–O	1	0.00313	1.66504		
	V–V	2	0.01581	3.06517		
	V–V	1	0.01720	3.33522		
6/20 (in sccm unit)	V–O	1	0.00311	1.58977	1.60%	0.98
	V–O	1	0.01005	1.55009		
	V–O	2	0.01106	1.82494		
	V–O	1	0.01600	2.32811		
	V–V	2	0.01700	3.04011		
	V–V	1	0.01750	3.35546		

CHAPTER V

LOCAL STRUCTURE AND ELECTROCHROMIC PROPERTIES OF

VANADIUM PENTAOXIIDE (V_2O_5) FILMS

5.1 Experiment

5.1.1 Thin films preparation

The vanadium oxide thin films were prepared by vanadium metal target (3 inches) 99.9% of purity, from Kurt J. Lesker. The target was placed at a distance of 6 cm from the substrates. The deposition conditions were fixed with the RF power of 200 W, based pressure less than 2.0×10^{-5} mbar, and Ar flow rate of 20 sccm, while the O_2 flow rates were varied by 1, 2, 3, 4, 5, and 6 sccm and the sputtering time was kept constant at 80 minutes. The vanadium oxide thin films were deposited on glass and Si (100) substrates to obtain the morphology, phase formation, and local structure.

Phase formation was investigated by the x-ray diffraction spectroscopy (XRD; BRUKER, D8 ADVANCE) with Cu Kα radiation). The film morphology was carried out by scanning electron microscopy (SEM) equipped with the energy-dispersive X-ray spectroscopy (EDS) (JEOL JSM-6010LV) and atomic force microscope (AFM) (Park Systems AFM XE-120). The local structure was characterized by synchrotron-based XANES and EXAFS spectra at the SUT-NANOTEC-SLRI XAS Beamline (BL 5.2) at the Synchrotron Light Research Institute (Public Organization), Thailand.

5.1.2 Cyclic voltammetry measurement

The electrochemical of sodium-ion insertion/extraction properties of the V_2O_5 thin films at O_2/Ar of 1/20, 2/20, 3/20, 4/20, 5/20, and 6/20 (in sccm unit) were investigated in 0.154 M NaCl solution and using the two-electrode system, in which Pt plate were used as the counter and reference electrodes. Cyclic voltammetry was performed between −1.8 and +1.8 V (versus Pt) at a scanning rate of 10 mV/s using a potentiostat/galvanostat.

Table 5.1 The sputtering condition of V_2O_5 thin films at different of O_2 and Ar flow rate.

Target	V-metal target (3 inches 99.9% of purity, from Kurt J. Lesker)
RF power	200 W
Base pressure	1×10^{-5} mbar
Operating pressure (O_2+Ar flow rate)	3×10^{-2} mbar
Distance of sample holder from target	6 cm
Sputtering time	80 minutes
O_2 flow rate	1, 2, 3, 4, 5, and 6 sccm
Ar flow rate	20 sccm
Substrate	FTO glass
Electrolyte	NaCl
Counter electrode	Pt plate
Scanning rate	10 mV/s
Potential window	-1.8 V to +1.8 V
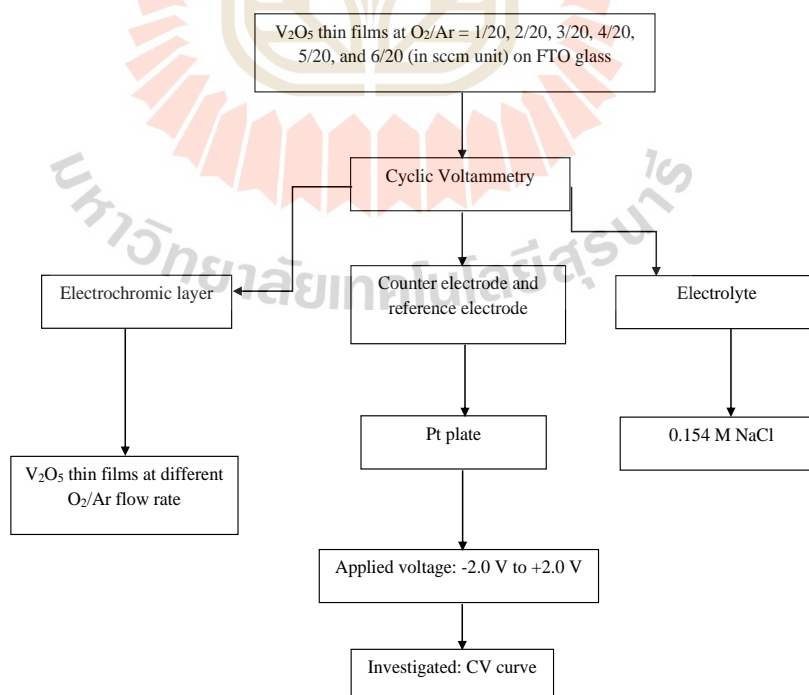
Figure 5.1 Flow chart of the of V_2O_5 thin films at different of O_2 and Ar flow rate for measurement the cyclic voltammetry.
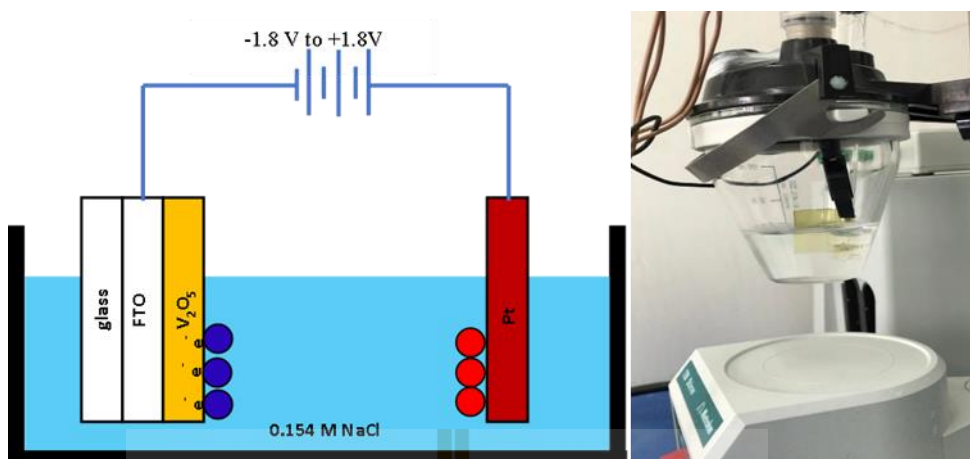
Figure 5.2 Schematic diagram of electrochromic structures and Na insertion into V_2O_5 structure (left) and the photo of two-electrode of electrochromic cell for cyclic voltammetry.
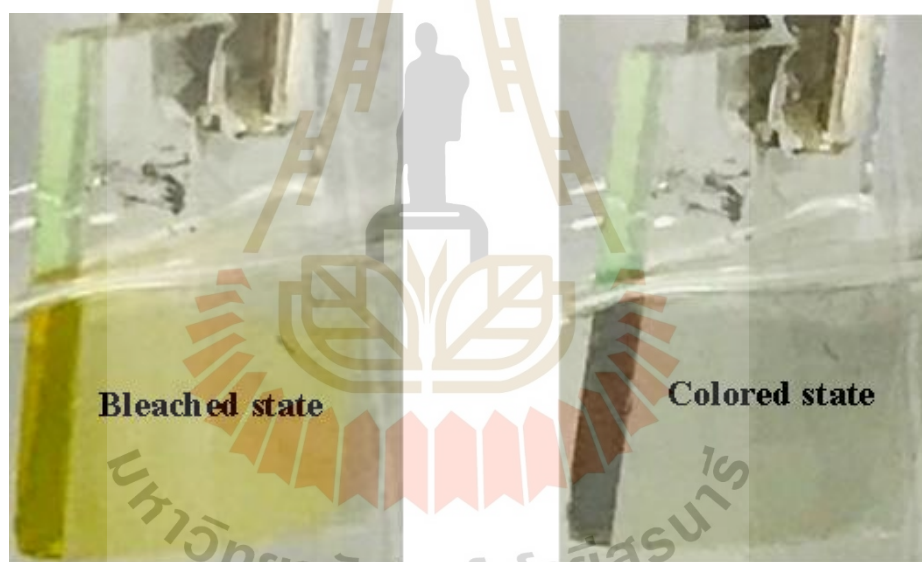
Figure 5.3 The photos exhibit the color changes of the film.

5.1.3 XAS and UV-Vis measurements

The sodium-ion insertion/extraction and optical properties of the V_2O_5 thin films at O_2/Ar of 1/20, 2/20, 3/20, 4/20, 5/20, and 6/20 (in sccm unit) were investigated in 0.154 M NaCl solution and using the two-electrode system, in which Ni foam sheet and Cu plate were used as the counter. Potential window was performed between −1.8 and +1.8 V for XAS and -0.3 V to +0.3 V for UV-Vis.

Table 5.2 The sputtering condition of V_2O_5 thin films at different of O_2 and Ar flow rate.

Target	V-metal target (3 inches 99.9% of purity, from Kurt J. Lesker)
RF power	200 W
Base pressure	1×10^{-5} mbar
Operating pressure (O_2+Ar flow rate)	3×10^{-2} mbar
Distance of sample holder from target	6 cm
Sputtering time	80 minutes
O_2 flow rate	1, 2, 3, 4, 5, and 6 sccm
Ar flow rate	20 sccm
Substrate	FTO glass and ITO glass
Electrolyte	NaCl
Counter electrode	Ni foam sheet and Cu plate
Potential window	-1.8 V to +1.8 V (for FTO and Ni foam electrode) and -0.3 V to 0.3 V (for ITO and Cu plate electrode)
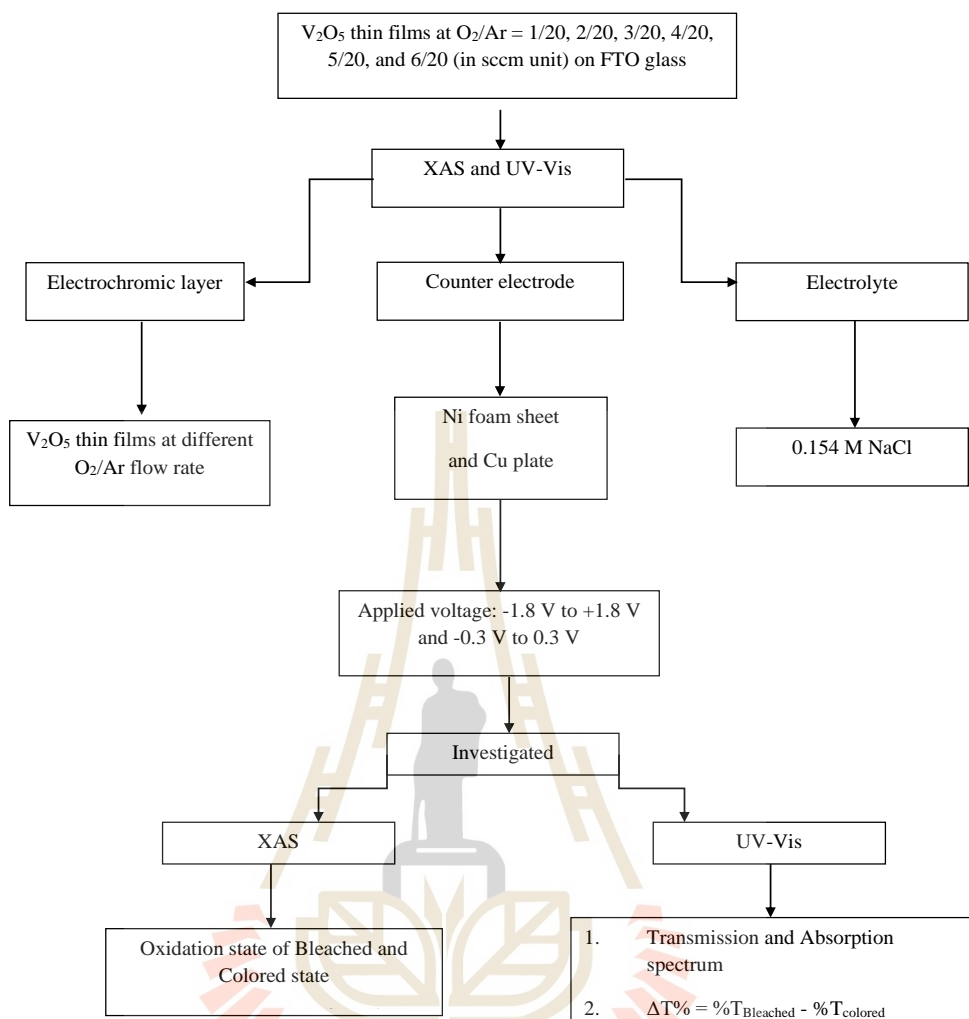
Figure 5.4 Flow chart of the of V_2O_5 thin films at different of O_2 and Ar flow rate for measurement the XAS and UV-Vis.

Figure 5.5 Schematic diagram of electrochromic structures and Na insertion into V_2O_5 structure (left) and the photo of two-electrode of electrochromic cell for XAS and UV-vis measurement.
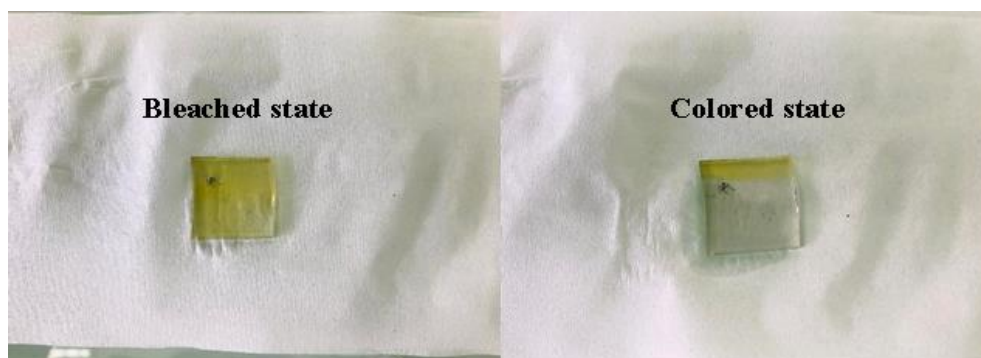
Figure 5.6 The photos exhibit the color changes of the film.

5.2   Results and discussions

5.2.1 Electrochromic properties

The electrochemical behavior of the V_2O_5 material was investigated using the two-electrode system, in which Pt sheet were used as the counter and reference electrodes. Cyclic voltammetry was adopted to investigate the Na insertion/extraction behavior in 0.154 M NaCl solution with a scan rate of 10 mV/s. Figure 5.7 (left) shows typical cyclic voltammograms of V_2O_5 electrodes with different O_2/Ar flow rate (in sccm unit) in the potential range of −2.0 to 2.0 V. The electrochemical Na+ insertion process occurring at V_2O_5 electrodes can be expressed by $V_2O_5 + xNa^+ + xe^- \leftrightarrow Na_xV_2O_5$, which is accompanied by color changes. These processes lead to film coloration [dark yellow→yellow→transparent (Figure 5.7 (right))]. Moreover, compared with the V_2O_5 electrode at O_2/Ar flow rate of 1/20-6/20 (in sccm unit) at applied potentials in the order of 0 to 1.0 V, all the peaks from the V_2O_5 electrode at O_2/Ar flow rate of 1/20 shifted to increased potentials but at applied potentials in the order of 1.0 to 2.0 V, all the peaks from the V_2O_5 electrode at O_2/Ar flow rate of 1/20 shifted to decreased potentials.

From figure 5.7, the cyclic voltammograms of V_2O_5 thin film sputtered onto FTO at O_2/Ar flow rate of 1/20, 2/20, 3/20, 4/20, 5/20, and 6/20 (in sccm unit) were used to calculate the specific capacitance of the film with the following equation

- CV measurement, I (current) is a function of voltage or I(V). So, we can write other form of I(V).

$$I = I(V) = \frac{\int_{V_{minimum}}^{V_{maximum}} I(V)dV}{\text{Potential window or Potential rang of CV}}$$

$$= \frac{\text{Area of CV loop}}{V_{\text{maximum}} - V_{\text{minimum}}} = \frac{\int_{V_{\text{minimum}}}^{V_{\text{maximun}}} I(V)dV}{V_{\text{maximum}} - V_{\text{minimum}}} \tag{5.1}$$

Therefore,

$$C = \frac{I}{v} = \frac{\frac{\int_{V_{\text{minimum}}}^{V_{\text{maximum}}} I(V)dV}{\Delta V}}{v} \tag{5.2}$$

Furthermore, CV loops show both charge and discharge steps. But there are many research, suggest use whole CV loop to calculate supercapacitor performance. Then, the specific capacitance of only discharge state will be

$$C = \frac{I}{v} = \frac{\frac{\int_{V_{\text{minimum}}}^{V_{\text{maximum}}} I(V)dV}{\Delta V}}{2v} \tag{5.3}$$

$$C_{\text{cell}} = \frac{I}{v} = \frac{\int_{V_{\text{minimum}}}^{V_{\text{maximum}}} I(V)dV}{2v \cdot \Delta V} \tag{5.4}$$

To check unit, A/sV is equalvalent with C/V or F. Then, C cell is in F for coin cell supercapacitor is evaluated by using this equation:

$$C_{\text{cell}} = 4\frac{\int_{V_{\text{minimum}}}^{V_{\text{maximum}}} I(V)dV}{2v \cdot \Delta V} = 2\frac{\int_{V_{\text{minimum}}}^{V_{\text{maximum}}} I(V)dV}{v \cdot \Delta V} = 2\frac{\text{Area of CV curve}}{(\text{scan rate}) \cdot (\text{potential window})} \tag{5.5}$$

where Ccell is the specific capacitance of materials in farad, ΔV is potential window of discharge step in volt (V), I is constant current in ampere (A), and $dt_{\text{discharge}}$ is the discharge time in second (s), is scan rate in volt per second (V/s), V_{maximum}-V_{minimum} is potential window in volt (V), and the integration of the resulting cyclic voltammograms, the accumulated charge (I) as a function of potential (V) can be obtained as $\int_{V_{\text{minimum}}}^{V_{\text{maximum}}} I(V)dV$. Then, the whole curve is recommended to for use as in Volt Ampere.

From table 5.3, The specific capacitance of the V_2O_5 thin films at O_2/Ar flow rate of 1/20, 2/20, 3/20, 4/20, 5/20, and 6/20 (in sccm unit) were estimated to be 16.1, 11.3, 19.8, 7.6, 14.1, and 10.6 mF, respectively. The highest specific capacitance is 19.8 mF was obtained from CV curves with V_2O_5 thin films which coat by RF reactive magnetron sputtering at O_2/Ar = 3/20 which was higher than other condition.
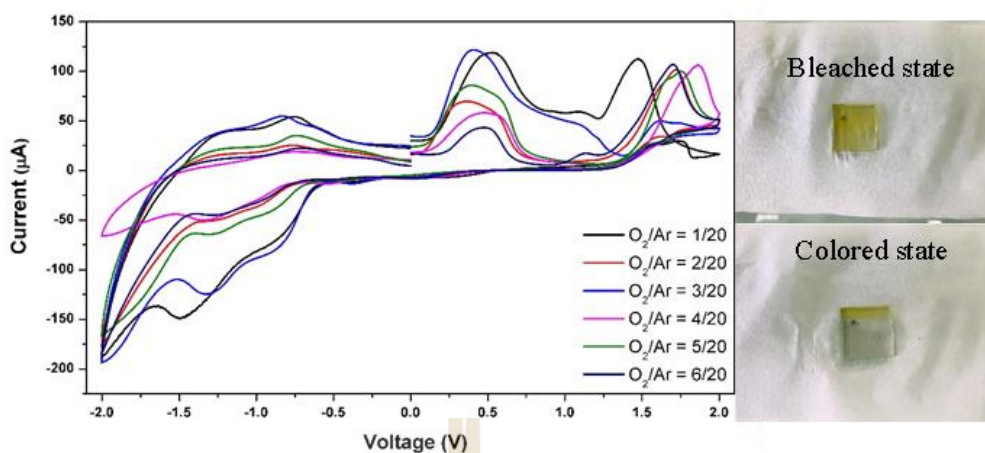
Figure 5.7 (left) Cyclic voltammograms of electrodeposited vanadium oxide films for Na insertion/extraction. (right) These processes lead to film coloration [dark yellow→transparent→ yellow].
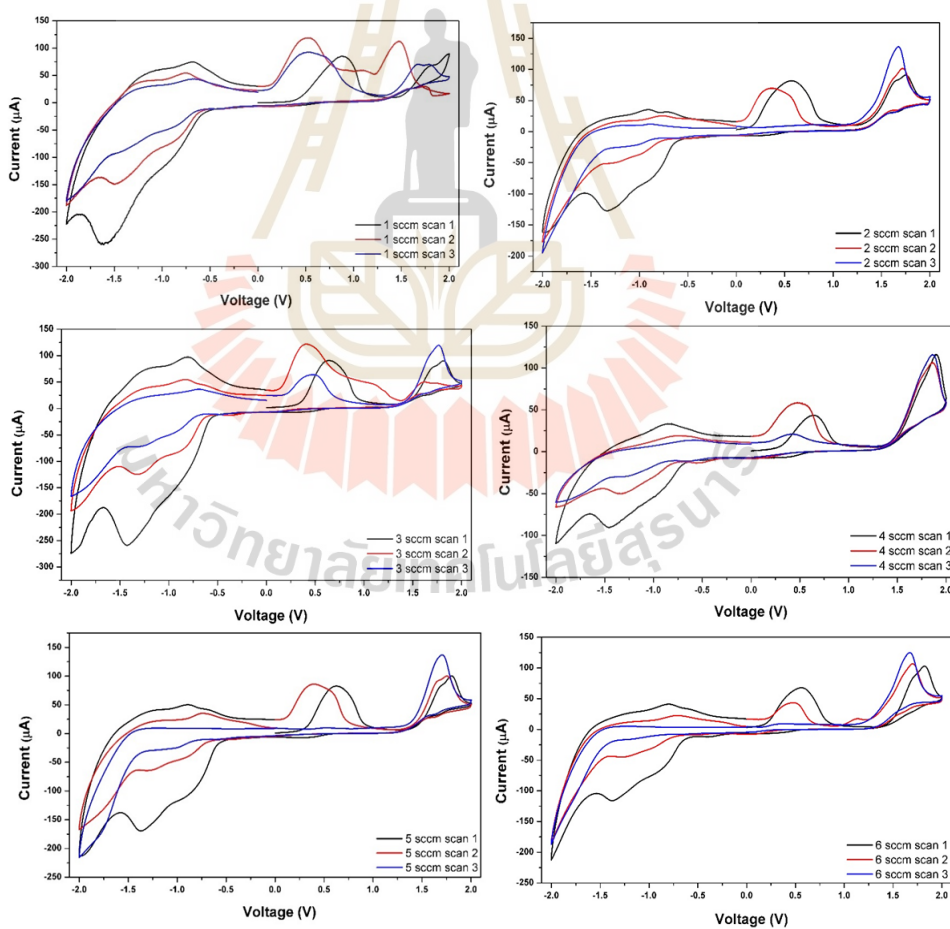
Figure 5.8 Cyclic voltammograms of electrodeposited vanadium oxide thin films at the O₂/Ar flow rate of 1/20, 2/20, 4/20, 5/20, and 6/20 (in sccm unit) for Na insertion/extraction.

Table 5.3 The table of specific capacitance of vanadium oxide thin films at different O_2/Ar flow rate.

O_2/Ar flow rate (in sccm unit)	Specific capacitance (mF)
1/20	16.1
2/20	11.3
3/20	19.8
4/20	7.6
5/20	14.1
6/20	10.6

In XAS (XANES) at V K-edge was performed during the coloration process upon the electrochemical reaction to gain insights into the effects of Na insertion/extraction on the oxidation states of vanadium, as well as the local atomic structure of the V_2O_5 thin films. Thus, the XAS spectrum of a V_2O_5 films deposited for O_2/Ar flow rate of 1/20, 2/20, 3/20, 4/20, 5/20, and 6/20 (in sccm unit) are shown in Figure 5.9 ((a)-(f)) and the corresponding first derivatives ((g)-(l)) with VO_2, V_2O_3, V_2O_5 and V-foil standard samples. The insets compare the edge peak intensities during Na-insertion processes. From figure 5.9 and figure 5.10, two major changes under bias potential from 0 to -1.8 V caused by Na-ion intercalation in the spectral features, which were observed in the edge region, were indicated as follows: a shift of edge peak position to the lower energy and a decrease in edge peaks. The shift to low energy was attributed to the decreased oxidation state of metal ions because of Na-ion intercalation, which can be conceptually caused by the reduced effective nuclear charge of the metal ions with decreased oxidation state. The energy of edge peak clearly decreased for the bias potentials from 0 to -0.8 to -1.8 V, suggesting that the local structure around the V atom became more symmetrical with Na-ion intercalation. However, extracting sodium under a bias potential from -1.8 to +1.8 V changes the color of the film from yellow to transparent (colored state) and transparent to yellow (bleached state). At 0.8 V the edge peak of the V K-edge shifts to high energy when the film was oxidized, and partial V^{3+}, V^{4+} ions change into V^{5+}. The remaining V^{4+} ions reduced to V^{5+} at 1.8 V (from Linear combination fit in table 5.4). The positive shift in the V K-edge indicates that the

average oxidation state of V increased because of an increase in the attractive potential of the nucleus. Additionally, the increase in the pre-edge peak area corresponds to the gradually decreasing sodium content.
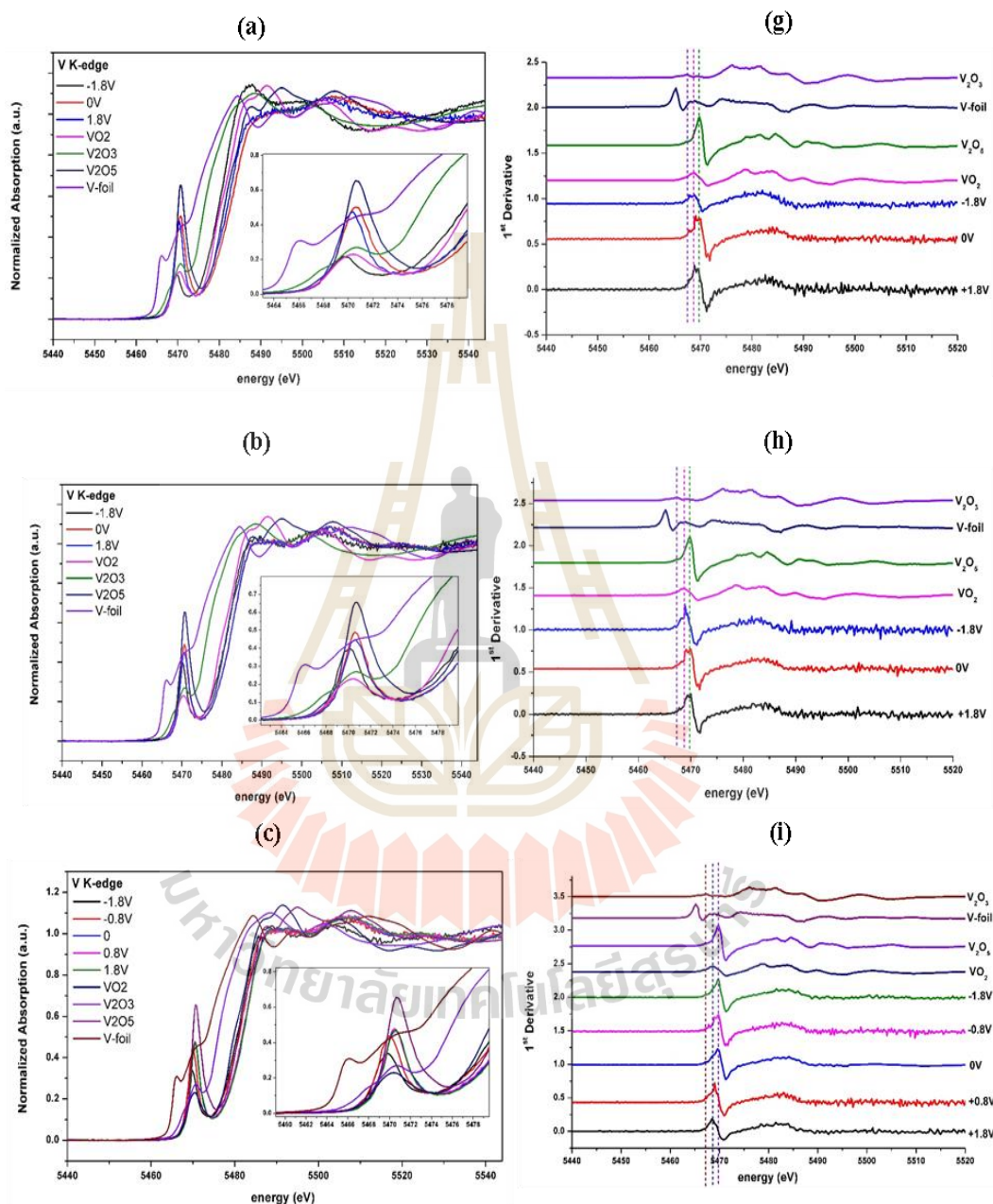
Figure 5.9 (Continuous) Normalized V K-edge XANES spectra ((a)-(f) and insets display the enlargements of pre-peak intensities during Na-insertion) and the corresponding first derivatives ((g)-(l)) of vanadium electrode at applied potentials in the order of -1.8, 0, and 1.8 V of the O_2/Ar flow rate of 1/20, 2/20, 4/20, 5/20, and 6/20 (in sccm unit) with VO_2, V_2O_3, V_2O_5 and V-foil standard samples.
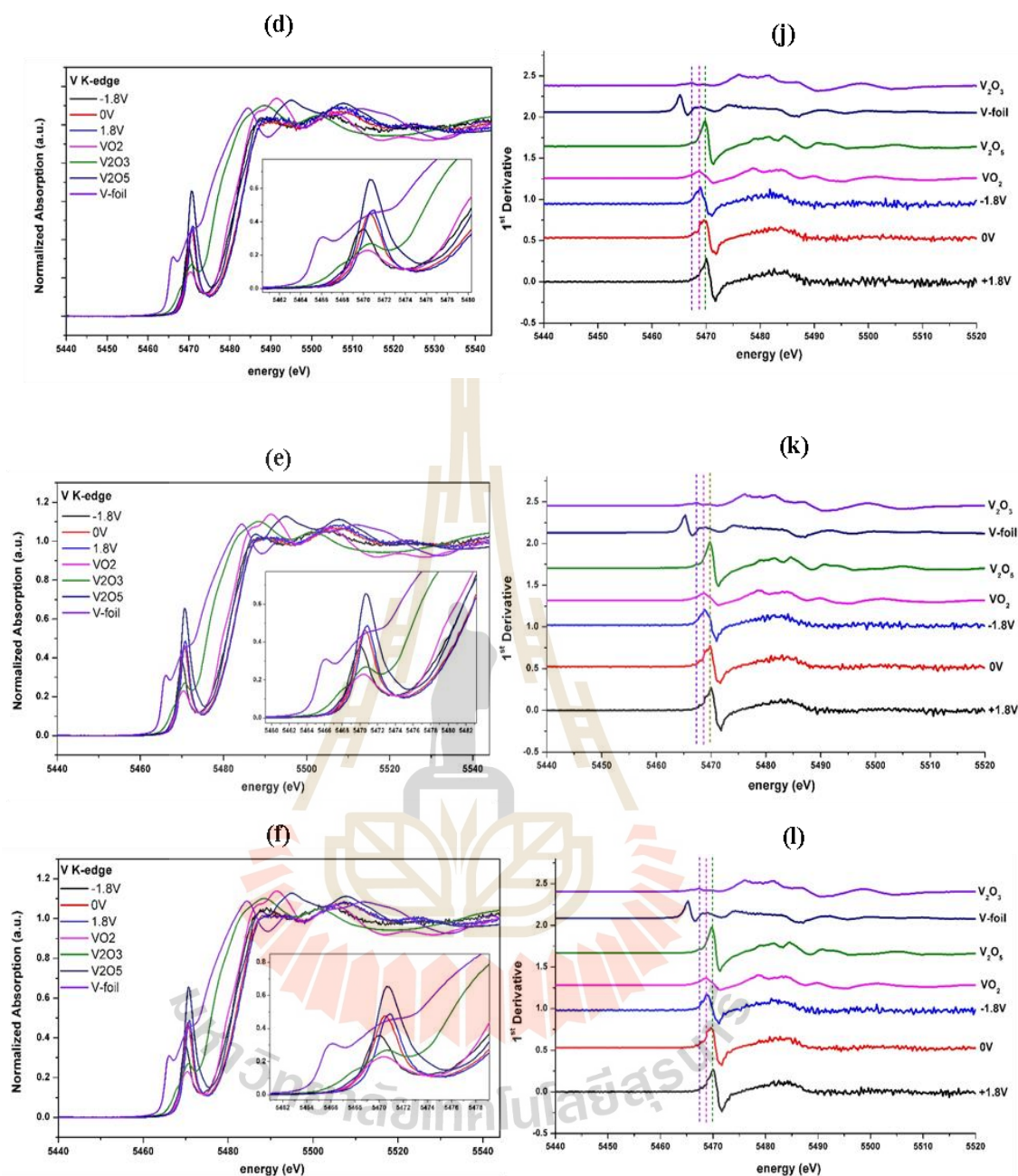
Figure 5.9 (Continuous) Normalized V K-edge XANES spectra ((a)-(f) and insets display the enlargements of pre-peak intensities during Na-insertion) and the corresponding first derivatives ((g)-(l)) of vanadium electrode at applied potentials in the order of -1.8, 0, and 1.8 V of the O_2/Ar flow rate of 1/20, 2/20, 4/20, 5/20, and 6/20 (in sccm unit) with VO_2, V_2O_3, V_2O_5, and V-foil standard samples.
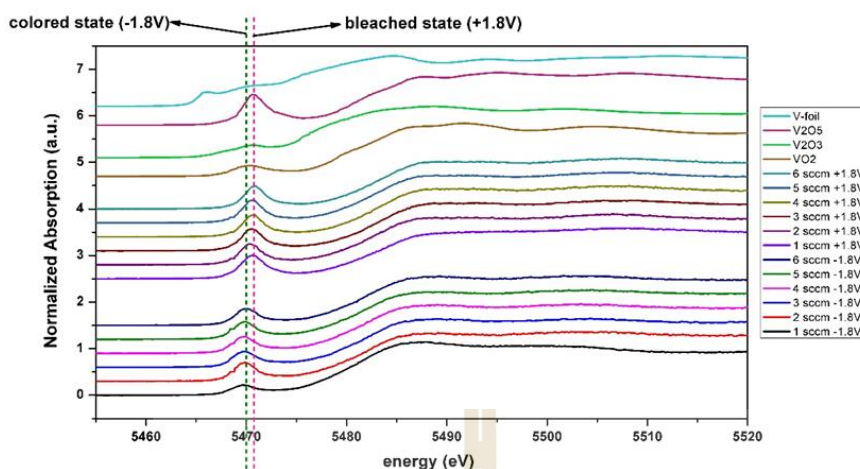
Figure 5.10 XANES spectra at V K-edge for the O_2/Ar flow rate of 1/20, 2/20, 3/20, 4/20, 5/20, and 6/20 (in sccm unit) at applied potentials in the order of -1.8, 0, and 1.8 V, with VO_2, V_2O_3, V_2O_5, and V-foil standard samples.

Table 5.4 (Continuous) Linear combination fit of %VO_2, %V_2O_5, %V_2O_3 and oxidation state at applied potentials in the order of -1.8, 0, and 1.8 V of vanadium oxide thin films at different O_2/Ar flow rates (in sccm unit) was applied potentials in the order of -1.8, -0.8, 0, 0.8, and 1.8 V.

O_2/Ar flow rate	applied potentials	%VO_2	% V_2O_5	%V_2O_3	E_0 (eV)	Oxidation state
1/20 (in sccm unit)	-1.8V	64	0	36	5468.45	3.56
	0V	41	58	1	5469.54	4.75
	+1.8V	22	77	1	5469.27	4.45
2/20 (in sccm unit)	-1.8V	61	32	7	5468.85	3.99
	0V	19	77	6	5469.63	4.85
	+1.8V	17	75	8	5469.67	4.89
3/20 (in sccm unit)	-1.8V	89	5	6	5468.51	3.62
	-0.8V	68	32	0	5469.04	4.20
	0V	12	81	7	5469.72	4.95
	+0.8V	15	77	8	5469.69	4.91
	+1.8V	13	79	8	5469.72	4.95

Table 5.4 (Continuous) Linear combination fit of %VO$_2$, %V$_2$O$_5$, %V$_2$O$_3$ and oxidation state at applied potentials in the order of -1.8, 0, and 1.8 V of vanadium oxide thin films at different O$_2$/Ar flow rates (in sccm unit) was applied potentials in the order of -1.8, -0.8, 0, 0.8 and 1.8 V.

O$_2$/Ar flow rate	applied potentials	%VO$_2$	% V$_2$O$_5$	%V$_2$O$_3$	E$_0$ (eV)	Oxidation state
4/20 (in sccm unit)	-1.8V	73	18	9	5468.82	3.96
	0V	19	73	8	5469.56	4.77
	+1.8V	5	82	13	5470.02	5.28
5/20 (in sccm unit)	-1.8V	62	28	10	5468.71	3.84
	0V	18	75	7	5469.79	5.03
	+1.8V	6	83	11	5470.02	5.28
6/20 (in sccm unit)	-1.8V	61	25	14	5468.8	3.94
	0V	17	76	7	5469.73	4.96
	+1.8V	3	84	13	5470.02	5.28
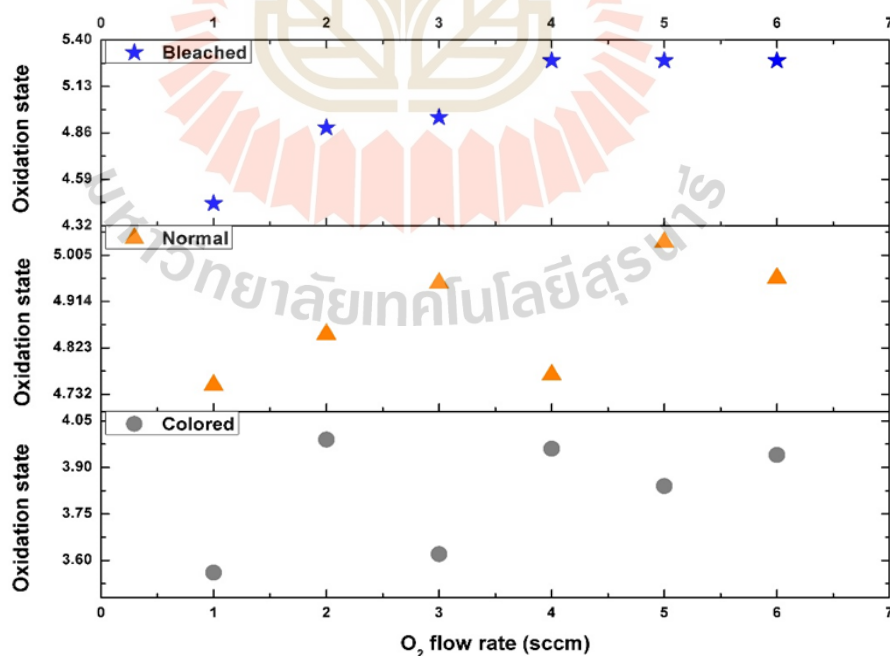
Figure 5.11 The oxidation state of the colored (-1.8 V), normal (0 V) and bleached (1.8 V) of vanadium oxide thin films at different O$_2$/Ar flow rates have changed as a result of the calculation.

5.2.2 Optical contrast

Chananonnawathorn (Chananonnawathorn, 2014) was studied in efficiency of electrochromic device (The transmittance variance) which was generated from delta of $\%T_{bleached}$ (percentage of transmittion at bleached state) and $\%T_{colored}$ (percentage of transmittion at colored state). The transmittance variance (ΔT) is defined by

$$\Delta\%T = \%T_{bleached} - \%T_{colored} \tag{5.6}$$

$$\%T_{avg} = \frac{\sum_{\lambda_a}^{\lambda_a} T(\lambda)E(\lambda)}{\sum_{\lambda_a}^{\lambda_b} E(\lambda)} \tag{5.7}$$

where $T(\lambda)$ is percentage of transmittion

$E(\lambda)$ is relative solar energy (The data of relative solar energy is shown in table 5.5)

So, $\sum_{\lambda_a}^{\lambda_b} E(\lambda) = 100$ because this data were calculated from average visible light and λ_a = 380 nm, λ_b = 780 nm.

In this work, efficiency of electrochromic device of the vanadium oxide thin films at the O_2/Ar flow rate of 1/20, 2/20, 4/20, 5/20, and 6/20 (in sccm unit) were compared with $\Delta\%T$ and a high value indicates of $\Delta\%T$ that the resulting film exhibits excellent electrochromic characteristics. (Chananonnawathorn, 2014).

Table 5.5 (Continuous) The table of relative solar energy at wavelength of visible light.

Wavelength(nm)	Energy (W/m^2 μm)	Relative Energy
380	513.14	2.06
400	749.95	3.00
420	1003.24	4.02
440	1136.67	4.55
460	1387.34	5.56
480	1456.28	5.83
500	1425.25	5.71

Table 5.5 (Continuous) The table of relative solar energy at wavelength of visible light.

Wavelength(nm)	Energy (W/m² µm)	Relative Energy
520	1373.08	5.50
540	1362.83	5.46
560	1316.44	5.27
580	1347.84	5.40
600	1324.65	5.30
620	1310.65	5.25
640	1298.73	5.20
660	1278.77	5.12
680	1249.75	5.00
700	1220.04	4.89
720	1180.45	4.73
740	1140.92	4.57
760	828.63	3.32
780	1065.90	4.27

The electrochromic performance of the of the vanadium oxide thin films at the O2/Ar flow rate of 1/20, 2/20, 4/20, 5/20, and 6/20 (in sccm unit) were characterized by optical contrast ($\Delta\%T$) as a function of Na^+ insertion and extraction in a 0.154 M NaCl electrolyte at different O_2/Ar flow rates. Each V_2O_5 thin films were sputtered onto ITO glass substrate at the O_2/Ar flow rate of 1/20, 2/20, 4/20, 5/20, and 6/20 (in sccm

unit). Figure 5.12 showed the transmittance spectra of bleached and colored of V_2O_5 thin films were plotted as a function of wavelength at O_2/Ar flow rates of (a) 1/20, (b) 2/20, (c) 3/20, (d) 4/20, (e) 5/20, and (f) 6/20 (in sccm unit). The important efficiency of electrochromic device parameters such as short %$T_{bleached}$ (percentage of transmittion at bleached state) and %$T_{colored}$ (percentage of transmittion at colored state) and optical contrast (Δ%T) which determined from the %T vs wavelength were shown in table 5.6. The optical contrast (Δ%T) of V_2O_5 thin films at the difference in transmittance of bleached and colored of V_2O_5 thin films were 0.97%, 15.20%, 22.17%, 18.54%, 19.11%, and 2.55% at O_2/Ar flow rates of 1/20, 2/20, 3/20, 4/20, 5/20, and 6/20 (in sccm unit), respectively. The highest optical contrast (Δ%T) is 22.17% was obtained from electrochromic device with V_2O_5 thin film which coat by RF reactive magnetron sputtering at O_2/Ar = 3/20 (in sccm unit) which was higher than the other conditions. So, at O_2/Ar = 3/20 (in sccm unit) has good performance for electrochromic deviece (compaired with other conditions).
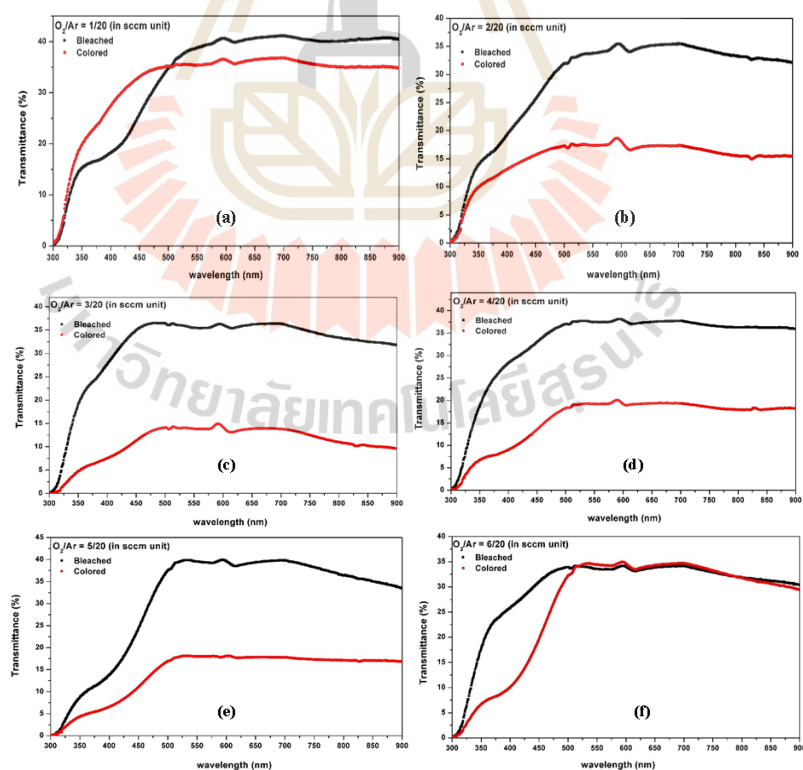
Figure 5.12 The transmittance spectra of bleached and colored of V_2O_5 thin films were plotted as a function of wavelength at O_2/Ar flow rates of (a) 1/20, (b) 2/20, (c) 3/20, (d) 4/20, (e) 5/20, and (f) 6/20 (in sccm unit).

Table 5.6 The table of $\%T_{bleached}$ and $\%T_{colored}$ of vanadium oxide thin films at different O_2/Ar flow rate.

O_2/Ar flow rate (in sccm unit)	$\%T_{bleached}$	$\%T_{colored}$	$\Delta\%T$
1/20	35.80	34.83	0.97
2/20	31.85	16.65	15.20
3/20	35.00	12.83	22.17
4/20	36.03	17.49	18.54
5/20	35.03	15.92	19.11
6/20	32.65	30.10	2.55
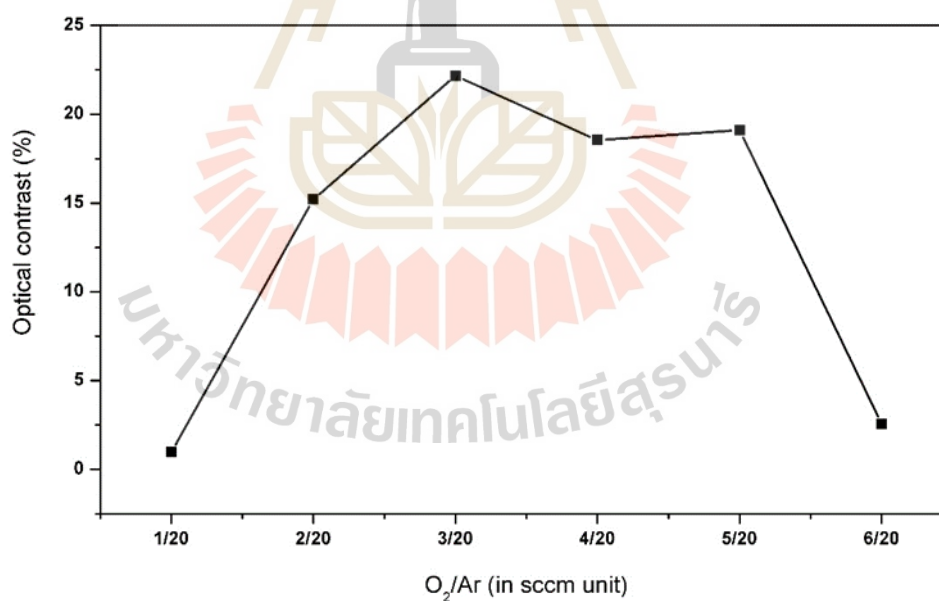
Figure 5.13 The optical contrast ($\Delta\%T$) of vanadium oxide thin films was plotted as a function of Na^+ insertion and extraction at various O_2/Ar flow rates.

CHAPTER VI

LOCAL STRUCTURE AND ELECTROCHROMIC PROPERTIES OF

TUNGSTEN OXIDE (WO₃) FILMS

6.1   Experiment

6.1.1 WO₃ thin films preparation (sample from NECTEC)

The tungsten oxide thin films were prepared by tungsten metal target (3 inches) 99.9% of purity, from Kurt J. Lesker. The target was placed at a distance of 6 cm from the substrates. The deposition conditions were fixed with the thickness, based pressure at 5.0×10^{-6} mbar, operating pressure at 6.0×10^{-3} mbar, rotated substract at 10 rpm, and Ar: O_2 flow rate of 80:40 (in sccm unit), while the DC power was by 100 W (sputtering time at 12.30 minute), 150 W (sputtering time at 7.13 minute), 200 W (sputtering time at 4.45 minute) and all samples were annealed at 400 ^{o}C. The tungsten oxide thin films were deposited on ITO glass and Si (100) substrates to obtain the morphology, phase formation, local structure and electrochromic properties.

6.1.2 Thin films characterizations

Crystal structure was investigated by the x-ray diffraction spectroscopy (XRD; BRUKER, D8 ADVANCE) with Cu Kα radiation). The optical properties were investigated by UV-Visible spectroscopy (Varian model Carry 50). And the local structure was characterized by synchrotron-based XANES and EXAFS spectra at the SUT-NANOTEC-SLRI XAS Beamline (BL5.2) at the Synchrotron Light Research Institute (Public Organization), Thailand.

Table 6.1 The sputtering condition of WO_3 thin films.

Target	W-metal target (3 inches 99.9% of purity, from Kurt J. Lesker)
RF power	100, 150, and 200 W
Base pressure	5×10^{-6} mbar
Operating pressure (O_2+Ar flow rate)	6×10^{-3} mbar
Distance of sample holder from target	6 cm
Sputtering time	12.30, 7.13, and4.45 minutes
Ar: O_2 flow rate	80:40 (in sccm unit)
Substrate	Si (100), ITO glass
Annealing	400 °C
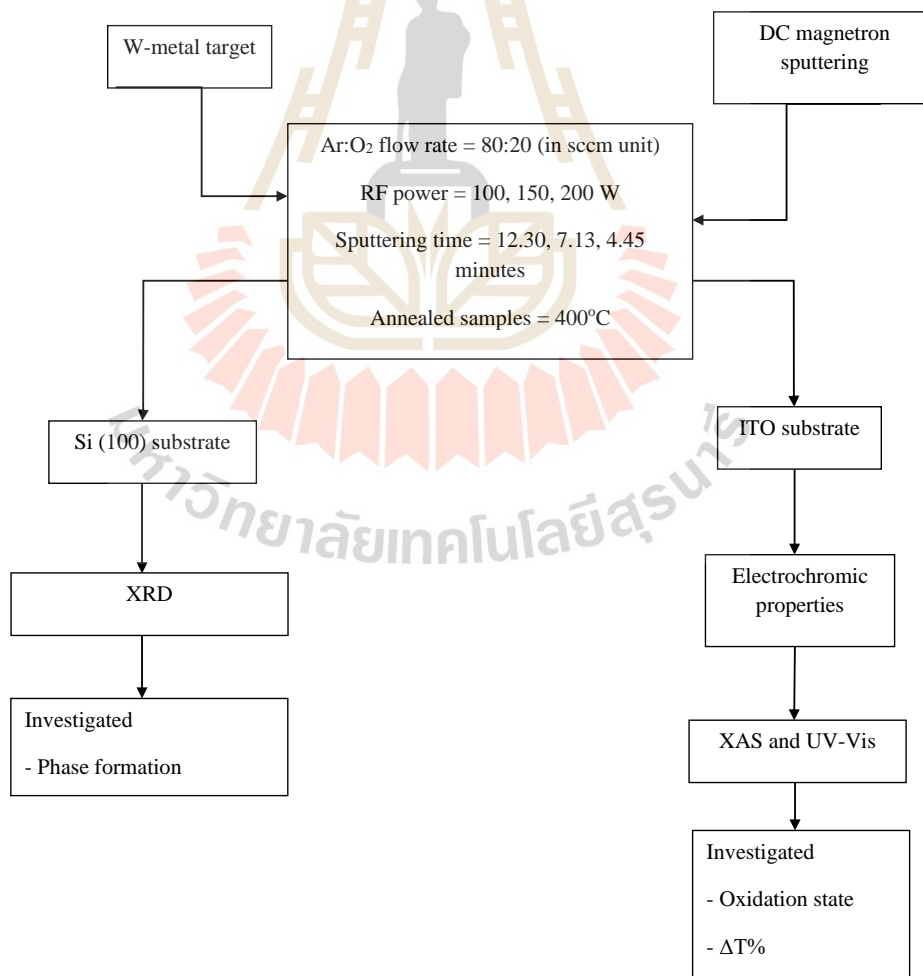
Figure 6.1 The process of WO_3 thin films for DC magnetron sputtering technique.

6.1.3 Procedure for Electrochromic properties (XAS and UV-Vis)

The potassium-ion insertion/extraction and optical properties of the WO_3 thin films at Ar: O_2 of 80:40 (in sccm unit) was investigated in 0.1 M KOH solution and using the two-electrode system, in which Cu plate was used as the counter. Potential window was performed between −1.4 and +1.4 V for XAS and UV-Vis.

Table 6.2 The sputtering condition of WO_3 thin films.

Target	W-metal target (3 inches 99.9% of purity, from Kurt J. Lesker)
RF power	100, 150, and 200 W
Base pressure	5×10^{-6} mbar
Operating pressure (O_2+Ar flow rate)	6×10^{-3} mbar
Distance of sample holder from target	6 cm
Sputtering time	12.30, 7.13, and 4.45 minutes
Ar: O_2 flow rate	80:40 (in sccm unit)
Annealing	400 °C
Substrate	ITO glass
Electrolyte	KOH
Counter electrode	Cu plate
Potential window	-1.4 V to +1.4 V
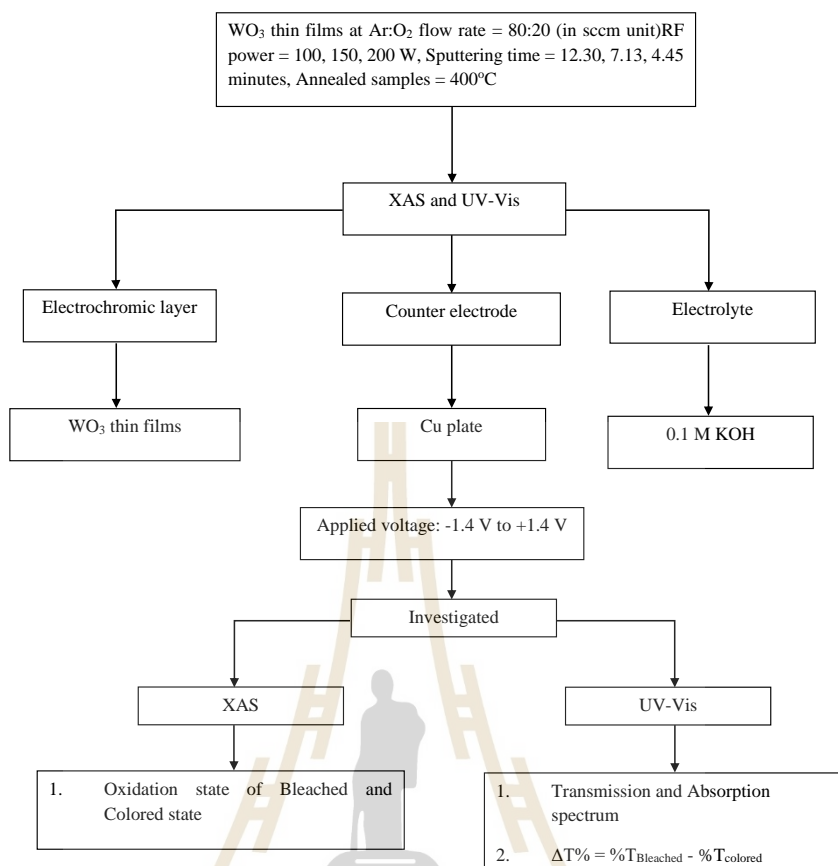
Figure 6.2 Flow chart of the of WO₃ thin films for measurement the XAS and UV-Vis.
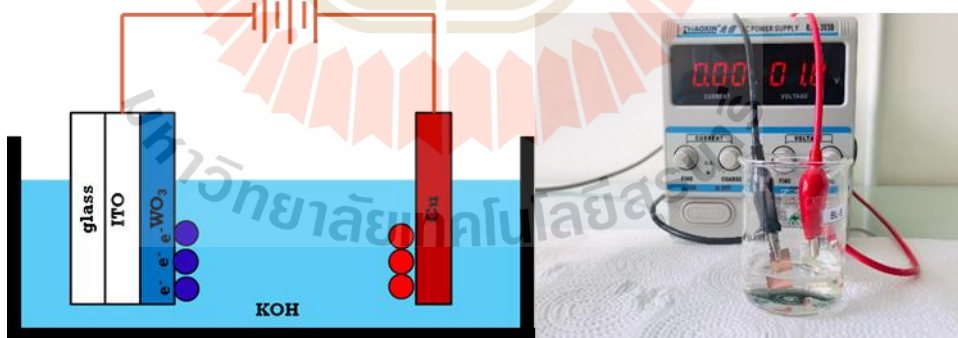
Figure 6.3 Schematic diagram of electrochromic structures and K insertion into WO₃ structure (left) and the photo of two-electrode of electrochromic cell for XAS and UV-vis measurement.
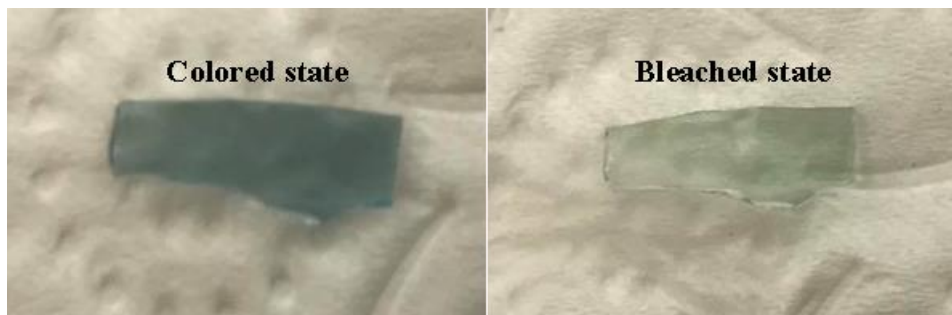
Figure 6.4 The photos exhibit the color changes of the film.

6.2 Results and discussion

6.2.1 Phase formation of WO$_3$ thin films
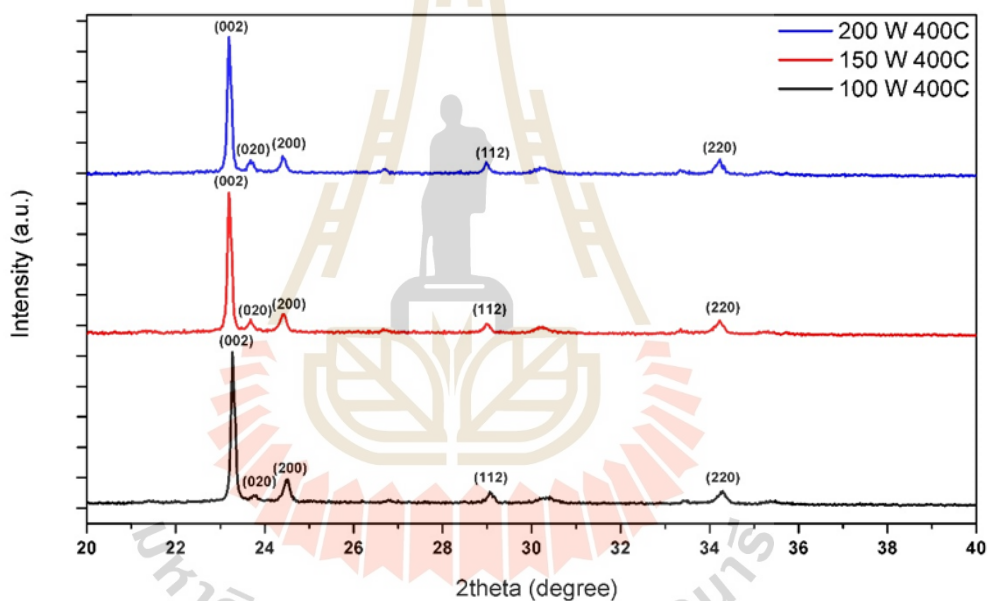
Figure 6.5 X-ray diffraction patterns of tungsten oxide thin films at the ratio of Ar: O$_2$ flow rate of 80: 40 (in sccm unit) and DC power of 100, 150, and 200W and all samples were annealed at 400 °C.

For investigating the crystal structures of tungsten oxide thin films, all thin-film samples fabricated at the ratio of Ar:O$_2$ flow rate of 80:40 (in sccm unit) and DC power of 100, 150, and 200W and all samples were annealed at 400 °C were characterized by the X-ray diffraction technique (XRD) and their diffraction patterns were shown in figure 6.5. The XRD patterns could be indexed to WO$_3$. At the ratio of Ar:O$_2$ flow rate of 80:40 (in sccm unit) and DC power of 100, 150, and 200W and all samples were

annealed at 400 °C in a 2θ range of 20°-40°, the diffraction peak at 23.194°, 23.69°, 24.4°, 28.98°, and 34.23° corresponding to the (002), (020), (200), (112), and (220) plane of WO$_3$ lattice parameters of a=7.3013Å, b=7.539Å, c=7.6893Å, and β=90.893° was detected (Wang et al., 2018). The XRD results of all thin-film samples would be further confirmed by the XAS technique.

6.2.2 Optical properties

The absorbance and transmittance spectra of tungsten oxide thin films on ITO glass substrate with the ratio of Ar:O$_2$ flow rate of 80:40 (in sccm unit) and DC power of 100, 150, and 200W and all samples were annealed at 400 °C were shown in figure 6.6. The absorption edges were clearly observed at around 410-430 nm which was corresponded to the energy band gap of the WO$_3$ thin films.
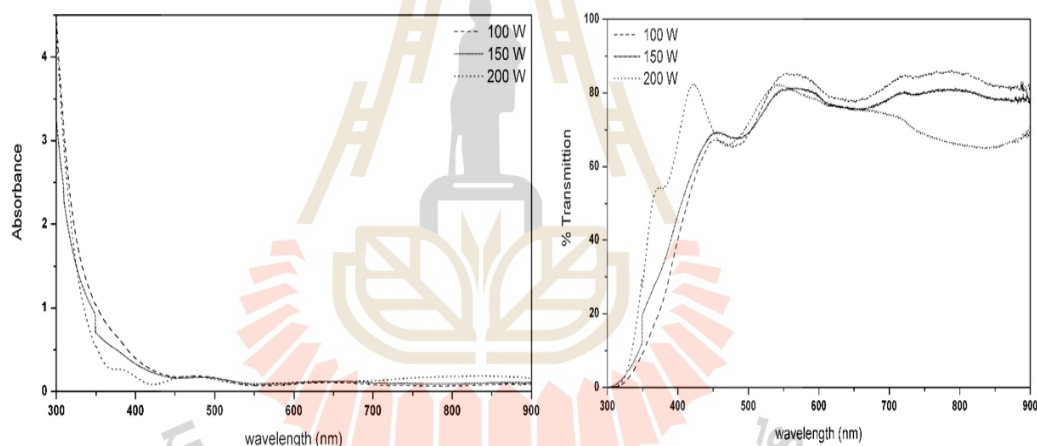
Figure 6.6 The absorbance (left) and transmittance (Right) spectra of tungsten oxide thin films on ITO glass substrate with the ratio of Ar:O$_2$ flow rate of 80:40 (in sccm unit) and DC power of 100, 150, and 200W and all samples were annealed at 400 °C.

The value of energy band gap was extracted from transmittance spectra by plotting $(\alpha h\nu)^2$ vs $h\nu$ and extrapolating the linear portion of the curve to zero. From table 6.3, The energy band gap of tungsten oxide thin films on ITO glass substrate with the ratio of Ar:O$_2$ flow rate of 80:40 (in sccm unit) and DC power of 100, 150, and 200 W and all samples were annealed at 400 °C were estimated to be 2.88, 2.90, and 3.00 eV, respectively. Therefore, the energy band diagram can be drawn as an inset of figure 6.7.
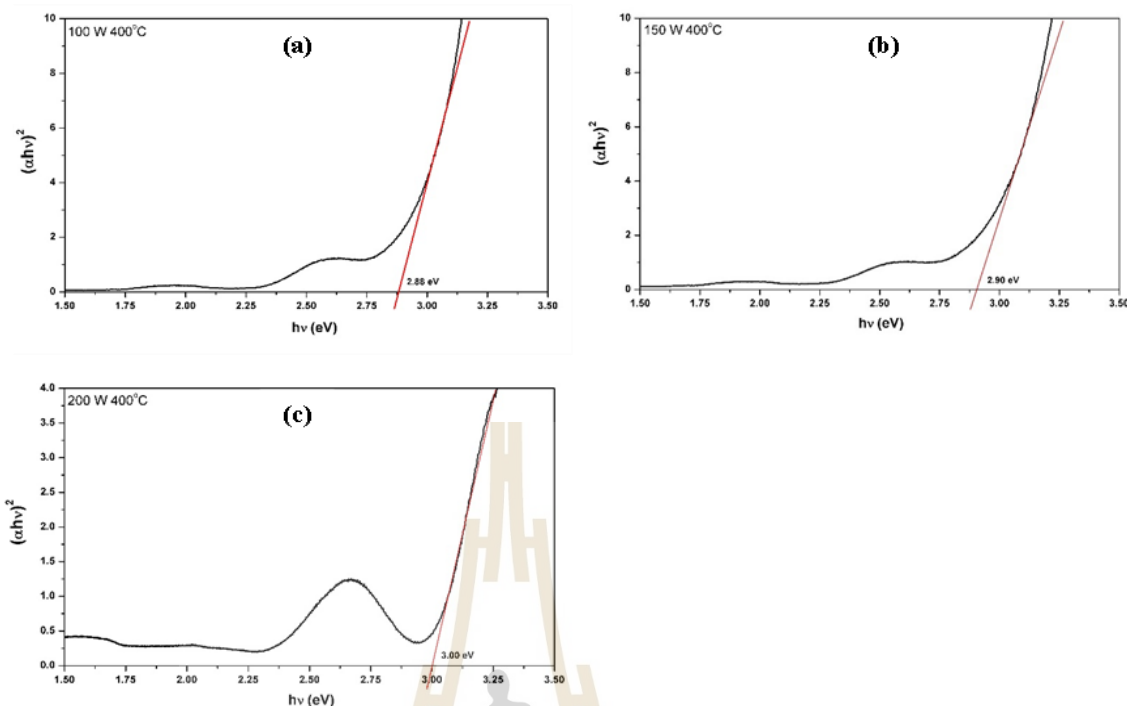
Figure 6.7 Relation between $(\alpha h\nu)^2$ and $h\nu$ of tungsten oxide thin films on ITO glass substrate with the ratio of Ar:O$_2$ flow rate of 80:40 (in sccm unit) and DC power of (a) 100, (b) 150, and (c) 200W and all samples were annealed at 400 °C.

Table 6.3 The table of energy band gap of WO$_3$ at all conditions.

DC power (W)	Energy gap (eV)
100	2.88
150	2.90
200	3.00

6.2.3 XAS and electrochromic properties

The electrochemical behavior of the WO$_3$ material was investigated using the two-electrode system, in which Cu plate were used as the counter electrodes. XAS and UV-vis were adopted to investigate the potassium (K) insertion/extraction behavior in 0.1 M KOH. Figure 6.8 and 6.10 shows typical xanes spectrum and % transmittance of WO$_3$ electrodes with the ratio of Ar:O$_2$ flow rate of 80:40 (in sccm unit) and DC power of 100, 150, and 200W and all samples were annealed at 400 °C in the potential range of −1.4 to 1.4 V.

A majority tungsten oxide phase can be used to study the electronic structure and local structure around W atoms using the XAS technique. Figure 6.8 showed the normalized W L_3-edge XANES spectrum of ratio of Ar:O_2 flow rate of 80:40 (in sccm unit) and DC power of (a) 100, (b) 150, and (c) 200W and all samples were annealed at 400 $^\circ$C, W-foil, and WO_3 standard samples. The characteristic absorption edge of W existed at 10207 eV and white line peak of W existed at 10209 eV (to compared with all condition), which corresponds to the energy required to eject a core electron from a tungsten atom. The white line peak of near 10209-10213 eV deconvoluted from XANES showed that the films contained the oxidation state of 6+ (W^{6+}) at bleached state (+1.4 V) and as-deposited state (0 V) and the other. Since the deposited WO_3 was a mix of tungsten oxide phases. The white line peaks observed in XANES spectra refered to the electronic 2p$\longrightarrow$5d transitions, whereas the white line peaks around 10211 eV assumed the oxidation state of 5+ (W^{5+}) at colored state (-1.4 V) and confirmed with EXAFS in the next section. The insets compare the edge peak intensities during K-insertion processes. From figure 6.8 and figure 6.10, two major changes under bias potential from 0 to -1.4 V caused by K-ion intercalation in the spectral features, which were observed in the white line peak region, were indicated as follows: a shift of white line peak position to the lower energy. The shift to low energy was attributed to the decreased oxidation state of metal ions because of K-ion intercalation, which can be conceptually caused by the reduced effective nuclear charge of the metal ions with decreased oxidation state. The energy of white line peak clearly decreased for the bias potentials from 0 to −1.4 V, suggesting that the local structure around the W atom became more symmetrical with K-ion intercalation. However, extracting potassium under a bias potential from −1.4 to +1.4 V changes the color of the film from transparent to blue (colored state) and blue to transparent (bleached state). The remaining W^{5+} ions reduced to W^{6+} at +1.4 V (Ho et al., 2013). The positive shift in the W L_3-edge indicates that the average oxidation state of W increased because of an increase in the attractive potential of the nucleus. Additionally, the increase in the energy of white line peak area corresponds to the gradually decreasing potassium content. So, the effect of K^+ insertion/extraction in WO_3 structure can be expressed by $WO_3 + xK^+ + xe^- \longleftrightarrow M_xW_2O_5$, which is accompanied by color changes [trasparent$\longrightarrow$blue

(colored state) and blue→transparent (bleached state)] which were shown in figure 6.9. As mentioned previously, the XANES results were used for the study of oxidation state of tungsten oxide thin films at all conditions. The plots showed that, tungsten thin films contained the 2p→5d transition peak (around 10209 eV) referred to W^{6+} for bleached and as-deposited state and the other around 10211 eV referred to W^{5+} for colored state at all conditions. The sole XANES results were not able to provide deeply information on the local structure of tungsten oxide. The white line peak near 10209-10213 eV (Wu et al., 2004) could be due to a mixture of several coordinations or a rather large distribution of crystal fields around tungsten (Ravel and Newville, 2005). This suggests a significant change in W local structure especially for coordinated oxygen atoms surrounding W atom. This would be further discussed in the EXAFS section.
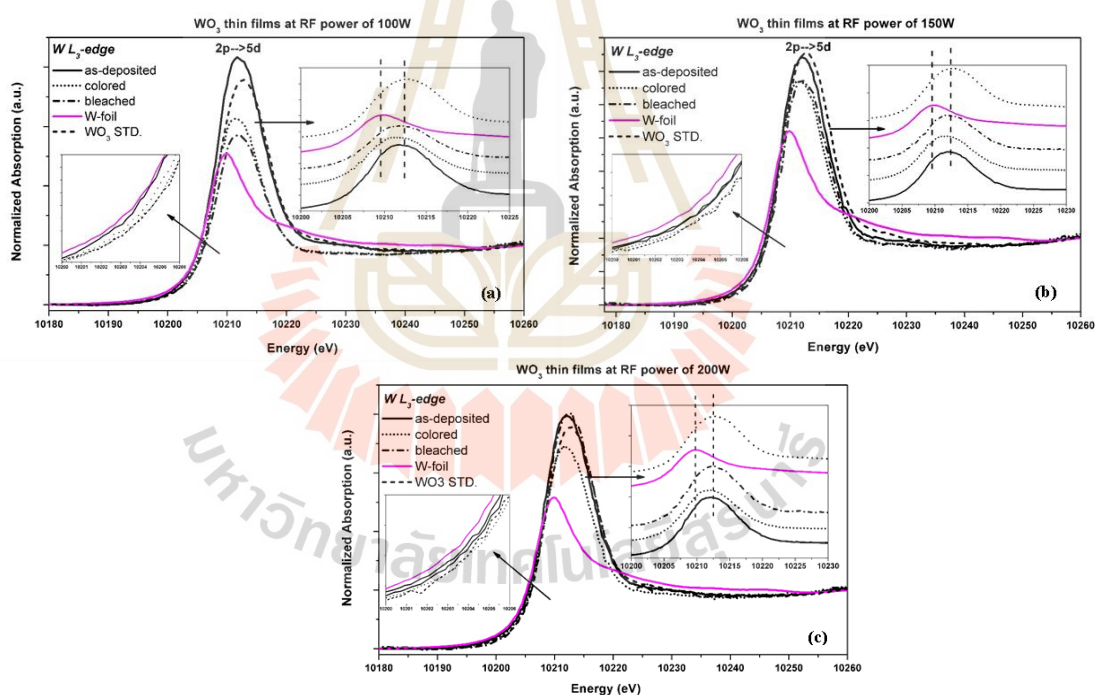
Figure 6.8 Normalized W L_3-edge XANES spectra and insets display the enlargements of white line peak intensities during K-insertion) of tungsten electrode at applied potentials in the order of -1.4 (colored state), 0 (as-deposited state), and +1.4 (bleached state) V at the ratio of Ar:O_2 flow rate of 80:40 (in sccm unit), DC power of (a) 100, (b) 150, and (c) 200 W and sample were annealed at 400 °C with WO_3 and W-foil standard samples.
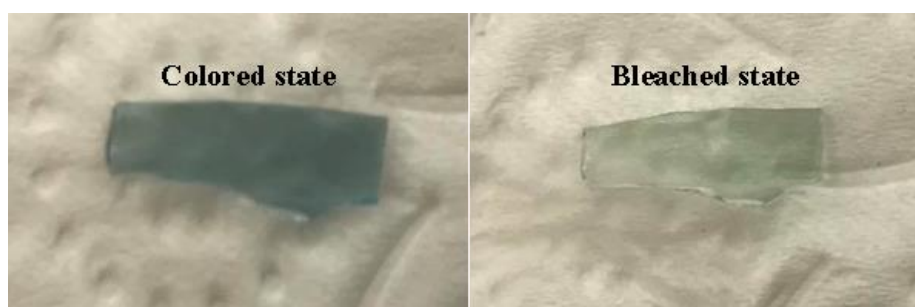
Figure 6.9 The photos exhibit the color changes of the film.
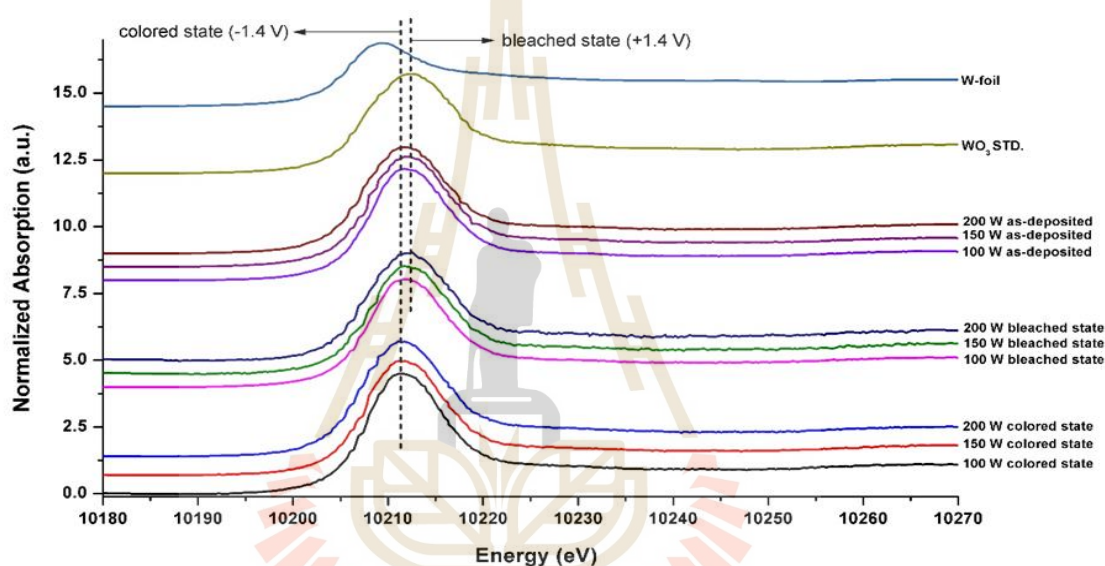
Figure 6.10 XANES spectra at W L_3-edge for the tungsten electrode at applied potentials in the order of -1.4 (colored state), 0 (as-deposited state), and +1.4 (bleached state) V at the ratio of Ar:O_2 flow rate of 80:40 (in sccm unit), DC power of 100, 150, and 200 W and sample were annealed at 400 $^{\circ}$C with WO_3 and W-foil standard samples.

In order to understand the local environment of W atoms in the structure, the EXAFS spectra were intensively analyzed and fitted using Athena and Artemis programs as implement in the IFEFFIT packages (Al-Mansoori et al., 2015; Wong et al., 1984). Figure 6.11 shows Fourier transform (FT) of EXAFS $k^3\chi$ data at the W L_3-edge from k = 3 to 10 Å^{-1}. The inset of figure 6.11 shows the R-space of the films in as-deposited, bleached and colored state. It demonstrates that for bleached films, the general line shapes are identical to each other irrespective of the thickness of the film and are

more close to monoclinic WO_3 (model from material project) (Rodella and Mastelaro, 2003). On the contrary, for the films in colored state the general line shapes are similar to the mixed of tetragonal WO_3, triclinic $K_2W_2O_5$ and cubic KWO_3 (model from material project). This finding is consistent with the X-ray absorption near-edge structure results. In the figure of all conditions, the general line shapes and radial distribution of the FT spectra of the films in bleached and colored states are also very different and provide a direct evidence for the change in W/O bond length. Two major changes under bias potential from 0 to −1.4 V caused by K-ion intercalation in the spectral features, which were observed in the R-space region, were indicated as follows: the increased of R-space position. The shift to more R-space was attributed to the structure of WO_3 was distorted by K-ion insertion. The R-space clearly increased for the bias potentials from 0 to −1.4 V, suggesting that the local structure around the W atom became more symmetrical with K-ion intercalation. However, extracting potassium under a bias potential from −1.4 to +1.4 V changes the color of the film from transparent to blue (colored state) and blue to transparent (bleached state). The remaining W^{5+} ions reduced to W^{6+} at +1.4 V (bleached state). The positive shift of R-space in the W structure indicates that the average oxidation state of W increased because of an increase in the R-space. The FT provided information on the partial atomic distribution around the W atoms in the WO_3 system. For the ratio of $Ar:O_2$ flow rate of 80:40 (in sccm unit), DC power of 150 W and sample was annealed at 400 °C, the resulting filtered data and wavenumber in a range of 3-10 Å were shown in figure 6.12 (Prins and Koningsberger, 1988). The FT spectra of R space showed that the single scattering contributions from the location of three W−O shells and the next location of W−W shells in tetragonal WO_3 model, two W−O shells and the next location of K−W shells in triclinic $K_2W_2O_5$ and W−O shells, W−K and the next location of W−W shells in cubic KWO_3 model model were determined (Li et al., 1995) in colored state. In the other case, The FT spectra of R space showed that the single scattering contributions from the location of three W−O shells and the next location of W−W shells in tetragonal WO_3 model and three W−O shells and the next location of W−W shells in triclinic WO_3 were determined (Li et al., 1995) in bleached state. The parameters of the EXAFS fitting such as interatomic distances (R), Debye-Waller factors (σ^2), and amplitude reduction

(S_0^2) were shown in table 6.4 (Mansour et al., 2002). These EXAFS results suggest a change in symmetry of the WO_3 thin films structure when the films were exposed to potassium ion (colored state). That means upon potassium exposure, due to potassium ion insertion, the structure varies from strongly distorted symmetry. Further, the ionic charge of W changes from 6+ state to 5+ states for the films in colored states. Additionally, the EXAFS fitting data of the ratio of Ar:O_2 flow rate of 80:40 (in sccm unit), DC power of 100, 150, and 200 W and sample were annealed at 400 $^\circ$C samples implied and supported the XANES results for the K insertion/extraction to the structural environment around W atoms in the WO_3 structure. A local structure was discovered to be affected directly by the K insertion/extraction.
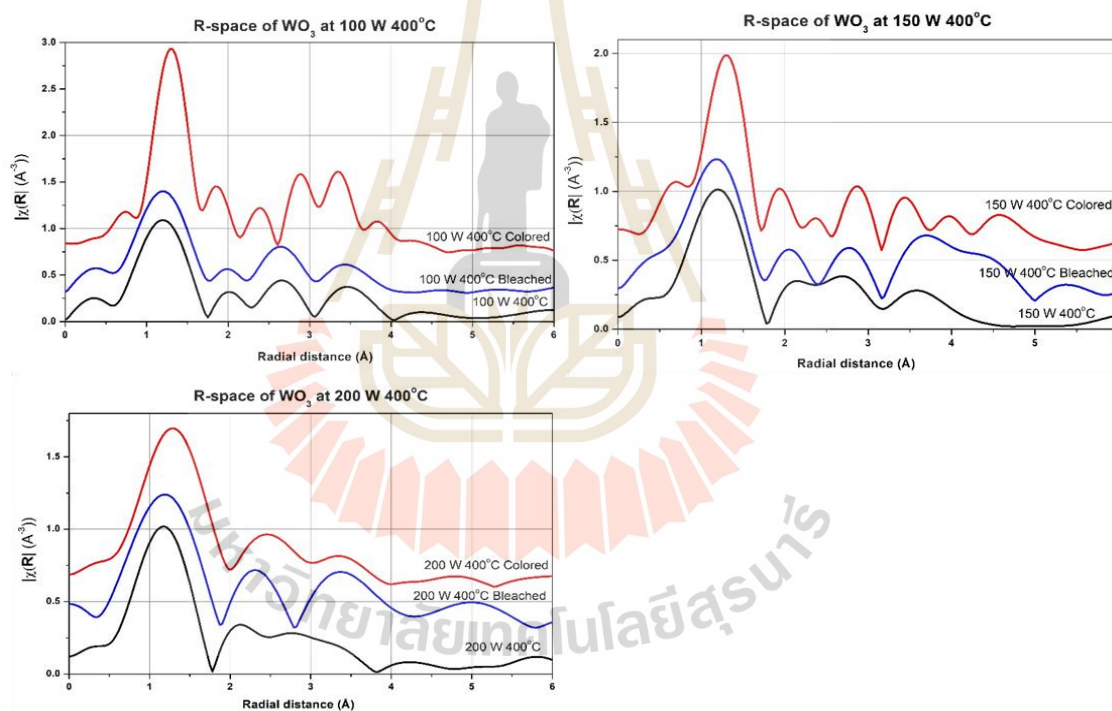
Figure 6.11 The EXAFS (R-space) results from the W L_3-edge of the ratio of Ar:O_2 flow rate of 80:40 (in sccm unit), DC power of 100, 150, and 200 W and sample were annealed at 400 $^\circ$C in as-deposited, bleached and colored state.
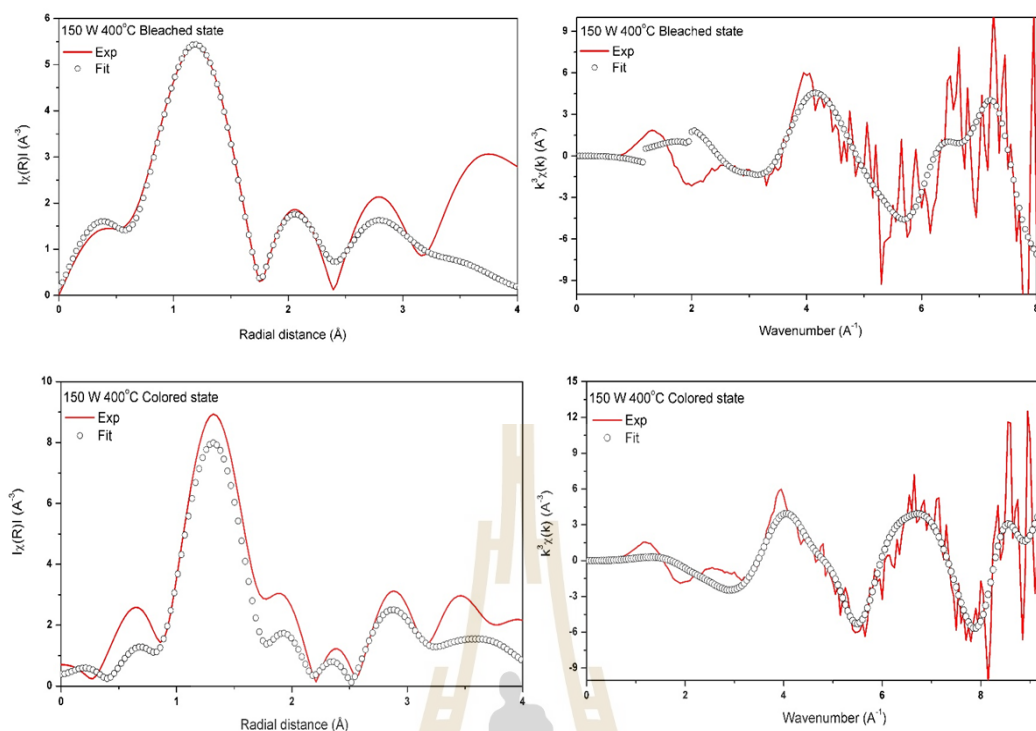
Figure 6.12 Fourier transform of EXAFS spectra at W L_3-edge (left) obtained from the experiment (red line) and fitting (black circle) of tungsten oxide thin films at the ratio of Ar:O_2 flow rate of 80:40 (in sccm unit), DC power of 150 W and sample were annealed at 400 °C in colored and bleached state and k3-weighted EXAFS data (right) of this sample.

Table 6.4 (Continuous) EXAFS fitting parameters of interatomic distance (R), coordination number (N), Debye-Waller factor (σ^2), and amplitude reduction (S_0^2) of the ratio of Ar:O_2 flow rate of 80:40 (in sccm unit), DC power of 150 W and sample were annealed at 400 °C in colored and bleached state.

Sample	Structure	Shell	N	σ^2	R(Å)	S_0^2
150W 400°C colored state	tetragonal WO$_3$	W–O	1	0.00300	1.67	0.558
		W–O	4	0.00316	1.77	0.558
		W–O	1	0.00339	1.92	0.558
		W–W	4	0.00300	3.73	0.558
	triclinic K$_2$W$_2$O$_5$	W–O	2	0.00300	1.74	0.435
		W–O	3	0.00320	2.08	0.435
		W–K	5	0.00300	3.46	0.435

Table 6.4 (Continuous) EXAFS fitting parameters of interatomic distance (R), coordination number (N), Debye-Waller factor (σ^2), and amplitude reduction (S_0^2) of the ratio of Ar:O_2 flow rate of 80:40 (in sccm unit), DC power of 150 W and sample were annealed at 400 °C in colored and bleached state.

Sample	Structure	Shell	N	σ^2	R(Å)	S_0^2
150W 400 °C colored state	cubic KWO$_3$	W–O	6	0.00300	2.01	0.007
		W–K	8	0.00520	3.48	0.007
		W–W	6	0.00600	4.02	0.007
150W 400 °C bleached state	tetragonal WO$_3$	W–O	1	0.00300	1.74	0.617
		W–O	4	0.00600	1.73	0.617
		W–O	1	0.00660	1.85	0.617
		W–W	4	0.00300	3.54	0.617
	triclinic WO$_3$	W–O	1	0.00300	1.93	0.383
		W–O	3	0.00345	2.01	0.383
		W–O	1	0.00360	2.04	0.383
		W–W	2	0.01500	3.55	0.383

6.2.4 Optical contrast

Chananonnawathorn (Chananonnawathorn, 2014) was studied in efficiency of electrochromic device (The transmittance variance) which was generated from delta of %T$_{bleached}$ (percentage of transmittion at bleached state) and %T$_{colored}$ (percentage of transmittion at colored state). The transmittance variance (ΔT) is defined by

$$\Delta\%T = \%T_{bleached} - \%T_{colored} \tag{6.1}$$

$$\%T_{avg} = \frac{\sum_{\lambda_a}^{\lambda_a} T(\lambda)E(\lambda)}{\sum_{\lambda_a}^{\lambda_b} E(\lambda)} \tag{6.2}$$

where T(λ) is percentage of transmittion

E(λ) is relative solar energy (The data of relative solar energy is shown in table 6.5)

So, $\sum_{\lambda_a}^{\lambda_b} E(\lambda) = 100$ because this data was calculated from average visible light and λ_a = 380 nm, λ_b = 780 nm.

In this work, efficiency of electrochromic device of the tungsten oxide thin films at the ratio of Ar:O_2 flow rate of 80:40 (in sccm unit), DC power of 150 W and sample were annealed at 400 $^\circ$C was compared with Δ%T and a high value indicates of Δ%T that the prepared film has good electrochromic properties (Chananonnawathorn, 2014).

Table 6.5 (Continuous) The table of relative solar energy at wavelength of visible light.

Wavelength (nm)	Energy (W/m^2 μm)	Relative Energy
380	513.14	2.06
400	749.95	3.00
420	1003.24	4.02
440	1136.67	4.55
460	1387.34	5.56
480	1456.28	5.83
500	1425.25	5.71
520	1373.08	5.50
540	1362.83	5.46
560	1316.44	5.27
580	1347.84	5.40
600	1324.65	5.30
620	1310.65	5.25
640	1298.73	5.20
660	1278.77	5.12

Table 6.5 (Continuous) The table of relative solar energy at wavelength of visible light.

Wavelength (nm)	Energy(W/m^2 μm)	Relative Energy
680	1249.75	5.00
700	1220.04	4.89
720	1180.45	4.73
740	1140.92	4.57
760	828.63	3.32
780	1065.90	4.27

The electrochromic performance of the of the vanadium oxide thin films at the ratio of Ar:O$_2$ flow rate of 80:40 (in sccm unit), DC power of 150 W and sample were annealed at 400 $^{\circ}$C was characterized by optical contrast (Δ%T) as a function of K$^+$ insertion and extraction in a 0.1 M KOH electrolyte. WO$_3$ thin films were sputtered onto ITO glass. Figure 6.13 showed the transmittance spectra of bleached and colored of WO3 thin films were plotted as a function of wavelength at the ratio of Ar:O$_2$ flow rate of 80:40 (in sccm unit), DC power of 150 W and sample were annealed at 400 $^{\circ}$C. The important efficiency of electrochromic device parameters such as short %T$_{bleached}$ (percentage of transmittion at bleached state) and %T$_{colored}$ (percentage of transmittion at colored state) and optical contrast (Δ%T) which determined from the %T vs wavelength were shown in table 6.6. The optical contrast (Δ%T) of WO$_3$ thin films at the transmittance of bleached and colored of WO$_3$ thin films were 21.14%.
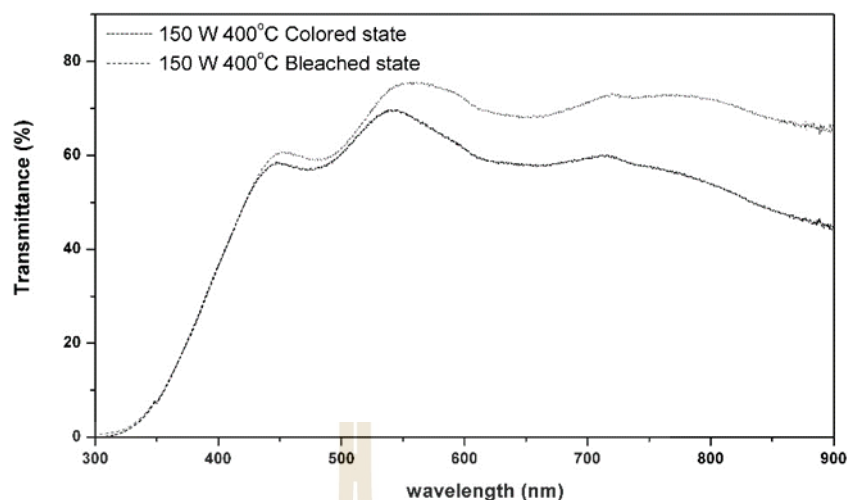
Figure 6.13 The transmittance spectra of bleached and colored of WO_3 thin films were plotted as a function of wavelength at the ratio of Ar:O_2 flow rate of 80:40 (in sccm unit), DC power of 150 W and sample were annealed at 400 °C.

Table 6.6 The table of %$T_{bleached}$ and %$T_{colored}$ of vanadium oxide thin films at different O_2/Ar flow rate.

Sample	%$T_{bleached}$	%$T_{colored}$	Δ%T
150 W 400 °C	79.65	58.51	21.14

      A comparison between the results obtained in this work and other sample is shown in table 6.7. It can be seen that introducing of WO_3 and V_2O_5 in electrochromic device gives a comparing of Δ%T at some O_2/Ar flow rate in V_2O_5 thin films and RF power in WO_3 thin films. From the results were shown V_2O_5 thin films at O_2/Ar = 3/20 (in sccm unit) that has the Δ%T more than WO_3 thin films.

Table 6.7 Comparison of the Δ%T between WO_3 and V_2O_5.

Sample	Δ%T
WO_3 at 150 W 400 °C	21.14
V_2O_5 at O2/Ar = 3/20 (in sccm unit)	22.17

CHAPTER VII

CONCLUSIONS

7.1 V_2O_5 thin films

In this study, vanadium oxide thin films were prepared by RF-magnetron sputtering from the V-metal target. The effect of O_2/Ar ratio on the local structure was investigated in terms of vanadium oxide films by varying an O_2 flow rate at 1-6 sccm and fixing Ar flow rate at 20 sccm, RF power at 200 W and sputtering time at 80 minutes.

7.1.1 Surface and Thickness

The surface roughness of prepared films with O_2/Ar flow rates of 3/20, 4/20, 5/20, and 6/20 (in sccm unit) was higher than that of 1/20 and 2/20 ratio (in sccm unit), and the film with the O_2/Ar flow rate of 3/20 (in sccm unit) had an atomic and weight ratio of 2.29 and 0.72, respectively, which was very close to the O/V atomic and weight ratio of V_2O_5

7.1.2 Phase formation

The XRD patterns could be indexed to V_2O_5. At O_2/Ar flow rate of 3/20 (in sccm unit), the diffraction peak at 20.36° corresponding to the (011) plane of orthorhombic V_2O_5 (space group Pmmn was detected. No other diffraction peak was detected in the other conditions because these samples were an amorphous phase. From XRD results, the V_2O_5 phase was identified. It was further confirmed by the XANES and EXAFS fitting results.

7.1.3 Optical properties

The transmittance spectra and absorption edges of V_2O_5 thin films on glass substrate with different gas flow rate were clearly observed at around 400-600 nm which was corresponded to the energy band gap of V_2O_5 thin films. The value of energy band gap was extracted from transmittance spectra by plotting $(\alpha h v)^2$ vs wavelength and extrapolating the linear portion of the curve to zero. The energy band gap of the V_2O_5 thin films at O_2/Ar flow rate of 1/20, 2/20, 3/20, 4/20, 5/20, and 6/20 (in sccm unit) were estimated to be 2.40, 2.62, 2.74, 2.72, 2.73, and 2.74 eV, respectively.

7.1.4 Local structure

The XANES spectrum at the V K-edge revealed that the produced films included V^{3+}, V^{4+} and V^{5+} in their oxidation states. The strength of the 1s⟶3d transition peak rose when the O_2/Ar ratio was raised. The rise in the intensity of the 1s⟶3d peak is ascribed to the production of V_2O_5 (V^{5+}). Additionally, the EXAFS data suggested and corroborated the XANES findings for the structural environment surrounding the V atoms in the orthorhombic structure of V_2O_5. As a consequence, it was observed that the flow rate of O_2/Ar gas may impact the rate at which RF-sputter systems deposit material on a local structure. It is believed that increasing the O_2/Ar gas flow rate increases the energy flux at the substrate, resulting in a quicker deposition rate. When other restrictions, such as a set sputtering power or working gas pressure, are present, the gas flow rate may be changed to achieve the required V_2O_5 structure. Additionally, the maximum chamber evacuation throughput capabilities must be addressed for the range of working gas flow rate adjustments required to provide a more precise control of sputtering chamber conditions.

7.1.5 Electrochromic properties

The electrochemical of sodium-ion insertion/extraction properties of the V_2O_5 thin films at O_2/Ar of 1/20, 2/20, 3/20, 4/20, 5/20, and 6/20 (in sccm unit) were investigated in 0.154 M NaCl solution and using the two-electrode system, in which Pt plate were used as the counter and reference electrodes. Cyclic voltammetry was performed between −1.8 and +1.8 V (versus Pt) at a scanning rate of 10 mV/s using a potentiostat/galvanostat.

7.1.5.1 Specific capacitance

The specific capacitance of the V_2O_5 thin films was calculated to be 16.1, 11.3, 19.8, 7.6, 14.1, and 10.6 mF for O_2/Ar flow rates of 1/20, 2/20, 3/20, 4/20, 5/20, and 6/20 (in sccm unit), respectively. CV curves with V_2O_5 thin films coated by RF reactive magnetron sputtering at O_2/Ar = 3/20 had the maximum specific capacitance of 19.8 mF, which was greater than other conditions.

The sodium-ion insertion/extraction and optical properties of the V_2O_5 thin films at O_2/Ar of 1/20, 2/20, 3/20, 4/20, 5/20, and 6/20 (in sccm unit) were investigated in 0.154 M NaCl solution and using the two-electrode system, in which Ni foam sheet

and Cu plate were used as the counter. Potential window was performed between −1.8 and +1.8 V for XAS and -0.3 V to +0.3 V for UV-Vis.

7.1.5.2 Oxidation state

The electrodeposition of V_2O_5 at continuous 1.8 V circumstances produced V_2O_5 thin films with varied local electronic structures and a different gas flow rate, according to electrochemical XAS experiments. V_2O_5 thin films' oxidation states range from V^{5+} in a bleached condition to V^{3+} and V^{4+} in a colored state. The effects of Na insertion/extraction on the vanadium oxidation states were investigated using XAS data in this research. The valence shift of the cations causes color switching when sodium is inserted.

7.1.5.3 Optical contrast

The highest optical contrast (Δ%T, good electrochromic properties) is 22.17% was obtained from electrochromic device with V_2O_5 thin film which coat by RF reactive magnetron sputtering at O_2/Ar = 3/20 (in sccm unit) which was higher than the other. So, at O_2/Ar = 3/20 (in sccm unit) has good performance for electrochromic deviece (compaired with other conditions).

7.2 WO$_3$ thin films

The tungsten oxide thin films were prepared by tungsten metal target and Ar: O_2 flow rate of 80:40 (in sccm unit), while the DC power was by 100 W (sputtering time at 12.30 minute), 150 W (sputtering time at 7.13 minute), 200 W (sputtering time at 4.45 minute) and all samples were annealed at 400 °C.

7.2.1 Phase formation

The XRD patterns could be indexed to WO3. At the ratio of Ar:O_2 flow rate of 80:40 (in sccm unit) and DC power of 100, 150 and 200W and all samples were annealed at 400°C. The diffraction peak at 23.194°, 23.69°, 24.4°, 28.98°, and 34.23° corresponding to the (002), (020), (200), (112), and (220) plane of WO$_3$ lattice parameters of a=7.3013Å, b=7.539Å, c=7.6893Å, and β=90.893° was detected.

7.2.2 Optical properties

The value of energy band gap was extracted from transmittance spectra by plotting $(\alpha h\nu)^2$ vs hν and extrapolating the linear portion of the curve to zero. The

energy band gap of tungsten oxide thin films on ITO glass substrate with the ratio of Ar:O_2 flow rate of 80:40 (in sccm unit) and DC power of 100, 150, and 200W and all samples were annealed at 400 $^\circ$C were estimated to be 2.88, 2.90, and 3.00 eV, respectively.

7.2.3 Local structure and electrochromic properties

The electrochemical behavior of the WO_3 material was investigated using the two-electrode system, in which Cu plate were used as the counter electrodes. XAS and UV-vis were adopted to investigate the potassium (K) insertion/extraction behavior in 0.1 M KOH. The WO_3 electrodes at the ratio of Ar:O_2 flow rate of 80:40 (in sccm unit) and DC power of 100, 150, and 200W and all samples were annealed at 400 $^\circ$C in the potential range of −1.4 to 1.4 V.

7.2.3.1 Oxidation state

The electrodeposition of WO_3 at constant 1.4 V circumstances produced WO_3 thin films with variable local electronic structures depending on the conditions, according to electrochemical XAS experiments. The oxidation state of WO_3 thin films ranges from W^{6+} for bleached to W^{5+} for colored. The effects of K insertion/extraction on the tungsten oxidation states were investigated using XAS data in this work. The valence shift of the cations causes color switching when sodium is inserted.

7.2.3.2 Local structure

The structure of WO_3 was altered by K-ion insertion, which caused the shift to more R-space. The R-space obviously increased for bias potentials ranging from 0 to -1.4 V, indicating that with K-ion intercalation, the local structure surrounding the W atom became more symmetrical. Extracting potassium under a bias potential of -1.4 to +1.4 V, on the other hand, changes the color of the film from transparent to blue (colored state) and then back to transparent (bleached state). At +1.4 V, the remaining W^{5+} ions were converted to W^{6+} (bleached state). The positive R-space shift in the W structure implies that the average oxidation state of W rose as the R-space increased.

7.2.3.3 Optical contrast

The optical contrast (Δ%T) of WO_3 thin films at the transmittance of bleached and colored of WO_3 thin films (150 W) were 21.14%.

A comparison between the results obtained in this work (V_2O_5) and other sample (WO_3). It can be seen that introducing of WO_3 and V_2O_5 in electrochromic device gives a comparing of $\Delta\%T$ at some O_2/Ar flow rate in V_2O_5 thin films and RF power in WO_3 thin films. From the results were shown V_2O_5 thin films at $O_2/Ar = 3/20$ (in sccm unit) that has the $\Delta\%T$ more than WO_3 thin films.

This thesis work focused on the development of vacuum sintering techniques and the synthesis of LTP-MnBi magnetic materials as an alternative to producing rare-earth-free permanent magnetic materials. The synthesis methods were studied and optimized with various parameters and conditions, such as the effect of gravity during sintering, particle size, vacuum pressure, Mn grinding time, glycine addition, and hybridization with cobalt. XRD, SEM/EDS, and XPS techniques were used to investigate the phases, microstructure, morphology, and chemical composition. The VSM technique was employed to investigate the magnetic properties.

A simple vacuum sintering system was built and utilized throughout this thesis work. The system provided opportunity to synthesize MnBi magnetic materials sintering without the formation of oxides. The sintered materials are made up of three different materials i.e., LTP-MnBi, Bi and Mn. The MnBi content for short sintering times was still low, resulting in the low energy product which is approximately ten times lower than predicted theoretically. Longer sintering time or using smaller Mn particle size was expected to yield higher MnBi content, and consequently the higher energy product. However, the technique was demonstrated to be a facile technique for synthesizing LTP-MnBi with less energy and time consuming as compared to other techniques.

It was demonstrated that vacuum pressure must be low enough to prevent oxidation. Preparations of MnBi in ultra-high vacuum (10^{-7} mbar), low vacuum (10^{-2} mbar), and under Ar flow were experimented. It was found that vacuum pressure is critical in the formation of MnBi during liquid phase sintering (LPS). The AP-MnBi ingot resulted in the inhomogeneous sintered product after sintering, with separated layers of Bi and MnBi, whereas the UHV-MnBi ingot produced a rather homogeneous material. Oxides were formed in the cases of LV-MnBi and AP-MnBi than in UHV-MnBi.

REFFERENCES

REFERENCES

Abramowitz, M., Davidson, and W. M. (2021). Photomultiplier tubes. *Molecular Expressions. Accessed.*

Acosta, D., Pérez, A., Magaña, C., and Hernández, F. (2016). V_2O_5 thin films deposited by rf magnetron sputtering: the influence of oxygen content in physical properties. *Mater. Sci. Eng A6 (3-4),* 81-87.

Al-Mansoori, M., Al-Shaibani, S., Al-Jaeedi, A., Lee, J., Choi, D., and Hasoon, S. F. (2017). Effects of gas flow rate on the structure and elemental composition of tin oxide thin films deposited by RF sputtering. *AIP Adv 7,* 125105.

Als-Nielsen, J. and McMorrow, D. (2001). Elements of modern x-ray physics. John Wiley and Sons.

Amelio G. (1974). Charge-coupled devices. *Scientific American 230,* 22-31.

Avni, A. A., Pierre-Henri, A., Barry, C. T., Schwendeman, I., Carleton, L. G., Hwang, J., Pinto, J. N., Tanner, B. D., MacDiarmid, G. A., and Reynolds, R. J. (2004). Multicoloured electrochromism in polymers: structures and devices. *Chem Mater 16,* 4401-12.

Bachmann, G. H., Ahmed, R. F., and Barnes, H. W. (1961). The crystal structure of vanadium pentoxide. *Z. Kristallogr. Cryst. Mater, 115,* 110-131.

Balerna, A., Bernieri, E., Burattini, E., Kuzmin, A., Lusis, A., Purans, J., and Cikmach, P. (1991). EXAFS studies of MeO_{3-x} (Me=W, Mo, Re, Ir) crystalline and amorphous oxides. *Nucl. Instrum. Methods. Phys. Res. B, 308,* 234-239.

Bange, K. (1999). Colouration of tungsten oxide films: A model for optically active coatings. *Sol. Energy Mater. Sol. Cells, 58,* 1.

Barreca, D., Armelao, L., Caccavale, F., Noto, D. V., Gregori, A., Rizzi, A. G., and Tondello, E. (2000). Highly oriented V_2O_5 nanocrystalline thin films by plasma-enhanced chemical vapor deposition. *Chem Mater 12,* 98-103.

Barreca, D., Battiston, G. A., Caccavalec, F., Noto, D. V., Gerbasi, R., Gregori, A., Rizzi, A. G., Tiziani, A., and Tondello, E. (1999). A PE-MOCVD route to V_2O_5 nanostructured thin films. *J Phys IV France 9,* 529-536.

Batista, C., Teixeira, V., and Carneiro, J. (2008). Structural and morphological characterization of magnetron sputtered nanocrystalline vanadium oxide films for thermochromic smart surfaces. *J Nano Res, 2,* 21–30.

Bauer, G., Güther, V., Hess, H., Otto, A., Roidl, O., Roller, H., and Sattelberger, S. (2012). Vanadium and vanadium compounds. *Ullmann's encycl. ind. Chem*, *38,* 49-69.

Beke, S. (2011). A review of the growth of V_2O_5 films from 1885 to 2010. *Thin Solid Films*, *519,* 1761-1771.

Benmoussa, M., Ibnouelghazi, E., Bennouna, A., and Ameziane, E.L. (1995). Structural, electrical and optical properties of sputtered vanadium pentoxide thin films. *Thin Solid Films, 265,* 22–28.

Benmoussa, M., Outzourhit, A., Bennouna, A., and Ameziane, E. L. (2002) Electrochromism in sputtered V_2O_5 thin films: structural and optical studies. *Thin Solid Films, 405,* 11–16.

Benmoussa, M., Outzourhit, A., Bennouna, A., and Ihlal, A. (2008). Li^+ ions diffusion into sol-gel V_2O_5 thin films: electrochromic properties. *Eur Phys J Appl Phys, 48,* 10502.

Berton, C. A. M., Avellaneda, O. C., and Bulhões, S. O. L. (2003). Thin film of CeO_2-SiO_2: a new ion storage layer for smart windows. *Sol. Energy Mater. Sol. Cells, 80,* 443-449.

Brandon, D. G. and Kaplan, W. D. (1999). Microstructural characterization of materials. Chichester, Wiley.

Bunker, G. (2010). Introduction to XAFS: A practical Guide to X-ray Absorption Fine Structure Spectroscopy. *Cambridge: Cambridge University press*.

Byker, J. H. (2001). Electrochromics and polymers. *Electrochim. Acta, 46,* 2015-2022.

Cai, G., Cui, M., Kumar, V., Darmawan, P., Wang, J., Wang, X., Eh, S. L. A., Qian, and K., Lee, S. P. (2016). Ultra-large optical modulation of electrochromic porous WO_3 film and the local monitoring of redox activity. *Chem. Sci, 7,* 1373-1382.

Cai, G., Wang, J., and Lee, S. P. (2016). Next-Generation Multifunctional Electrochromic Devices. *Acc. Chem. Res, 49,* 1469-1476.

Camurlu, P. (2014). Polypyrrole derivatives for electrochromic applications. *RSC Adv, 4,* 55832-55845.

Cao, K., Shen, E. D., Österholm, M. A., Kerszulis, A. J., and Reynolds, R. J. (2016). Tuning Color, Contrast, and Redox Stability in High Gap Cathodically Coloring Electrochromic Polymers. *Macromolecules, 49*, 8498-8507.

Cazzanelli, E., Mariotto, G., Passerini, S., and Smyrl, W. H. (1996). Raman spectroscopic investigations of Liintercalated V_2O_5 xerogel. *J Non-Cryst Solids, 208,* 89– 98.

Chakraborty, S., Sakata, H., Yokoyama, E., Wakaki, M., and Chakravorty, D. (2007). Laser induced forward transfer technique for maskless patterning of amorphous V_2O_5 thin films. *Appl Surf Sci, 254,* 638–643.

Chan, L. Y., Pung, Y. S., and Sreekantan, S. (2014). Synthesis of V_2O_5 nanoflakes on PET fiber as visible-light-driven photocatalysts for degradation of RhB Dye. *J. Catal,* 370696.

Chananonnawathorn, C. (2014). Investigation of Electrochromic Property Based on WO_3 Films for Smart Window Application. Thammasat university.

Chang, F. I., Gilbert, L. B., and Sun, I. T. (1975). Electrochemichromic systems for display applications. *J. Electrochem. Soc, 122,* 955-962.

Chang, F. I., Kmetz R. A., and Willisen, K. F. (1976). Nonemissive Electrooptic Displays. *Springer US, Boston, MA,* 155–196.

Chang, W. C., Chung, H. C., and Liou, S. G. (2008). Novel anodic polyelectrochromic aromatic polyamides containing pendent dimethyltriphenylamine moieties. *Macromolecules, 41,* 8441-8451.

Chen, L. C. and Ho, K. C. (2001). Design equations for complementary electrochromic devices: application to the tungsten oxide–Prussian blue system. *Electrochim Acta, 46,* 2151–2158.

Chen, Y., Xie, K., and Liu, Z. (1998). XPS studies of V_2O_5 thin film at different temperatures and oxygen partial pressures. *Appl Surf Sci, 126,* 347–351.

Chen, Z., Augustyn, V., Wen, J., Zhang, Y., Shen, M., Dunn, and B. Lu, Y. (2011). Highperformance supercapacitors based on intertwined CNT/V_2O_5 nanowire nanocomposites. *Adv Mater, 23,* 791.

Chernova, A. N., Roppolo, M., Dillon, C. A., Whittingham, S., and Layered, M. (2009). vanadium and molybdenum oxides: batteries and electrochromics. *J. Mater. Chem, 19,* 2526–2552.

Cong, S., Geng, F., and Zhao, Z. (2016). Tungsten oxide materials for optoelectronic applications. Adv. Mater 28: 10518.

Crandall, S. R., and Faughnan, W. B. (1976). Dynamics of coloration of amorphous electrochromic films of WO_3 at low voltages. *Appl. Phys. Lett, 28,* 95-97.

Cremonesi, A., Bersani, D., Lottici, P. P., Djaoued, Y., and Brüning, R. (2006). Synthesis and structural characterization of mesoporous V_2O_5 thin films for electrochromic applications. *Thin Solid Films, 515,* 1500–1505.

Crociani, L., Carta, G., Natali, M., Rigato, V., and Rossetto, G. (2011). MOCVD of vanadium oxide films with a novel vanadium (III) precursor. *Chem Vapor Depos, 17,* 6–8.

De Castro, M. S. B., Ferreira, C. L., and de Avillez, R. R. (2013). Vanadium oxide thin films produced by magnetron sputtering from a V_2O_5 target at room temperature. *Infrared Phys, Techn 60,* 103–107.

Deb, S. K. (1968). Physical properties of a transition metal oxide: optical and photoelectric properties of single crystal and thin film molybdenum trioxide. *Proceedings of Royal Society A, 304*, 211.

Deb, S. K. (1969). A Novel Electrophotographic System. *Appl. Opt, 8,* 192-195.

Deb, S. K. (1973). Optical and photoelectric properties and colour centres in thin films of tungsten oxide. *J. Theor. Appl. Phys, 27,* 801-822.

Deb, S. K. (2008). Opportunities and challenges in science and technology of WO_3 for electrochromic and related applications. *Sol. Energy Mater. Sol. Cells, 92,* 245-258.

Deb, S. K. and Chopoorian, J. A. (1966). Optical Properties and Color-Center Formation in Thin Films of Molybdenum Trioxide. *Int. J. Appl. Phys, 37,* 4818.

DeVries, J. M., Trimble, C. Tiwald, E. T., Thompson, W. D., and Woollam, A. J. (1999). Optical constants of crystalline WO_3 deposited by magnetron sputtering. *J. Vac. Sci. Technol, 17,* 2906-2910.

Dhananjaya, M., Prakash, N. G., Sandhya G. L., Lakshmi, N. A., and Hussain, O. M. (2017). Microstructure and supercapacitor properties of V_2O_5 thin film prepared by thermal evaporation method. *Mech Mater Sci Eng,* 2412-5954.

Diffey, L. B. (2002). Sources and measurement of ultraviolet radiation. *Methods, 28,* 4-13.

Dyer, A. L., Thompson, E. J., and Reynolds, J. R. (2011). Completing the colour palette with spray-processable polymer electrochromics. *ACS Appl Mater Interfaces, 3,* 1787-1795.

Eh, S. L. A., Tan, M. W. A., Cheng, X., Magdassi, S., and Lee, S. P. (2017). Recent advances in flexible electrochromic devices: prerequisites, challenges, and prospects. *Energy Technol, 6,* 33-45.

Ekwongsa, C., Rujirawat, S., Butnoi, P., Vittayakorn, N., Suttapun, M., Yimnirun, R., and Kidkhunthod, P. (2020). Temperature dependent local structure of $LiCoO_2$ determined by in-situ Co K-edge X-ray absorption fine structure (EXAFS). *Radiat. Phys, Chem 175,* 108545.

Etacheri, V., Marom, R., Elazari, R., Salitra G., and Aurach, D. (2011). Challenges in the development of advanced li-ion batteries. *A Review. Energy Environ.Sci, 11,* 3242-3262.

Fateh, N., Fontalvo, G. A., Cha, L., Klünsner, T., Hlawacek, G., Teichert, C., and Mitterer, C. (2008). Synthesis-structure relations for reactive magnetron sputtered V_2O_5 films. *Surf Coat Tech, 202,* 1551–1555.

Fateh, N., Fontalvo, G. A., and Mitterer, C. (2007). Structural and mechanical properties of dc and pulsed dc reactive magnetron sputtered V_2O_5 films. *J Phys D Appl Phys, 40,* 7716–7719.

Faughnan, B. W., Crandall, R. S., and Hyman, P. M. (1975). Optical Properties of Materials *RCA Rev, 36,* 177.

Faughnan, W. B., Crandall, S. R., and Lampert, A. M. (1975). Model for the bleaching of WO_3 electrochromic films by an electric field. *Appl. Phys. Lett, 27,* 275-277.

Faughnan, W. B., Crandlal, S. R., and Heyman, M. P. (1975). Electrochromism in WO_3 amorphous films. *RCA Rev, 36,* 177-179.

Fultz, B., and Howe, M. J. (2008). Transmission electron microscopy and diffractometry of materials. *Springer Link.*

Gallasch, T., Stockhoff, T., Baither, D., and Schmitz, G. (2011). Ion beam sputter deposition of V_2O_5 thin films. *J Power Sources, 196,* 428–435.

Garcia-Lobato, A. M., Martinez, I. A., Perry, L. D., Castro-Roman, M., Zarate, A. R., and Escobar Alarcon, L. (2011). Elucidation of the electrochromic mechanism of nanostructured iron oxides films. *Sol. Energy Mater. Sol. Cells, 95,* 751-758.

Giannetta, H. M. R., Calaza, C., Lamas, D. G., Fonseca, L., and Fraigi, L. (2015). Electrical transport properties of V_2O_5 thin films obtained by thermal annealing of layers grown by RF magnetron sputtering at room temperature. *Thin Solid Films, 589,* 730–734.

Gokdemir, F. P., Ozdemir, O., and Kutlu, K. (2014). Comparison of structural and electrochemical properties of V_2O_5 thin films prepared by organic/inorganic precursors. *Electrochim Acta, 121,* 240–244.

Goodenough, J.B. (1971). Metallic oxides. *Prog. in Solid State Chem, 5,* 145-399.

Granqvist C. G. (1995). Handbook of Inorganic Electrochromic Materials, *Elsevier*, Amsterdam.

Granqvist C. G. (2000). Electrochromic tungsten oxide films: Review of progress 1993–1998. *Sol. Energy Mater. Sol. Cells, 60,* 201-262.

Granqvist, G. C. (2008). Oxide electrochromics: why, how, and whither. *Sol Energy Mater Sol Cells, 92,* 203-208.

Granqvist, G. C. (2014). Electrochromics for smart windows: Oxide-based thin films and devices. *Thin solid films, 564,* 1-38.

Granqvist, G. C., Lansåker, C. P., Mlyuka, R. N., Niklasson, A. G., and Avendaño, E. (2009). Progress in chromogenics: new results for electrochromic and thermochromic materials and devices. Sol. Energy Mater. *Sol. Cells, 93,* 2032-2039.

Groot, D., F., F. M., Hu, Z. W., Lopez, M. F., Kaindl, G., Guillot, F. and Tronc, M. (1994). Differences between L_3 and L_2 x-ray absorption spectra of transition metal compounds. *J. Chem. Phys, 101,* 6570.

Groult, H., Le, Van. K., Mantoux, A., Perrigaud, L., and Doppelt, P. (2007). Study of the Li+ insertion into V_2O_5 films deposited by CVD onto various substrates. *J Power Sources, 174,* 312-320.

Guan, Z. S., Yao, J. N., Yang, Y. A., and Loo, B. H. (1998). Electrochromism of annealed vacuum evaporated V_2O_5 films. *J Electroanal Chem, 443,* 175–179.

Haijin, S., Yuna, K., Bhuvana, T., Jiyea, L., Xu, Y., Cheolmin, P., and Eunkyoung, K. (2012). Colour combination of conductive polymers for black electrochromism. *ACS Appl Mater Interfaces, 4,* 185-191.

Hajimoto, Y., and Hara, T. (1976). Coloration in a WO_3 film. *Appl. Phys. Lett, 28,* 228-229.

Hench, L. L. and West, J. K. (1990). Principles of electronic ceramics. Wiley.

Hippert, F., Geissler, E., Hodeau, J. L., Leliévre-Berna, E. and Regnard, J. R. (2006). Neutron and X-ray Spectroscopy. *Netherlands: Springer.*

Ho, C. K., Greenberg, B. C. (1994). Tungsten oxide-prussian blue electrochromic system based on a proton-conducting polymer electrolyte. *J. Electrochem. Soc, 141,* 2061-2067.

Ho, K. Y., Chang., C. C., Wei., H. D., Dong., L. C., Chen., L. C., Chen., L. J., Jang., L. W., Hsu., C. C., Chan, S. T., Kumar, K., Chang, L. C., and Wu, K. M. (2013). Characterization of gasochromic vanadium oxides films by X-ray absorption spectroscopy. *Thin Solid Films, 544,* 461-465.

Hong, S. F., Hwang, S. C., and Chen, L. C. (2008). Deposition-order-dependent polyelectrochromic and redox behaviors of the polyanilineeprussian blue bilayer. *Electrochim Acta, 53,* 6215-27.

Hughes, M. (2016). What is sputtering? Retrieved, *http://www.semicore.com/news/92-what-is-rf-sputtering.*

Hüppauff, M., and Lengeler, B. (1993). Valency and Structure of Iridium in Anodic Iridium Oxide Films. *J. Electrochem. Soc, 140,* 598-602.

Iida, Y., Kaneko, Y., Kanno, and Y. (2008). Fabrication of pulsed-laser deposited V_2O_5 thin films for electrochromic devices. *J Mater Process Tech, 197,* 261–267.

Inaba, K. Kobayashi, S. Uehara, K. Okada, Reddy, A. S. and Endo, T. (2013). High resolution X-ray diffraction analyses of (La,Sr)MnO$_3$/ZnO/Sapphire(0001) double heteroepitaxial films. *Advances in Materials Physics and Chemistry, 3,* 72-89.

Invernale, A. M., Seshadri, V., Mamangun, D. M. D., Ding, Y., Filloramo, J., and Sotzing, A. G. (2009). Polythieno thiophene as an optically transparent Ion-storage layer. *Chem. Mater, 21,* 3332-3336.

Irie, M., Fukaminato, T., Matsuda, K., Kobatake, S., (2014). Photochromism of diarylethene molecules and crystals: memories, switches, and actuators. *Chem. Rev, 114,* 12174-12277.

Julien, C., Guesdon, J. P., Gorenstein, A., Khelfa, A., and Ivanov, I. (1995). The growth of V$_2$O$_5$ flash-evaporated films. *J Mater Sci Lett, 14,* 934-936.

Julien, C., Guesdon, J. P., Gorenstein, A., Khelfa, A., Ivanov, I. (1995). The influence of the substrate material on the growth of V$_2$O$_5$ flash-evaporated films. *Appl Surf Sci, 90,* 389-391.

Julien, C., Khelfa, A., Benramdane, N., Guesdon, J. P., Dzwonkowski, P., Samaras, I., and Balkanski, M. (1994). Lithium insertion in indium selenide films: application to microbatteries. *Mater Sci Eng B-Adv, 23,* 105-115.

Justin, T. (2021). UV-Vis Spectroscopy: Principle, Strengths and Limitations and Applications Retrieved, *https://www.technologynetworks.com.*

Jutimoosik, J. (2010). Local structure of magnesium zinc oxide nanocrystals. M.S. thesis, Suranaree University of Technology, Nakorn Ratchasima.

Kaid, M. A. (2006). Characterization of electrochromic vanadium pentoxide thin films prepared by spray pyrolysis. *Egypt J Solids, 29,* 273–291.

Kamper, A., Hahndorf, I., and Baerns, M. (2000). A molecular mechanics study of the adsorption of ethane and propane on V$_2$O$_5$(001) surfaces with oxygen vacancies. *Top. Catal, 11,* 77-84.

Kang, M., Chu, M., Kim, S. W., and Wook, R. J. (2013) Optical and electrical properties of V2O5 nanorod films grown using an electron beam. *Thin Solid Films, 547,* 198–201.

Kawai, J. (2000). Absorption techniques in x-ray spectrometry, Encyclopedia of analytical chemistry. *New York, Wiley.*

Kidkhunthod, P., Nilmoung, S., Mahakot, S., Rodporn, S., Phumying, S., and Maensiri, S. (2016). A structural study and magnetic properties of electrospun carbon/manganese ferrite (C/MnFe$_2$O$_4$) composite nanofibers. *J. Magn. Magn. Mater, 401,* 436-442.

Klysubun, W. (2006). X-ray Absorption Spectroscopy Technique. Nakhon Ratchasima Synchrotron Light Research Institute.

Kodre, A. (2002). XANES spectroscopy (online). http:*www.ung.si/arcon/xas/xanes/xanes-theory.pdf.*

Koike, S., Fujieda, T., Sakai, T., and Higuchi, S. (1999). Characterization of sputtered vanadium oxide films for lithium batteries. *J Power Sources, 81–82,* 581–584.

Koningsberger, D.C. and Prins, R. (1988). X-ray Absorption: Principles, Applications of EXAFS, SEXAFS, and XANES. John Wiley & Sons Inc.

Kovendhan, M., Joseph, D. P., Manimuthu, P., Sendilkumar, A., Karthick, S. N., Sambasivam, S., Vijayarangamuthu, K., Hee, J. K., Byung, C. C., Asokan, K., Venkateswaran, C., and Mohan, R. (2015). Prototype electrochromic device and dye sensitized solar cell using spray deposited undoped and 'Li' doped V$_2$O$_5$ thin film electrodes. *Curr Appl Phys, 215,* 622–631.

Kumagai, N., Kitamoto, H., Baba, M., Durand-Vidal, S., Devilliers, and D., Groult, H. (1998). Intercalation of lithium in r.f.-sputtered vanadium oxide film as an electrode material for lithium-ion batteries. *J. Appl. Electrochem, 28,* 41-48.

Kumar, RTR., Karunagaran, B., Venkatachalam, S., Mangalaraj, D., Narayandass, Sa. K., and Kesavamoorthy, R. (2003). Influence of deposition temperature on the growth of vacuum evaporated V$_2$O$_5$ thin films. *Mater Lett, 57,* 3820-3825.

Kuzmin, A., Purans, J. (1993). X-ray absorption spectroscopy study of local structural changes in a-WO$_3$ under colouration. *J. Phys.: Condens. Matter, 5,* 2333-2340.

Larsen, D. (2014). XANES: Application. *http://chemwiki.ucdavis.edu.htm.*

Lee, H. S., Deshpande, R., Parilla, A. P., Jones, M. K., To, B., Mahan, H. A., and Dillon, C. A. (2006). Crystalline WO$_3$ nanoparticles for highly improved electrochromic applications. *J. Adv. Mater, 18,* 763-766.

Lee, K., Abe, Y., Kawamura, M., and Kim, H. K. (2012). Effects of substrate temperature on electrochromic properties of cobalt oxide and oxyhydroxide thin films prepared by reactive sputtering using O_2 and H_2O gases. *J. Appl. Phys, 51,* 045501.

Li, G. G., Bridges, F., and Booth, H. C. (1995). X-ray-absorption fine-structure standards: A comparison of experiment and theory. *Phys. Rev. B Condens. Matter, 52,* 6332-6348.

Liberatore, M., Decker, F., Vuk, A. S., Orel, B., and Dražič, G. (2006). Effect of the organic–inorganic template ICSPPG on sol-gel deposited V_2O_5 electrochromic thin film. *Sol Energ Mat Sol C, 90,* 434–443.

Lin, Y. S., Tsai, C. W., and Chen, P. W. (2008). Electrochromic properties of V_2O_{5-z} thin films sputtered onto flexible PE/ITO substrates. *Solid State Ionics, 179,* 290–297.

Lin, Y. S. and Tsai C. W. (2008). Reactive sputtering deposition of V_2O_{5-z} on flexible PET/ITO substrates for electrochromic devices. *Surf Coat Tech, 202,* 5641–5645.

Lourenço, A., Gorenstein, A., Passerini, S., Smyrl, W. H., Fantini, M. C. A., and Tabacniks, M. H. (1998). Radiofrequency reactively sputtered VO_x thin films deposited at different oxygen flows. *J Electrochem Soc, 145,* 706–711.

Lu, Y. R., Wu, Z. T., Chen, L. C., Wei, H. D., Chen, L. J., Chou, C. W., and Dong, L. C. (2015). Mechanism of electrochemical deposition and coloration of electrochromic V_2O_5 nano thin films: an In situ X-ray spectroscopy study. *Nanoscale Res. Lett, 10,* 387- 393.

Lu, Y., Liu, L., Mandler, D., and Pooi, S. L. (2013). High switching speed and coloration efficiency of titanium-doped vanadium oxide thin film electrochromic devices. *J Mater Chem C, 1,* 7380–7386.

Ma, D. and Wang, J. (2016). Inorganic electrochromic materials based on tungsten oxide and nickel oxide nanostructures. *Sci. China. Chem, 60,* 54–62.

Ma, X., Lu, S., Wan, F., Fangchao, W., Mingyao, H., Quanwei, W., Quanyao, Z., and Galina, S. Z. (2016). Synthesis and electrochromic characterization of graphene /V_2O_5/MoO_3 nanocomposite films. *ECS J Solid State Sc, 5,* P572–P577.

Mansour, N. A., Smith, H. P., Baker, M. W., Balasubramanian, M., and McBreen, J., (2002). In situ XAS investigation of the oxidation state and local structure of vanadium in discharged and charged V_2O_5 aerogel cathodes. *Electrochim. Acta, 47,* 3151-3161.

Mantoux, A., Groult, H., Balnois, E., Doppelt, P., and Gueroudji L. (2004). Vanadium oxide films synthesized by CVD and used as positive electrodes in secondary lithium batteries. *J Electrochem Soc, 151,* A368-A373.

Mastragostino, M., Arbizzani, C., Ferloni, P., and Marinangeli, A. (1992). Polymer-based electrochromic devices. *Solid State Ionics, 56,* 471-478

Meacham, P. A., Wijayantha, U. G. K., Peter, M. L., and Ward, D. M. (2004). Polyelectrochromic behaviour in the visible and near-infrared region of a window based on a dinuclear ruthenium–dioxolene complex adsorbed onto a nanocrystalline SnO_2 electrode. *Inorg. Chem. Commun, 7,* 65-68.

Meyer, B. (1992). Applying 'design by contract'. *IEEE, 25,* 40-51.

Mjejri, I., Manceriu, LM., Gaudon, M., Rougier, A., and Sediri, F. (2016). Nano-vanadium pentoxide films for electrochromic displays. *Solid State Ionics, 292,* 8–14.

Mo, Y., Antonio, M. R., and Scherson, D. A. (2000). In situ Ru k-edge x-ray absorption fine structure studies of electroprecipitated ruthenium dioxide films with relevance to supercapacitor applications. *J. Phys. Chem. B, 104,* 9777–9779.

Monk, P. M. S., Mortimer, R. J., and Rosseinsky, D. R. (1995). Electrochromism: fundamentals and applications. *VCH Edition,* 243.

Monk, P. M. S., Mortimer, R. J., and Rosseinsky, D. R. (2007). Electrochromism and electrochromic devices. *Cambridge Edition,* 1-512.

Mortimer, J. R. (1997). Electrochromic materials. Chem. *Soc. Rev, 26,* 147-156.

Mortimer, J. R. (1999). Organic electrochromic materials. *Electrochim. Acta, 44,* 2971-2981.

Mortimer, J. R., Rosseinsky, R. D., and Monk, S. M. P. (2015). Electrochromic materials and devices. *WILEY-VCH.*

Murawski, L., Gledel, C., Sanchez, C., Livage, J., and Audières, J. P. (1987). Electrical conductivity of V_2O_5 and $Li_xV_2O_5$ amorphous thin films. *J Non-Cryst Solids, 89,* 98-106.

Nabavi,M., Sanchez, C., and Livage, J. (1991). Structure and properties of amorphous V_2O_5. Philos. *Mag. Lett, 63,* 941-953.

Najdoski, M., Koleva, V., and Samet, A. (2014). Effect of deposition conditions on the electrochromic properties of nanostructured thin films of ammonium intercalated vanadium pentoxide xerogel. *J Phys Chem C, 118,* 9636–9646.

Najdoski, M., Koleva, V., and Samet, A. (2014). Effect of deposition conditions on the electrochromic properties of nanostructured thin films of ammonium intercalated vanadium pentoxide xerogel. *J Phys Chem C, 118,* 9636–9646.

Namioka, T. (2000). 17 - Diffraction gratings. *Vacuum Ultraviolet Spectroscopy, 1,* 347-377.

Nandakumar, N. K. and Seebauer, E. G. (2011). Low temperature chemical vapor deposition of nanocrystalline V_2O_5 thin films. *Thin Solid Films, 519,* 3663–3668.

Newville, M. (2004). Consortium for Advanced Radiation Sources. Chicago.

Oßigwald, S., Breimaier, S., Linseis, M., and Winter, F. R. (1993). Polyelectrochromic vinyl ruthenium-modified tritylium dyes. *Organometallics, 36,* 1993-2003.

Ottaviano, L., Pennisi, A., Simone, F., and Salvi, A. M. (2004). RF sputtered electrochromic V_2O_5 films. *Opt Mater, 27,* 307–313.

Patel, J. K., Bhatt, G. G., Ray, R. J., Suryavanshi, P., and Panchal, J. C., (2017). All-inorganic solid-state electrochromic devices: a review. *J. Solid State Electrochem, 21,* 337-347.

Patridge, J. C., Love, T. C., Swider-Lyons, E. K., Twigg, E. M., and Ramaker, E. D. (2013). In-situ X-ray absorption spectroscopy analysis of capacity fade in nanoscale-$LiCoO_2$. *J. Solid State Chem, 203,* 134–144.

Pauporté, T., Aberdam, D., Hazemann, J. L., Faure, R., and Durand, R. (1999). X-ray absorption in relation to valency of iridium in sputtered iridium oxide films. *J. Electroanal. Chem, 465,* 88-95.

Pauporté, T., Soldo-Olivier, Y., and Faure, R. (2003). XAS Study of Amorphous WO_3 formation from a peroxo-tungstate solution. *J. Phys. Chem. B, 107,* 8861-8867.

Pauporté, T., Soldo-Olivier, Y., and Faure, R. (2004). In situ X-ray absorption spectroscopy study of lithium insertion into sputtered WO_3 thin films. *J. Electroanal. Chem, 562,* 111-116.

Picollo, M., Aceto, M., and Vitorino, T. (2018). UV-Vis spectroscopy. *Phys. Sci. Rev, 4,* 1-14.

Platt, R. J. (1961). Electrochromism, a possible change of colour producible in dyes by an electric field. *J Chem Phys, 34,* 862.

Poelman, H., Tomaszewski, H., Poelman, D., Fiermans, L., Gryse, D. R., Reyniers, M. F., and Marin, B. G. (2002). V_2O_5 thin films deposited by means of dc magnetron sputtering from ceramic V_2O_3 targets. *Surf Interface Anal, 34,* 724–727.

Poumellec, B., Kraizman, V., Aifa, Y., Cortès, R., Novakovich, A., and Vedrinskii, R. (1998). Experimental and theoretical studies of dipole and quadrupole contributions to the vanadium K-edge XANES for $VOPO_4$ $_2H_2O$ xerogel. *Phys. Rev. B Condens. Matter, 58,* 6133-6146.

Prins, R. and Koningsberger, C. D. (1988). X-ray Absorption: principles, applications, techniques of EXAFS, SEXAFS, XANES, *https://www.osti.gov/biblio/5927479.*

Qu, Y. H., Primetzhofer, D., Arvizu, A. M., Qiu, Z., Cindemir, U., Granqvist G. C., and Niklasson, A. G. (2017). Electrochemical rejuvenation of anodically coloring electrochromic nickel oxide thin films. *ACS Appl. Mater. Interfaces, 9,* 42420-42424.

Quinzeni, I., Ferrari, S., Quartarone, E., and Mustarelli, P. (2011). Structural, morphological and electrochemical properties of nanocrystalline V_2O_5 thin films deposited by means of radiofrequency magnetron sputtering. *J Power Sources, 196,* 10228–10233.

Raj, D. V., Ponpandian, N., Mangalaraj, M., and Viswanathan, C. (2013). Effect of annealing and electrochemical properties of sol-gel dip coated nanocrystalline V_2O_5 thin films. *Mat Sci Semicon Proc, 16,* 256–262.

Raj, P. D., Gupta, S., and Sridharan, M. (2015). Nanostructured V_2O_5 thin films deposited at low sputtering power. *Mat Sci Semicon Proc, 39,* 426–432.

Ramana, C. V., Hussain, O. M., Naidu, B. S., Julien, C., and Balkanski, M. (1998). Physical investigations on electron-beam evaporated vanadium pentoxide films. *Mater Sci Eng B-Adv, 52,* 32-39.

Rao, MC. and Rao, RK. (2014). Thermal evaporated V_2O_5 thin films: thermodynamic properties. *Int J Chem Tech Res, 6,* 3931–3934.

Rauh, D. R. (1999). Electrochromic windows: an overview. *Electrochim. Acta, 44,* 3165-3176.

Ravel B. and Newville, M. Athena, Artemis, Hephaestus: data analysis for Xray absorption spectroscopy using IFEFFIT. *J. Synchrotron Radiat, 12,* 537–541.

Ravel, B. D. (1997). Ferroelectric phase transition in oxide perovskites studied by XAFS. Ph.D. Dissertation, University of Washington, Washington.

Rehr, J. J. and Albers, R. C. (2000). Theoretical approaches to x-ray absorption fine structure. *Rev. Mod. Phys, 72,* 621.

Robbins, J. and Seman, M. (2005). Electrochromic devices deposited on low-temperature plastics by plasma-enhanced chemical vapor deposition. United States, *USDOE Office of Energy Efficiency and Renewable Energy (EERE)*, FG36-04GO14328.

Rodella, B. C. and Mastelaro, R. V. (2003). Structural characterization of the V_2O5/TiO_2 system obtained by the sol–gel method. *J Phys Chem Solids, 64,* 833-839.

Rosaiah, P. and Hussain, O. M. (2013). Electron beam evaporated nano crystalline V_2O_5 thin films for electrochromic and electrochemical applications, In: Giri P, Goswami D, Perumal A, Advanced Nanomaterials and Nanotechnology. Springer Proceedings in Physics, Berlin, Heidelberg, *Springer, 143,* 485–496.

Rosseinsky, R. D. and Mortimer, J. R. (2001). Electrochromic systems and the prospects for devices. *Adv. Mater, 13,* 783-793.

Rowley, M. N. and Mortimer, J. R. (2002). New electrochromic materials. *Sci. Prog, 85,* 243-262.

Sahana, M. B. and Shivashankar, S.A. (2004). Metalorganic chemical vapor deposition of highly oriented thin film composites of V_2O_5 and V_6O_{13}: suppression of the metal-semiconductor transition in V_6O_{13}. *J Mater Res, 19,* 2859–2870.

Santos, R., Loureiro, J., Nogueira, A., Elangovan, E., Pinto, J. V., Veiga, J. P., Busani, T., Fortunato, E., Martins, R., and Ferreira, I. (2013). Thermoelectric properties of V_2O_5 thin films deposited by thermal evaporation. *Appl Surf Sci, 282,* 590-594.

Sarminio, J., Talledd, A., Andersson, A. A., Passerini, S., and Decker, F. (1993). Stress and electrochromism induced by Li insertion in crystalline and amorphous V_2O_5 thin film electrodes. *Electrochim Acta, 12,* 1637– 1642.

Seeboth, A., Lötzsch, D., Ruhmann, R., and Muehling, O., (2014). Thermochromic Polymers—Function by Design. *Chem. Rev, 114,* 3037-3068.

Shanthakumar, P. (2008). X-ray study of two complex oxides, each having octahedral oxygen co-ordination of transition metals. Ph.D. Dissertation, University of Connecticut, Connecticut.

Shimizu, Y., Nagase, K., Miura, N., and Yamazoe, N. (1990). New preparation process of V_2O_5 thin film based on spin-coating from organic vanadium solution. *Jpn J Appl Phys, 29,* L1708–L1711.

Silversmit, G., Poelman, H., and DeGryse, R. (2004). Influence of magnetron deposition parameters on the stoichiometry of sputtered V_2O_5 films. *Surf Interface Anal, 36,* 1163–1166.

Šipr, O., Šimnek, A., Bocharov, S., Kirchner, Th., and Dräger, G. (1999). Geometric and electronic structure effects in polarized V K-edge absorption near-edge structure spectra of V_2O_5. Phys. *Rev. B Condens. Matter, 60,* 115-127.

Stern, E. A., Heald, S. M., and Koch, E. E. (1983). Synchrotron Radiation. North-Holland.

Stizza, S., Mancini, G., Benfatto, M., Natoli, R. C., Garcia, J., Bianconi, A. (1989) Structure of oriented V_2O_5 gel studied by polarized x-ray-absorption spectroscopy at the vanadium K edge. *Phys. Rev. B Condens. Matter, 40,* 229-236.

Su, Q., Lan, W., Wang, Y. Y., and Liu, X. Q. (2009). Structural characterization of **β**-V_2O_5 films prepared by dc reactive magnetron sputtering. *Appl Surf Sci, 255,* 4177–4179.

Suli, A., Torok, M.I., and Hevesi, I. (1986). On the capacitance of n-V_2O_5/p-Si heterojunctions. *Thin Solid Films, 139,* 233-246.

Surnev, S., Ramsey, M. G., and Netzer, F. P. (2003). Vanadium oxide surface studies. *Surf. Sci, 73,* 117-165.

Talledo, A., Andersson, A. M., and Granqvist, C. G. (1990). Electrochemically lithiated V_2O_5 films: An optically passive ion storage for transparent electrochromic devices. *J Mater Res, 5,* 1253–1256.

Thakur, K. V., Ding, G., Ma, J., Lee, S. P., and Lu, X. (2012). Hybrid materials and polymer electrolytes for electrochromic device applications. *Adv. Mater, 24,* 4071-4096.

Thompson, A. C., Attwood, D. T., Gullikson, E. M., Howells, M. R., Jeffrey B. Kortright, Robinson, A. L., Underwood, J. H., Kim, K.-J., Kirz, J., Lindau, I., Pianetta, P., Winick, H., Williams, G. P., and Scofield, J. H. (2001). X-ray data booklet. Berkeley: Lawrence Berkeley Laboratory.

Vernardou, D. (2017). Using an atmospheric pressure chemical vapor deposition process for the development of V_2O_5 as an electrochromic material. *Coatings, 7,* 24.

Vernardou, D., Loudoudakis, D., Spanakis, E., Katsarakis, N., and Koudoumas, E. (2014). Electrochemical properties of vanadium oxide coatings grown by hydrothermal synthesis on FTO substrates. *New J Chem, 38,* 1959–1964.

Vernardou, D., Sapountzis, A., Spanakis, E., Kenanakis, G., Koudoumas, E., and Katsarakis, N. (2013). Electrochemical activity of electrodeposited V_2O_5 coatings. *J Electrochem Soc, 160,* D6–D9.

Wang, J., Curtis, C. J., Schulz, D. L., and Zhang, G. J. (2004). Influences of treatment temperature and water content on capacity and rechargeability of V_2O_5 xerogel films. *J Electrochem Soc, 151,* A1–A7.

Wang, Q., Huang, J., Zhou, J., Liu, Z., Geng, Y., Liang, Z., Du, Y., and Tian., X. (2018). Different nanostructured tungsten oxides synthesized by facile solvothermal route for chlorine gas sensing. Sens. *Actuators B Chem, 275,* 306-311.

Wang, X. G., Jiang, Y. S., Yang, N. H., Yuan, L., and Pang, S. J. (1999). Crystallinity and morphology changes of a-WO_3 films. *Appl. Surf. Sci, 143,* 135-141.

Wang, Y., Shang, H., Chou, T., and Guozhong, C. (2005). Effects of thermal annealing on the Li+ intercalation properties of $V_2O_5 \cdot nH_2O$ xerogel films. *J Phys Chem B, 109,* 11361–11366.

Watanabe, H., Itoh, K., and Matsumoto, O. (2001). Properties of V_2O_5 thin films deposited by means of plasma MOCVD. *Thin Solid Films, 386,* 281-285.

Weckhuysen, M. B., Jehng, M. J., and Wachs, E. I. (2000). In situ raman spectroscopy of supported transition metal oxide catalysts: $18o_2–16o_2$ isotopic labeling studies. *J. Phys. Chem. B, 104,* 7382–7387.

Weckhuysen, M. and Keller, D. E. (2003). Chemistry, spectroscopy and the role of supported vanadium oxides in heterogeneous catalysis. *Catal. Today, 78,* 25-46.

Wei, D., Scherer, M. R., Bower, C., Andrew, P., Ryhänen, T., and Steiner, U. (2012). A nanostructured electrochromic supercapacitor. *Nano Lett, 12,* 1857.

Wong, J., Lytle, W. F., Messmer, P. R., and Maylotte, H. D. (1984). K-edge absorption spectra of selected vanadium compounds. *Phys. Rev. B Condens. Matter, 30,* 5596-5610.

Wruck, D., Ramamurthi, S., and Rubin, M. (1989). Sputtered electrochromic V_2O_5 films. *Thin Solid Films, 182,* 79–85.

Wu, Y. Z., Xian, C. D., Hu, D. T., Xie, N. Y., Tao, Y., Natoli, R. C., Paris, E., and Marcelli, A. (2004). Quadrupolar transitions and medium-range-order effects in metal K-edge x-ray absorption spectra of 3d transition-metal compounds. *Phys. Rev. B Condens. Matter, 70,* 033104, 1-4.

Xia, H. X., Tu, P. J., Zhang, J., Xiang, Y. J., Wang, L. X., and Zhao, B. X. (2010). Fast electrochromic properties of self-supported Co_3O_4 nanowire array film. *Sol. Energy Mater. Sol. Cells, 94,* 386-389.

Xia, H. X., Tu, P. J., Zhang, J., Xiang, Y. J., Wang, L. X., and Zhao, B. X. (2010). Cobalt oxide ordered bowl-like array films prepared by electrodeposition through monolayer polystyrene sphere template and electrochromic properties. *ACS Appl. Mater. Interfaces, 2,* 186–192.

Xiong, S., Yin, S., Wang, Y., Kong, Z., Lan, J., Zhang, R., Gong, M., Wu, B., Chu, J., and Wang, X. (2017). Organic/inorganic electrochromic nanocomposites with various interfacial interactions: A review. *Mater. Sci. Eng, 221,* 41-53.

Yang, P., Sun, P., and Mai, W. (2016). Electrochromic energy storage devices. Mater. *Today, 19,* 394-402.

Yang, Y. A. and Yao, J. N. (2000). Microstructural properties of an electrochromic WO_3 thin film. *J Phys Chem Solids, 61,* 647-650.

Yi, C., Yi-Jie, T., Hai-Feng, C., and Zhao-Yang, Z. (2013). Tricolour electrochromism of PEDOT film electrodeposited in mixed solution of boron trifluoride diethyl etherate and tetrahydrofuran: hypsochromic effect. *J Appl Polym Sci, 129,* 3764-71.

Yoon, Y. S., Kim, J.S., and Choi, S. H. (2004). Structural and electrochemical properties of vanadium oxide thin films grown by d.c. and r.f. reactive sputtering at room temperature. *Thin Solid Films, 460,* 41–47.

Yoshino, T., Baba, N., and Kouda, Y. (1987). Electrochromic properties of V_2O_5 thin films colloidchemically deposited onto ITO glasses. *Jpn J Appl Phys, 26,* 782–783.

Yoshino, T., Kobayashi, K., Araki, S., Nakamura, K., and Kobayashi, N. (2012). Electrochromic properties of electrochemically fabricated nanostructure nickel oxide and manganese oxide films. *Sol. Energy Mater. Sol. Cells, 99,* 43-49.

Zahid, A., Afzal, N., and Rafique, M. (2019). Effect of Ar: O_2 ratio on reactively magnetron sputtered ZnO film's properties. *Mater. Res. Express, 6,* 116419.

Zeller, R. H., Kmetz, R. A., and von Willisen, K. F. (1976). Nonemissive Electrooptic Displays. *Springer US, Boston,* 149-154.

Zhou, D., Xie, D., Xia, X., Wang, X., Gu, C., and Tu, J. (2016). All-solid-state electrochromic devices based on WO_3NiO films: material developments and future applications. *Sci. China. Chem, 60,* 3–12.

นันทนัส วัฒนสุภิญโญ. (2553). สมบัติทางกายภาพของฟิล์มบางซิงค์ออกไซด์เจือด้วยอลูมิเนียมและอินเดียมเตรียมโดย เทคนิค ดีซี แมกนี ตรอนสปัตเตอริง. สืบค้นจาก *http://thesis.swu.ac.th/swuthesis/Phy(M.S.)/Nuntanut_W.pdf.*

APPENDIX

APPENDIX

Taylor & Francis
Taylor & Francis Group

Check for updates
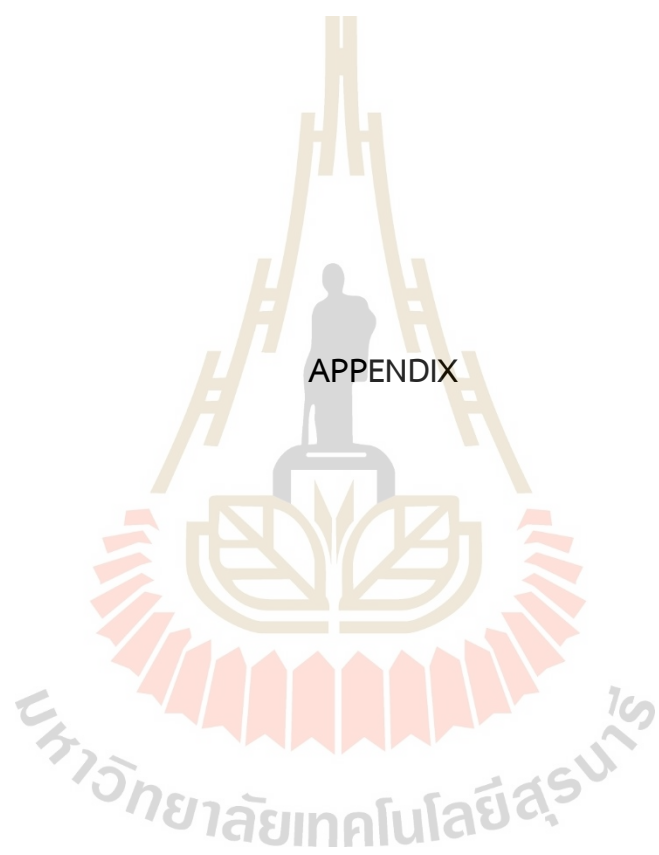
Local structure and structural properties of vanadium oxide thin films prepared by radio-frequency reactive magnetron sputtering at various oxygen flow rate

Piyaporn Thangdee[a], Ekachai Chongsereecharoen[b], Thanun Chunjaemsri[a], Chinawat Ekwongsa[a], Pinit Kidkhunthod[c], Narong Chanlek[c], Natthapong Wongdamnern[d], Prapan Manyum[e], Saroj Rujirawat[c], and Rattikorn Yimnirun[f,g]

[a]Reaserch Network NANOTEC-SUT on Advanced Nanomaterials and Characterization, School of Physics, Institute of Science, Suranaree University of Technology, Nakhon Ratchasama, Thailand; [b]Faculty of Science and Technology, Valaya Alongkorn Rajabhat University, Klong Luang, Pathumthani, Thailand; [c]Synchrotron Light Research Institute (Public Organization), Nakhon Ratchasama, Thailand; [d]Faculty of Science and Technology, Rajamangala University of Technology Suvarnabhumi, Nonthaburi, Thailand; [e]School of Physics and Center of Excellence in High Energy Physics and Astrophysics, Suranaree University of Technology, Nakhon Ratchasama, Thailand; [f]School of Energy Science and Engineering, Vidyasirimedhi Institute of Science and Technology (VISTEC), Wangchan, Rayong, Thailand; [g]Research Network of NANOTEC-VISTEC on Nanotechnology for Energy, Vidyasirimedhi Institute of Science and Technology (VISTEC), Wangchan, Rayong, Thailand

ABSTRACT

In this work, vanadium oxide thin films were prepared by using radio frequency reactive magnetron sputtering with vanadium metal target. The effect of O_2 flow rate was investigated in terms of vanadium oxide thin films by varying O_2/Ar flow rate at 1/20, 2/20, 3/20, 4/20, 5/20, 6/20 (in sccm unit) with fixed RF power at 200 W and sputtering time at 80 minutes. The surface morphology and crystal structure of V_2O_5 thin films were investigated by scanning electron microscope (SEM), atomic force microscope (AFM), and X-Ray Diffractometer (XRD) respectively. The influence of the O_2/Ar ratio on a local structure of vanadium oxide thin films was studied by the Synchrotron x-ray absorption spectroscopy (XAS) technique. The oxidation states of vanadium oxide thin films were measured at V K-edge by the x-ray absorption near-edge structure (XANES). The results of XANES spectra at the V K-edge showed that the prepared films under the O_2/Ar flow rate at 1/20 sccm contained the vanadium with the oxidation states of V^{3+} and V^{5+} while the others contained only V^{5+}. This is because the higher O_2/Ar flow rate possibly causes an increase in energy flux at the substrate and the 1s→3d transition peak's intensity, which could lead to a higher deposition rate. To achieve the desired V_2O_5 structure, the gas flow rate could be adjusted properly. The evolution of the local structure around V atoms was studied using the extended x-ray absorption fine structure (EXAFS) which supported the XANES results indicating that the structural environment around V atoms is in good agreement with the V_2O_5 orthorhombic structure. Finally, XANES and EXAFS fitting results confirmed that the O_2 flow rate affected the local structure of vanadium oxide thin films.

CURRICULUM VITAE

Name: Mr. Piyaporn Thangdee

Education Background:

2009-2012   B.Sc. (Physics) Khon Kean University, Khon Kean, Thailand

2013-2016   M.Sc. (Applied Physics) Chiang Mai University, Chiang Mai Thailand

2016-2022   Ph.D. (Physics) Suranaree University of Technology, Nakorn Ratchasima, Thailand.

Academic Experience:

- Research Assistant at Synchrotron Light Research Institute (Public Organization), Thailand.

- Teaching Assistant at Laboratory, School of Physics, Suranaree University of Technology, Thailand.